High-Quality InP on GaAs

by

Nathaniel Joseph Quitoriano

B.S. with Honors in Materials Science and Mineral Engineering
University of California, Berkeley, 2000

B.S. with Honors in Materials Electrical Engineering and Computer Science
University of California, Berkeley, 2000

Submitted to the Department of Materials Science and Engineering
in Partial Fulfillment of the Requirements for the Degree of

Doctor of Philosophy in Electronic Materials

at the
Massachusetts Institute of Technology

September 2006

Signature of Author: ______________________________
Department of Materials Science and Engineering
June 21, 2004

Certified by: ______________________________
Eugene A. Fitzgerald
Merton C. Flemings-SMA Professor of Materials Science and Engineering
Thesis Supervisor

Accepted by: ______________________________
Samuel M. Allen
POSCO Professor of Physical Metallurgy
Chair, Departmental Committee on Graduate Students

High-Quality InP on GaAs

by

Nathaniel Joseph Quitoriano

Submitted to the Department of Materials Science and Engineering
on May 25, 2006 in Partial Fulfillment of the Requirements for the
Degree of Doctor of Philosophy in Electronic Materials

ABSTRACT

In addition to traditional telecommunication applications, devices based on InP have received increased attention for high-performance electronics. InP growth on GaAs is motivated by the fact that InP wafers are smaller, more expensive, and utilize older fabrication equipment than GaAs. High-quality InP on GaAs may also serve as a step towards bringing high-quality InP onto the Si platform. Integrating high-quality InP onto bulk GaAs has proven to be challenging, however. While a number of commercial Molecular Beam Epitaxy (MBE) growth foundries offer InP on GaAs for M-HEMT (Metamorphic High-Electron-Mobility Transistor) applications, the successful demonstration of InP-based, minority-carrier devices on bulk GaAs remains elusive.

In this work InP on GaAs suitable for minority carrier devices is demonstrated exhibiting a threading dislocation density of $1.2\times10^6/\text{cm}^2$ determined by plan-view transmission electron microscopy. To further quantify the quality of this InP on GaAs, a photoluminescence (PL) structure was grown to compare the quality to bulk InP. Comparable room and low (20K) temperature PL was attained. (The intensity from the PL structure grown on the InP on GaAs was ~70% of that on bulk InP at both temperatures.) To achieve this, graded buffers in the InGaAs, InGaP, InAlAs and InGaAlAs materials systems were explored. In each of these systems, under certain growth conditions, microscopic compositional inhomogeneities along the growth direction blocked dislocations leading to dislocation densities sometimes $> 10^9/\text{cm}^2$. Using scanning-transmission electron microscopy, composition variations were observed. These composition variations are caused by surface-driven phase separation leading to Ga-rich regions.

As the phase separation blocked dislocation glide and led to high threading dislocation densities, conditions for avoiding phase separation were explored and identified. Composition variations could be prevented in $\text{In}_x\text{Ga}_{1-x}\text{As}$ graded buffers grown at 725 °C to yield low dislocation densities of $9\times10^5/\text{cm}^2$ for $x < 0.34$, accommodating ~70% of the lattice mismatch between GaAs and InP. However, further grading to 53% In is required to attain the lattice constant of InP. Compositional grading in the $\text{In}_y\text{Ga}_{1-y}\text{P}$ ($0.8 < y < 1.0$) materials system was found to accommodate the remaining lattice mismatch with no rise in threading dislocation density by avoiding phase separation. Consequently, to achieve high-quality InP on GaAs a graded buffer in the InGaAs material system was followed by a graded buffer in the InGaP materials system to reach InP.

The research to achieve high-quality InP on GaAs diverged into two paths. The first successful path, using graded buffers in different materials systems, was discussed

above. The second path involved the deposition of InP at various temperatures on the high-quality $In_{0.34}Ga_{0.66}As$ platform that was developed to determine if InP deposited on the InGaAs platform with 1.2% misfit relaxed controllably without much dislocation nucleation. To the contrary, rampant dislocation nucleation occurred in this highly-strained InP at all temperatures studied. Interestingly, however, the InP was observed to relax via a secondary-slip system, a/2<110>{110}.

This secondary-slip system has a Burgers vector typical in semiconductors of a/2<110>. Unlike the primary-slip system, where dislocations glide on {111}-type planes, the secondary-slip system dislocations glide on {110}-type planes. Relaxation via the secondary-slip system was found to be a function of stress and temperature. A critical stress, e_c, appears to be required for dislocations to glide via the secondary-slip system otherwise all relaxation occurs by the primary-slip system. For $e > e_c$ and at all temperatures studied, both the primary- and secondary-slip systems are active with apparent cross-slip from one system to the other. At low temperatures, nearly all of the relaxation was accomplished through the secondary-slip system, however. The amount of relaxation via the primary- and secondary-slip systems at three different temperatures was quantified; the resulting Arrhenius plot suggests a difference in the activation energy for glide between the two systems is 1.5 eV.

TABLE OF CONTENTS

LIST OF FIGURES

Figure 6.12.

InGaP graded buffer grown at 600 °C on an InGaAs virtual substrate. Figures (a)-(e) are cross section micrographs of the same region. Micrographs (a)-(d) are STEM results including a Ga element map (a), an In element map (b), a P element map (c) and an ADF image taken of the region under the diffraction condition in which the maps were taken. Micrograph (e) is a

Chapter 1. Motivation

1.1. Motivation for InP on GaAs

The properties of InP and other materials with similar lattice constants enable state-of-the-art electronic and optical devices. Near lattice matched InGaAs on InP has very high electron mobilities and band alignments that have enabled record transistor speeds (604 GHz with electron mobilities, $\mu_e > 10^4$ cm^2/Vs[1]). The traditional use of InP materials, however, is in the telecommunications industry where lattice matched $In_{0.58}Ga_{0.42}As_{0.9}P_{0.1}$ emits 1.55 μm light which corresponds to the low absorption wavelength in SiO_2 fiber optic cables (see Figure 1.1). InP is a small, expensive, and fragile semiconductor, however limiting its use to niche markets. Bringing the InP lattice constant onto GaAs and perhaps eventually onto Si will allow for greater economies of scale and possibly opening new markets. An additional problem for InP and other related materials lies in the fact that InP devices are fabricated on wafers with small diameters.

To understand why the small size of InP wafers is a problem, one must understand the implications on the InP industry from the Si industry driving the integrated circuit technology for over 40 years. Over the years the Si wafers were produced with larger diameters to take advantage of economies of scale. (Many costs associated in fabricating microelectronics are largely insensitive to size of the wafer. As a result the larger wafer one can use implies a lower cost per chip.) As Si wafer sizes increased, old Si fabrication facilities that produced chips on smaller wafers were sold to the GaAs industry as GaAs wafer sizes also increased. Thus the GaAs industry used old Si industry tools; one step further from state-of-the-art, the InP industry purchased old GaAs fabrication facilities. Since the minimum feature size has reduced in the Si industry as the wafer size has increased, older InP fabrication equipment can typically render only large feature sizes. This has not been too problematic because the InP industry has used epitaxially defined layers to fabricate key dimensions. Thus bringing InP to GaAs (and eventually to Si) offers a two fold benefit, greater economies of scale and use of more state-of-the-art equipment.

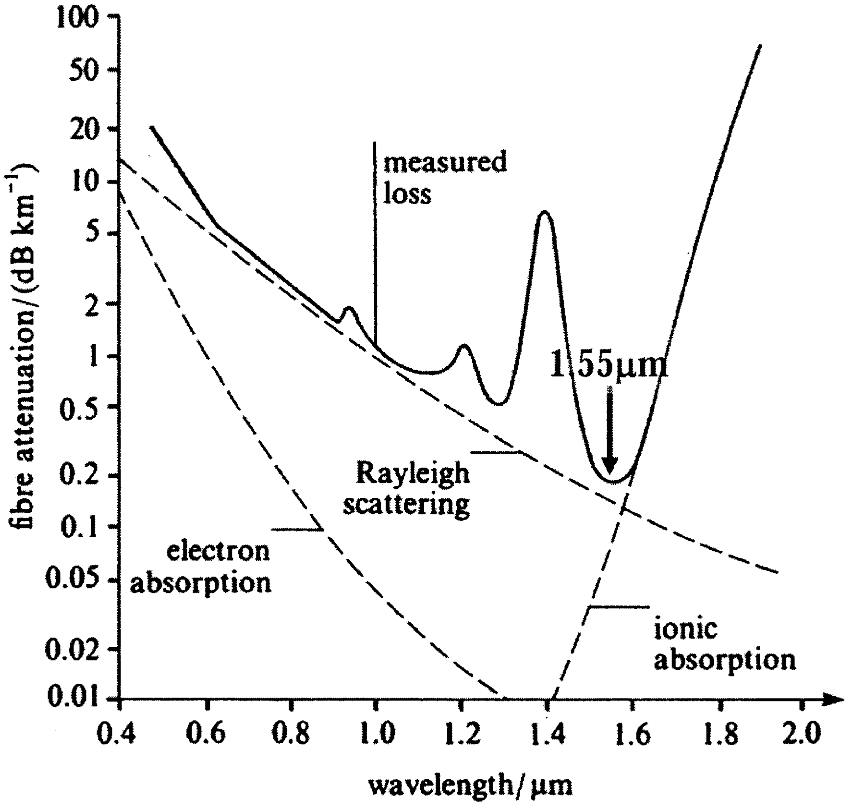

Figure 1.1: Attenuation coefficient, α, vs. wavelength of light in SiO_2 fiber optic cables. The minimum absorption occurs at 1.55 μm which corresponds to the bandgap of $In_{0.58}Ga_{0.42}As_{0.9}P_{0.1}$. The peaks in the attenuation above the Rayleigh scattering around 1.2 and 1.4 μm are due to absorption by OH impurities. (The figure was reproduced from Gorham *et al.*[2])

Typically devices are designed such that the epitaxial semiconductors used in the devices are lattice matched to the substrate. For this reason, group IV semiconductors are not usually associated with heterojunctions because no group IV semiconductors are lattice matched to them. In III-V semiconductors, however, lattice matched materials are available making them very flexible and useful. Lattice-matched semiconductors are available for compound semiconductors because of the extra degree of freedom brought about through the use of two atoms which allows a number of ternary and quaternary materials systems available for a given lattice constant. For example, InP has a lattice constant of 5.868 Å and, as a result the ternary and quaternary III-V semiconductor systems include InGaAsP, InAlGaAs, InGaAs, InAlAs, and AlAsSb are lattice matched to it (at particular compositions). These materials systems on InP allow for a bandgap range from about 0.7-1.95 eV as seen in Figure 1.2.

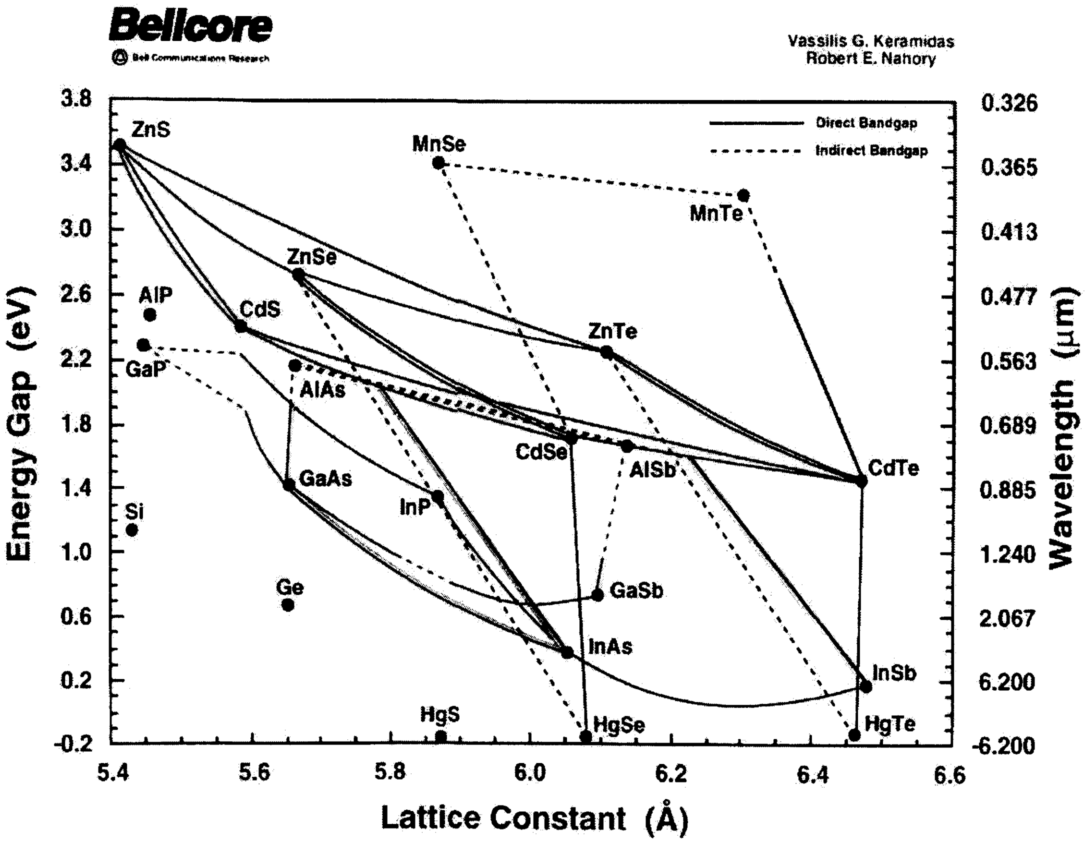

Figure 1.2 Energy gap vs. lattice constant diagram for many group IV, III-V and II-VI semiconductors. (Figure reproduced from poster by V.G. Keramidas and R.E. Nahory.)

1.2. Motivation for Dislocation Control

Designers tend to grow lattice matched materials on commercially available substrates to avoid dislocations because dislocations reduce minority carrier lifetimes and decrease free carrier mobility. There has been some work in lattice-mismatched semiconductors (especially for quantum wells in III-V materials where the layer can be grown thin enough to avoid dislocations). However, because of the lack of understanding of lattice-mismatched semiconductors and dislocations, lattice-mismatched semiconductors are generally avoided.

Figure 1.3 shows the effect of the density of dislocations in devices on the minority carrier lifetime in that device. In Figure 1.3 the minority carrier lifetime is constant for low dislocation densities and then reduces roughly proportionally to the dislocation density. This plateau for low dislocation densities is because for low dislocation densities, most electrons will not encounter a dislocation and recombine there. However, once the spacing between dislocations is on the order of the mean diffusion distance of a minority carrier the minority carrier lifetime will decrease. As dislocations are detrimental to device performance, they must be minimized.

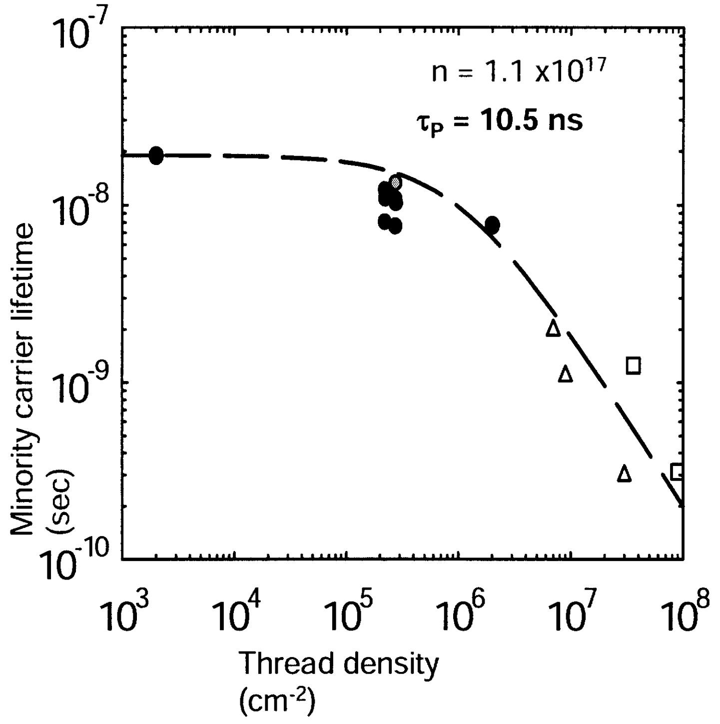

Figure 1.3: Minority carrier lifetime vs. threading dislocation density in GaAs. The data comes from Groenert[3] and Carlin[4] and compiled by Groenert[3].

1.3. Thesis format

The next chapter discusses why dislocations are thermodynamically favored for some lattice-mismatched films and the conditions for which this occurs. As three different types of dislocations were observed in this work, Chapter 2 also discusses the difference between these dislocations including the glide plane and Burgers vectors.

Chapter 3 discusses methodologies by which high-quality materials can be integrated together including bonding, small area growth techniques and compositional grading. Graded buffers are discussed in some detail because most samples discussed in this work have some compositional grading.

Composition variations due to phase separation were observed in some of the semiconductor alloys explored in this work. Consequently, chapter 4 discusses phase separation in semiconductors. Since phase separation is not fully understood for growth conditions, phase separation in general is discussed as well.

Chapter 5 briefly discusses the methodologies used in this work with emphasis on transmission electron microscopy as well as x-ray diffraction since these were the two characterization methods used most.

Most of the results from this work are in chapters 6 and 7. Chapter 6 discusses how high-quality InP on GaAs was achieved using InGaAs and InGaP compositionally graded buffers. This result was obtained by understanding and avoiding phase separation in the InGaAs and InGaP materials systems.

Chapter 7 discusses the relaxation of InP depositied on a lattice constant between GaAs and InP. This InP was found to relax via a secondary slip system where dislocations glide on {110}-type planes instead of {111}-type planes. The relaxation via the secondary slip system was studied as a function of temperature and lattice-mismatch.

Finally, chapter 8 summarizes the key results from this work and indicates some paths for future work for these and other materials.

Chapter 2. Introduction to Lattice-mismatch

Heteroepitaxy, epitaxial growth of a different material on another, allows for the ability to engineer band gaps, band offsets, lattice constants, and mobility enhancements. Without heteroepitaxy, quantum well lasers, HBTs (Heterojunction Bipolar Transistor), or modern CMOS devices would not be possible[5]. Heteroepitaxy can be divided into two types, heteroepitaxy with materials having the same lattice constant or lattice-mismatched heteroepitaxy. Often, engineers restrict device designs to those that have lattice constants close to commercially available substrates. The criterion to limit the choice of materials to those close to the lattice constant of the substrate is the result of the desire to avoid nucleating dislocations which deteriorate device performance. Dislocations reduce the minority carrier lifetime as well as reduce the electron and hole free carrier mobilities, μ_e and $\mu_{h,}$ in devices. The reduction in minority carrier lifetimes results from the fact that dislocations are recombination centers for electrons and holes. Figure 1.3 plots the minority carrier lifetime versus threading dislocation density in GaAs. The minority carrier lifetime in phosphide-based materials is expected to be less affected by the threading dislocation density. Dislocations reduce μ_e and μ_h because dislocations are scattering centers for free carriers since they are deviations from a perfect crystal having both broken and bent bonds.

2.1. Background in lattice-mismatched semiconductors

At times a desired performance metric cannot be achieved at small misfits from the substrate lattice constant where the misfit, f, is defined by

$$f = \frac{a_s - a_f}{a_f} = \varepsilon + \delta$$ **Equation 1**

where a_s and a_f are the lattice constants for the substrate and film, respectively and ε and δ are the elastic and plastic strains, respectively. When the desired metric requires dislocations to be nucleated, dislocation morphology must be understood and controlled to ensure the device is not deleteriously affected.

Equation 1 suggests there are two mechanisms by which a lattice-mismatch can be accommodated, elastic and plastic strains. Elastic strain accommodates the lattice-mismatch through the distortion of atomic bonds away from the equilibrium atomic position, r_o. This deviation from r_o increases the energy of the system as seen in the Leonard-Jones potential, Figure 2.1. Plastic strain, on the other hand, accommodates the lattice-mismatch through the formation of dislocations. Dislocations can be extra half planes of atoms that reduce the elastic distortion of lattice-mismatched films. The formation of a dislocation requires energy, E_d. E_d is usually larger then small deviations from the equilibrium atomic position. Consequently, a lattice-mismatched material will initially deform elastically because a small deviation from equilibrium increases the energy of the system roughly continuously while nucleation of a dislocation requires a finite increase.

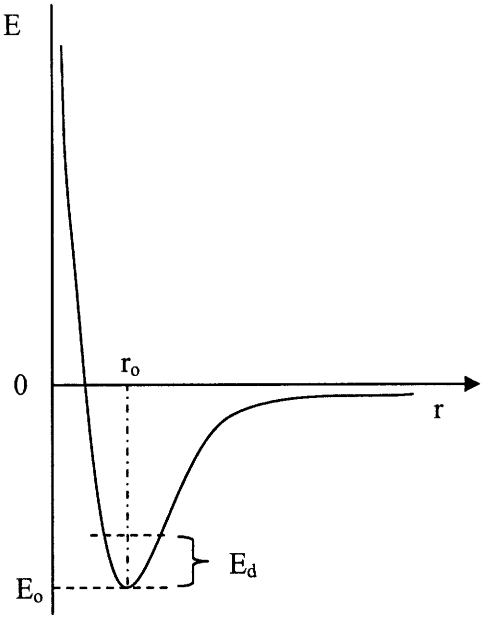

Figure 2.1: Schematic of the Leonard-Jones Potential which illustrates the energy of a system of two atoms separated by distance, r. The energy at infinity is defined as zero while the minimum energy at r_0 is E_0. The Leonard-Jones potential can be used to schematically illustrate the effects of changing the interatomic distance in a solid away from the equilibrium spacing, r_0. Small deviations from r_0 increase the energy of the system roughly continuously. The energy to form a dislocation, E_d, is a finite energy above E_0. As a result, atom bonds in a solid will initially distort and, after the distortion is large enough, form dislocations.

As is suggested from the Leonard-Jones potential, initially a reasonable lattice-mismatched film will grow psuedomorphically on the substrate. That is to say the film will adopt the in-plane lattice parameter of the substrate, thereby deviating from r_o, and no dislocations will be nucleated. As a result, all of the misfit stress will be taken up in elastic distortion of the crystal lattice. Expressed in terms of Equation 1 the lattice-mismatch is equal to the elastic strain, $f = \varepsilon$. A film initially takes all of the mismatch stress by deforming the lattice because distortions of the lattice are roughly continuous while dislocations add a finite energy to a system due to the broken bonds and strain fields associated with them.

If the substrate were thin it too would deform, however, since the substrate is usually much thicker than the film and elastic energy is proportional to thickness, for small thicknesses it is a good approximation to assume that the substrate maintains its equilibrium lattice constant while the film distorts to match the substrate's in plane lattice constant. The case for a film whose equilibrium lattice constant is larger than the substrate's is depicted in Figure 2.2; because $a_f > a_s$, the film is in a state of biaxial compression. (All lattice-mismatched films in this work have lattice constant larger than the substrate.)

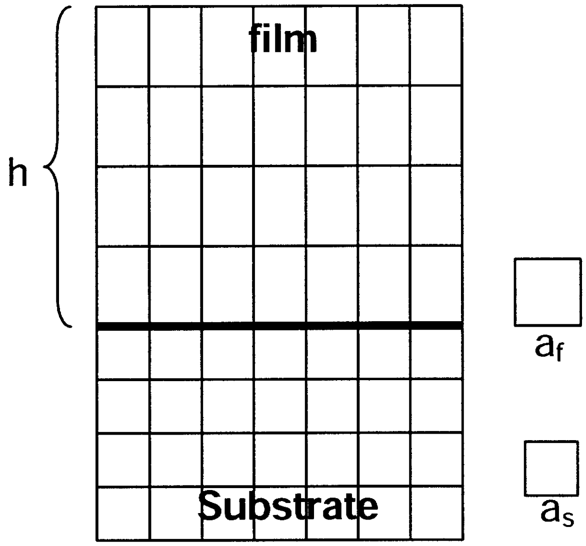

Figure 2.2: A pseudomorphically grown film, with thickness h, and an equilibrium lattice constant a_f on a substrate with equilibrium lattice constant a_s. Pseudomorphic material implies that there are no dislocations and all of the misfit strain is taken up elastically by lattice distortions.

2.2. Critical Thickness

As the thickness, h, of the film in Figure 2.2 is increased, there will be a critical thickness, h_c, at which dislocation formation will be energetically favored. This occurs because the elastic strain energy is proportional to thickness and eventually the energy to distort the lattice will be greater then the energy to form a dislocation. The case where there is elastic strain and dislocations present, the misfit strain will be divided between the elastic and plastic components, $f = \varepsilon + \delta$. A film with both elastic and plastic deformation is schematically illustrated in Figure 2.3.

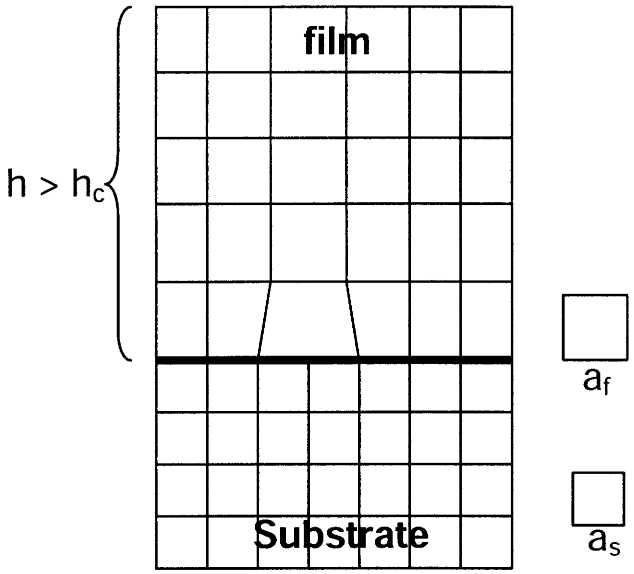

Figure 2.3: Lattice-mismatched film of thickness, $h > h_c$ (the critical thickness). The fact that $h > h_c$ is evident by the presence of a misfit dislocation at the substrate film interface. The misfit dislocation partially relaxes the misfit strain f. Consequently, the misfit strain, f, is divided into elastic, ε, and plastic, δ, components whose sum is f (See Equation 1).

The value for the critical thickness, h_c at which dislocations become energetically favored, can be calculated equating energies or forces. Matthews *et al.* have derived h_c in both ways yielding similar expressions[6]. A short derivation of the critical thickness, h_c, using the energetic considerations is presented here following the work of Fitzgerald[7]. As mentioned earlier, the elastic strain energy per unit area, E_ε, of a distorted film is proportional to the thickness, h, and the stiffness of the material given by the Young's Modulus, Y, following the expression below.

$$E_\varepsilon = \varepsilon^2 Yh \qquad \textbf{Equation 2}$$

where Young's modulus for the (001) surface is given by

$$Y = C_{11} + C_{12} - 2\frac{C_{12}^2}{C_{11}}$$ **Equation 3**

where C_{ij} are the components of the stiffness tensor of the film.

Dislocations have broken bonds and strain fields associated with them; consequently, their presence introduces a discrete energy into the system. The energy per unit area of an array of dislocations whose average distance, S, apart is given by

$$E_d = \left(\frac{1}{S}\right)\left[Db(1 - \nu\cos^2\alpha)\right]\left[\ln(R/b) + 1\right]$$ **Equation 4**

where b is the Burgers vector of the dislocation, ν is the Poisson's ratio, α is the angle between the Burgers vector and the dislocation line, R is the outer cut-off radius of the dislocation core and D is an average shear modulus given by Equation 5 below.

$$D = G_f G_s b/\pi(G_f + G_s)(1 - \nu)$$ **Equation 5**

G_f and G_s are the shear moduli of the film and substrate respectively. Using Equation 4 and the fact that the amount of plastic strain relieved is given by, $\delta = f - \varepsilon = b_{eff}/S$, the dislocation energy per unit area, E_d is:

$$E_d = D\left(\frac{b}{b_{eff}}\right)(1 - \nu\cos^2\alpha)(f - \varepsilon)\left[\ln(R/b) + 1\right]$$ **Equation 6**

The total energy of the system, therefore, is the sum of elastic and dislocation energies expressed as $E_{tot} = E_\varepsilon + E_d$. One can take the derivative of the total energy expression with respect to elastic strain, set it to zero and thereby derive a critical strain. The critical thickness, therefore, is the thickness at which this critical strain occurs and is given by Equation 7 as long as $h_c < S/2$.

$$h_c = \frac{D\left(b / b_{eff}\right)(1 - \nu\cos^2\alpha)(f - \varepsilon)\left[\ln(h_c / b) + 1\right]}{2Yf}$$ **Equation 7**

2.3. Dislocations

2.3.1 Different types of dislocations

In this work three different types of dislocations are encountered and to understand these dislocations, some background will be given. The primary-slip system in Face-Centered Cubic (FCC), diamond and zinc-blend structures is the a/2<110>{111} slip system. These are the type of dislocations that are most often reported. The slip systems notation described the Burgers vector and the slip plane. Thus a/2<110> is the Burgers vector and {111} is the slip plane. These dislocations are often called 60° dislocations, because when using a (001) substrate the angle, α, between the line direction, <110>-type directions, and the Burgers vector is 60° for dislocations on the (001) plane. For 60° dislocations on the (001) plane, $b_{eff} = b/2$ and is depicted in Figure 2.4 showing that the line direction, $\vec{u}$, is along the <110>-type direction.

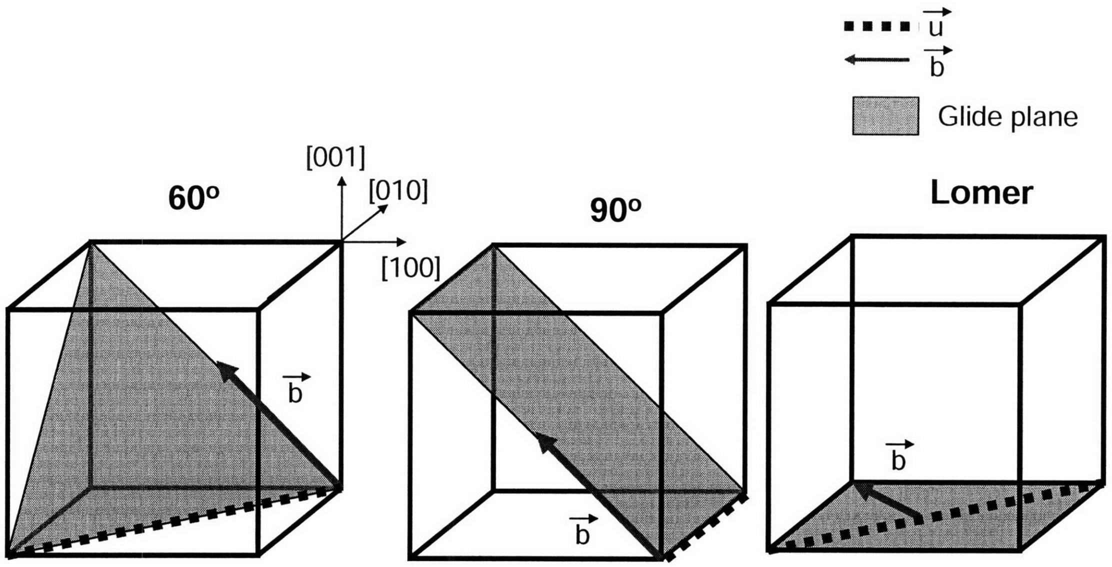

$$b_{eff} = \frac{b}{2} \qquad b_{eff} = \frac{b}{\sqrt{2}} \qquad b_{eff} = b$$

Figure 2.4 Dislocations discussed in this work including the common 60° dislocation, the 90° dislocation and the Lomer dislocation. All of these dislocations have a a/2<110>-type Burgers vector. The Lomer dislocation is the only sessile dislocation of the three as its Schmid factor is zero on the (001) surface.

The other dislocations discussed in this work include secondary-slip 90° dislocations and sessile Lomer dislocations, also depicted in Figure 2.4. The 90° dislocation belong to the a/2<110>{110}-slip system. 90° dislocations glide on {110}-type planes and, because the intersection of {110}-type planes on the (001) surface is along <100>-type directions, have <100>-type line directions. 90° dislocations have a larger b_{eff} than 60° dislocations and the largest schimd factor which resolves the shear stress onto the glide plane. The Schmid factor is large for 90° dislocations partly because their glide plane is 45° from the surface plane. The Schmid factor, M, is given by the equation below

$$M = \cos\lambda \cos\varphi \qquad \textbf{Equation 8}$$

where λ is the angle between the Burgers vector and the normal (in the film plane) to the line that is formed by the intersection of the film plane and the glide plane. The angle, φ, is the angle between the film plane and the normal to the slip plane.

Like secondary-slip dislocations, Lomer dislocations are also 90° dislocations since they are pure edge. Lomer dislocations are thermodynamically more favorable because they have the maximum effective Burgers vector, $b_{eff} = b$. However, unlike the previously mentioned 90° dislocations, Lomer dislocations are sessile, cannot glide, when formed on a (001) growth surface because their Schmid factor is zero. Lomer dislocations belong to the a/2<110>{100}-slip system. As a consequence, Lomer dislocations have only been observed to form via dislocation reactions[8] or, thought to be formed through the coalescence of islands during the initial layers of growth of a lattice-mismatched material[7]. However, because their Schmid factor is zero, unlike the 60° and 90° dislocations do not often form.

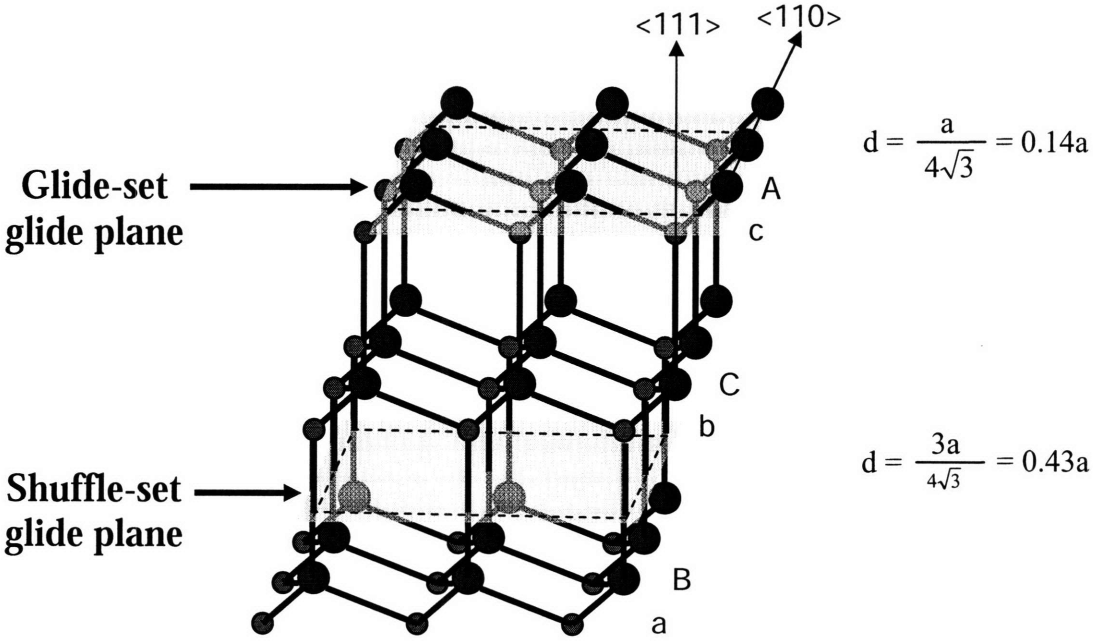

Figure 2.5: Possible glide planes for 60° dislocations in a zinc-blende crystal. 60° dislocations in diamond structure materials are similar except that instead of the structure having two different atoms, all of the atoms are the same. Both sets have <111>-type slip planes; however, owing to the fact that there are two atoms for every FCC lattice point, there are two types of <111> planes. The letters to the right lower case and capital A, B, and C are the index of each plan of atoms. The equations on the right refer to the interplanar spacing, d, and the lattice constant, a, for each of the slip planes. Glide-set dislocations 60° dislocations are most often observed given by the fact that partial dislocations are often observed[9, 10].

Unlike with Lomer and secondary-slip 90° dislocations, there is an added level of differentiation required for 60° dislocations in zinc-blende or diamond structure semiconductors. 60° dislocations in semiconductors can be of two types belonging to the shuffle- or glide-set. These two types of dislocations are differentiated by their different glide planes. Figure 2.5 shows the two different types of {111} planes in the zinc-blende structure.

The origin of the two different glide planes in zinc-blende and diamond structures derives from the fact that each FCC (Face-Centered Cubic) lattice point has two atoms associated with it, one at each FCC lattice point and one at $\left\langle \frac{1}{4}\frac{1}{4}\frac{1}{4} \right\rangle$. As is evidenced from Figure 2.5, the two different {111}-type planes have different interplanar-spacings, d, namely a shuffle plane, with d = 0.43a (a is that lattice constant), between planes with the same index (for example the plane depicted in Figure 2.5 between atoms of index B and b) and the glide plane, with d = 0.14a, between atoms of different indices (for example as in Figure 2.5 between atoms of index c and A).

Dislocations belonging to the glide-set whose Burgers vector is a/2<110> can dissociate into two partial dislocations of a/6<112>. Dislocations can not dissociate in the shuffle-set, however, because of the large energy required to do so[11]. Partial 60° dislocations are usually observed in semiconductors[9, 10] thus 60° dislocations usually belong to the glide-set and form because the dislocation energy is proportional to b^2[12]. A caveat to the formation and glide of glide-set dislocations lies in the fact that the planes associated with glide-set dislocations are much closer ($d \sim 0.14a$) then in the shuffle-set ($d \sim 0.43a$). For this reason the Peierls stress is expected to be larger for glide-set dislocations whose origin is thought to be from the frictional force associated with shearing atomic planes across each other.

Chapter 3. Phase Separation

3.1. Phase Separation in Compound Semiconductors

Phase separation was observed in many of the materials studied in this work. Phase separation proved to be deleterious to material quality and was avoided when possible. For this reason, a brief background on phase separation is presented. The body of literature calculating phase diagrams in III-V semiconductors is extensive and seemingly contradictory at times. Various work exists on the subject using different approximations and techniques like using a valence force field approximation[13] or by calculations from first principles[13]; in addition, some works account for coherency strains[14, 15] (first suggested by Cahn[16]) and others do not[17, 18]. Seemingly more understood is that, III-V semiconductors are expected to phase separate at low temperatures because of their positive enthalpies of mixing[19, 20].

Initially, when some phase diagrams for zinc-blende semiconductors were calculated de Cremoux and Stringfellow used only the energy term due to chemical considerations (comparing the spinodally decomposed state to the random alloy)[17, 18]. Later those same authors considered elastic coherency terms (terms associated with changing the lattice constant in the matrix when phase separation occurred) and found a suppression of the spinodal decomposition critical temperature[14, 15]. The suppression of the spinodal region with the inclusion of the elastic coherency term makes intuitive sense as phase separation induces composition deviations and (in most compound semiconductors except AlGaAs) thus cause lattice-mismatch relative to the matrix. The change in lattice constant will, in turn, induce elastic lattice distortions and will increase the energy required to enable phase separation to occur thereby suppressing the spinode.

Figure 3.1 illustrates the effect of the addition of the coherency strain term in the InGaAsP materials system calculated by Stringfellow[14, 18]. Note that with the addition of the coherency strain term, the spinodal region reduces in size.

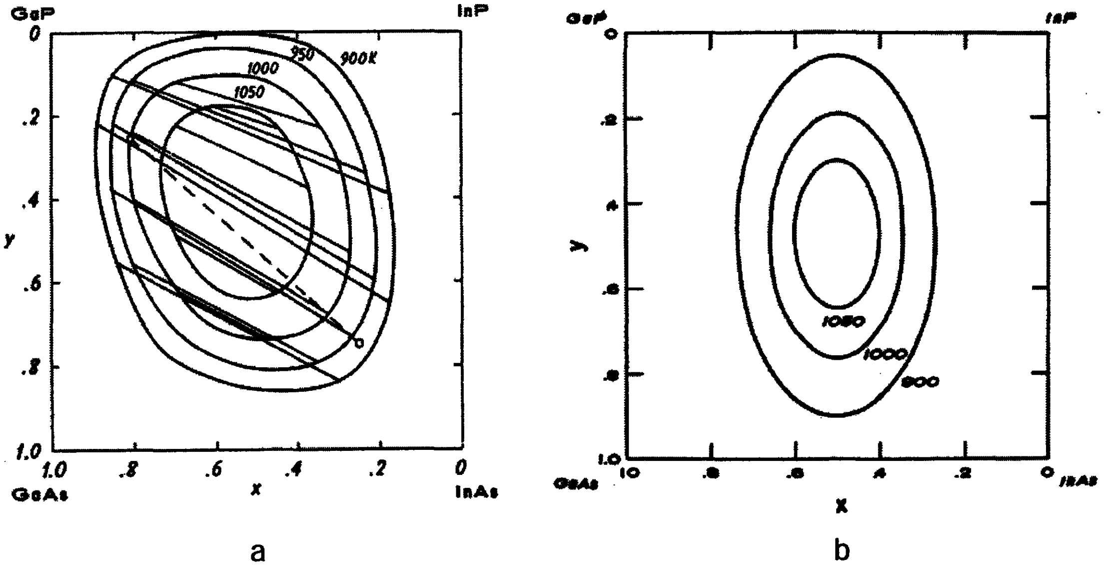

a

b

Figure 3.1 Phase diagrams for InGaAsP materials systems without (a) and with (b) coherency strain terms calculated by Stringfellow in [18] and [14], respectively. Note that the spinodal region decreases when the coherency term is included as the coherency term adds energy to any process that causes a lattice-mismatch.

There remains a disjunction between calculated phase diagrams and experiments, however. Even if one uses the phase diagram with a larger phase separated region that does not include coherency terms, in this work and in other works[21-24] phase separation is still observed at even higher temperatures than those predicted by Stringfellow in the InGaAs and InGaP materials systems. The observation of phase separation at temperatures higher then expected by calculations suggests either a missing energetic term that should be considered or a problem with the models used.

As an added level of confusion, no work known to the authors has been published on phase separation at a surface under MOCVD growth conditions. Without any other considerations due to MOCVD growth at a surface, the expected coherency strain terms should yield a phase diagram intermediate to those depicted in Figure 3.1(a) and (b). This is because at the surface, the film would experience some coherency strain due to the substrate; but, not as much as if it were in the bulk. Given the confusing state of the literature and the fact that the calculated phase diagrams do not accurately predict the results of experiments, the specifics of predicted phase diagrams will not be address further. Instead some basic concepts and trends of phase separation and phase diagrams will be discussed.

3.2. General Phase Separation

Spinodal decomposition is expected if the enthalpy of mixing is positive in the Gibbs free energy expression, Equation 9 below. Stingfellow and Zunger have calculated that the enthalpy of mixing, ΔH, in compound semiconductors is positive[19, 20] implying that spinodal decomposition and phase separation is likely at sufficiently low temperatures.

$$\Delta G = \Delta H - T\Delta S \qquad \textbf{Equation 9}$$

where G is the Gibbs free energy, T is the absolute temperature, and S is the entropy.

Spinodal decomposition arises from the fact that the Gibbs free energy, ΔG, becomes concave down at some compositions and temperatures. This occurs at sufficiently low temperatures when the enthalpy of mixing, ΔH, is positive. The Gibbs free energy is the sum of these enthalpic and entropic terms, shown schematically in Figure 3.2(a), for a temperature T greater then the critical temperature (T_c) above which spinodal decomposition does not occur. If the magnitude of the entropic terms is about the same as that of the enthalpic term, the Gibbs free energy will, for some composition, be concave down. The situation where the Gibbs free energy becomes concave down occurs at temperature below T_C. Figure 3.2(b) plots the Gibbs free energy versus composition for four different temperatures all of which are below T_C. That the temperatures are below T_C is evident from the fact that the concavity of ΔG is negative in places unlike in Figure 3.2(a). The arrow in Figure 3.2(b) indicates increasing temperatures; this is evident as the composition range where there is the negative concavity decreases.

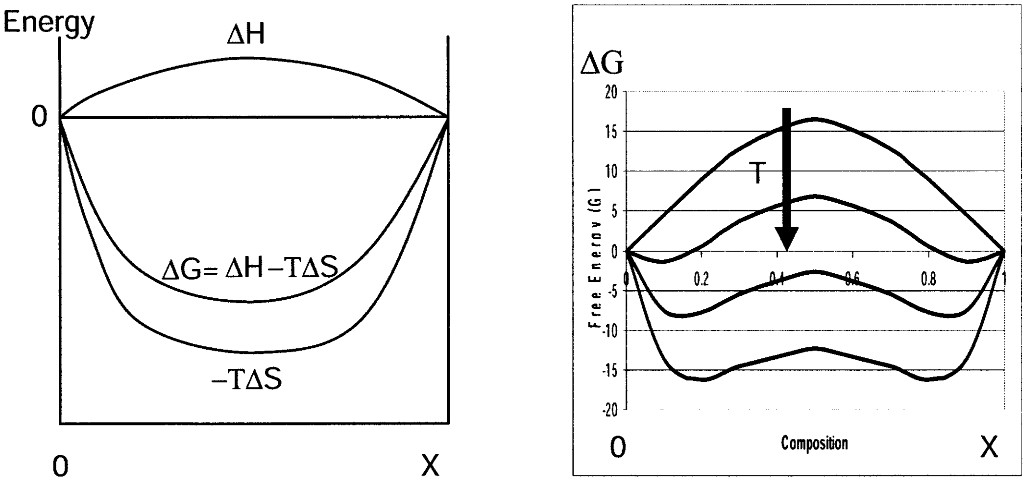

a b

Figure 3.2 Schematic figures that have spinodal decomposition. In (a) the enthalpic (ΔH) and the entropic (-TΔS) terms combine to form the Gibbs free energy at a temperature, $T > T_C$, where T_C is the critical temperature above which no spinodal decomposition is favored. In (b), the Gibbs free energy as a function of composition is plotted for various temeperatures T all of which are less then T_C as evident from the change in concavity of the Gibbs free energy for four different temperature. The arrow marks the direction of increasing temperature.

The phase diagram (bottom of Figure 3.3) for a materials system can be derived by knowing the Gibbs free energy curves (top of Figure 3.3) at a number of different temperatures. This process is shown schematically in Figure 3.3 for temperatures T_1, T_2, and T_3 all of which are lower the T_C. First to plot the edges of the miscibility gap (where the nucleation and growth region begins) one must determine the compositions at which a common tangent can be drawn on either side of the concave down portion of the Gibbs free energy curves. These points of common tangency are then mapped to the phase diagram through the vertical lines at the temperature the curve came from. The boundaries of the spinodal region at a given temperature (not marked with vertical lines), occurs at the composition where the change of concavity in the Gibbs free energy curve occurs. The spinodal regime is different from the nucleation and growth regime because unlike within the nucleation and growth regime, within the spinode the system is unstable to small perturbations in composition as all fluctuations reduce the Gibbs free energy. The nucleation and growth region on the other hand is stable to small fluctuations and requires larger fluctuations to occur to reduce the free energy of the system.

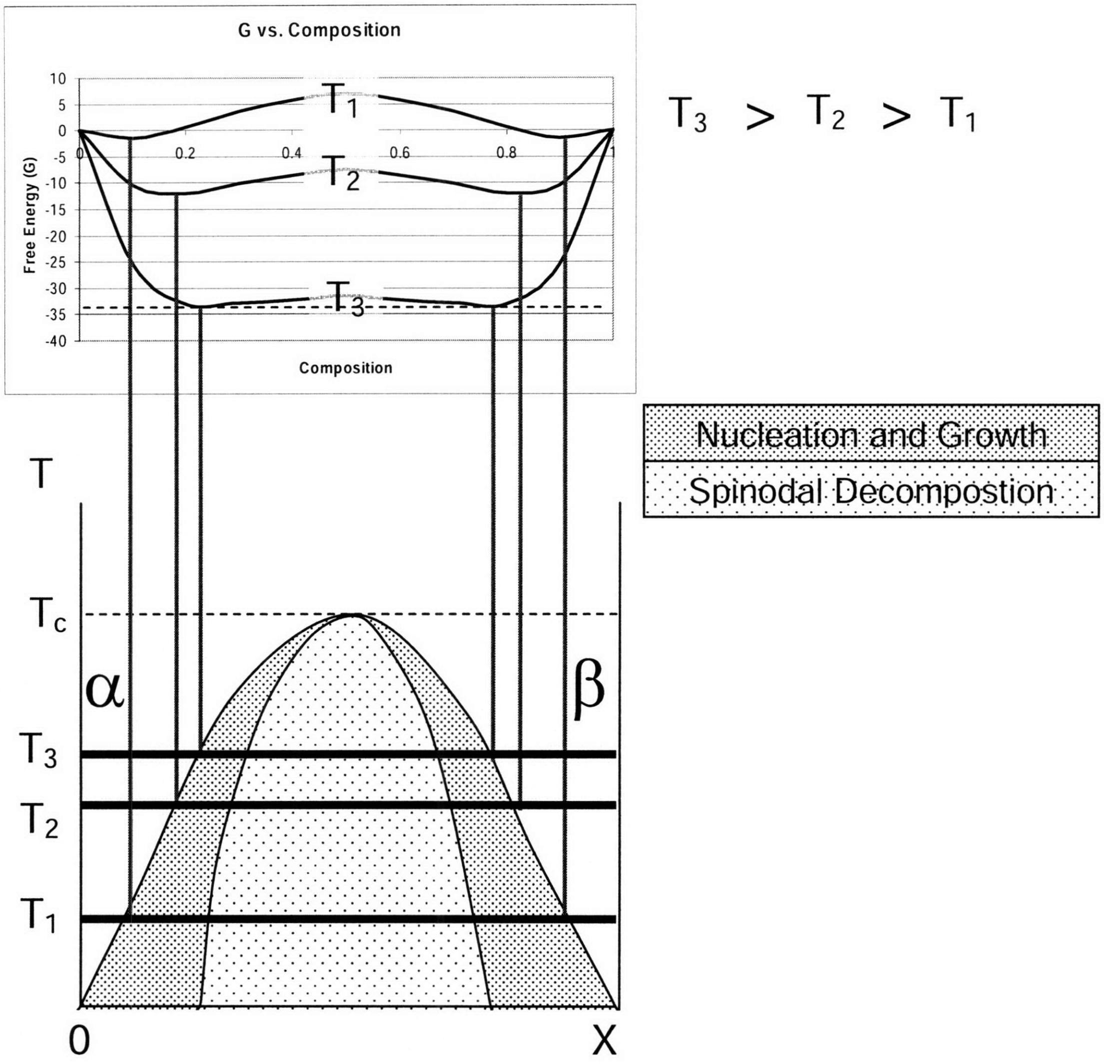

Figure 3.3 A schematic illustration of how the Gibbs free energy curve (top) determines the phase diagram (bottom). When the free energy curve becomes concave down, the tangent to the curve at the lowest points dictate the location of the miscibility gap as illustrated at temperatures, T_1, T_2, and T_3. Though harder to see in this figure and not traced out, the composition, at a given temperature, where the concavity changes marks the beginning of the spinodal region of the phase diagram.

3.3. Avoiding Phase Separation

As phase separation was not desired in the materials grown in this work the trends to reduce or eliminate phase separation are examined. In looking at a standard phase diagram, there are two experimentally controlled parameters to affect the miscibility of the system, temperature and composition. One trend is that if phase separation is observed at a particular composition and temperature, an increase in temperature could avoid phase separation. Another way to avoid phase separation is to change the composition at a given temperature. In looking at the phase diagram in Figure 3.3, compositions close to the pure components, pure X for example, are miscible. Consequently, if phase separation is observed and avoiding phase separation is desired, then one can increase the temperature of the system or the composition could be changed to a composition closer to a pure substance.

Chapter 4. Integration of Materials

4.1. Introduction

Direct growth of materials with large lattice-mismatches onto a substrate yields high dislocation densities as is depicted for Ge on Si and InP on GaAs in Figure 4.1(a) and (b), respectively. The large threading dislocation density ($\rho_t > 10^8/cm^2$) is due to enhanced dislocation nucleation from the large lattice-mismatch, f ~ 4%. This nucleation will be discussed later.

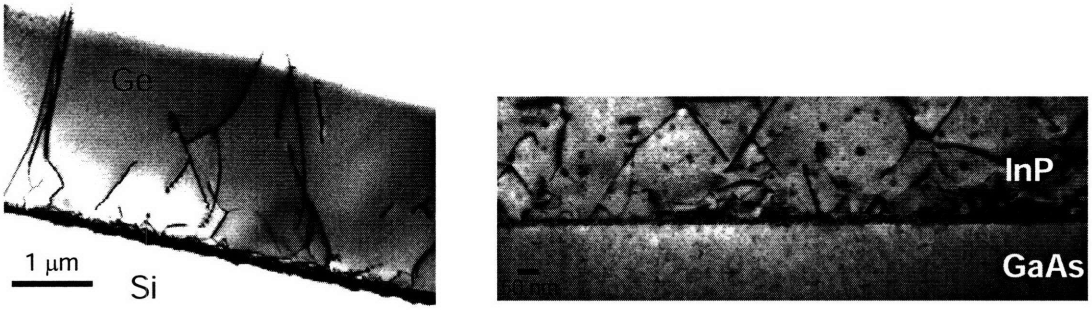

a b

Figure 4.1: Highly mismatched compressive films. Ge directly grown on Si is depicted in (a) reproduced from Langdo[25]. InP directly grown on GaAs is depicted in (b). Notice that many dislocations intersect the surface in each film each with about 4% lattice-mismatch leading to a threading dislocation density > $10^8/cm^2$.

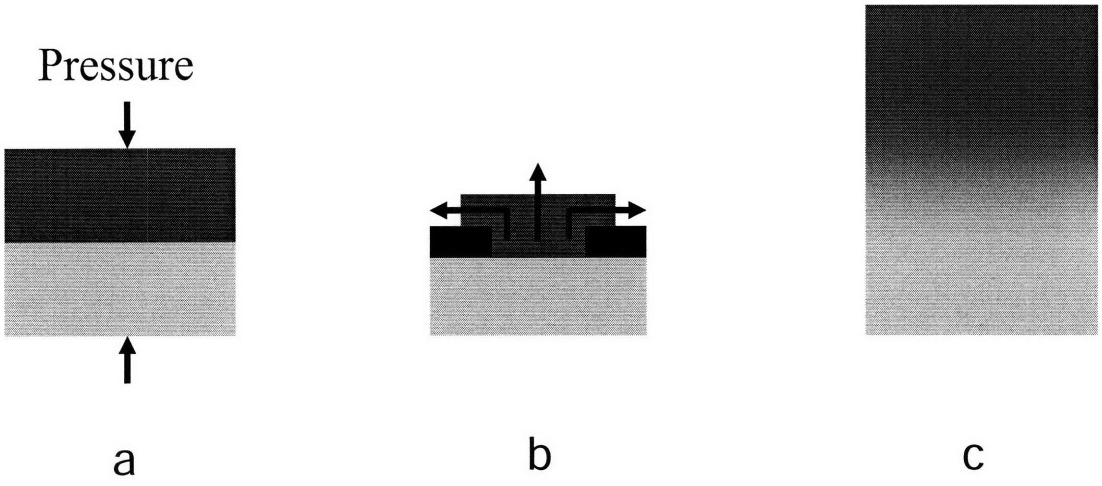

Figure 4.2 Three different methods of integrating materials together (a) bonding, (b) Epitaxial Lateral Overgrowth, a small area technique, and (c) compositionally graded buffer.

To avoid the large threading dislocation densities and microstructures depicted in Figure 4.1 and maintain good crystal quality, there are three main methods to integrate high-quality materials together: bonding, small area growth techniques, and compositional grading. These techniques are schematically depicted in Figure 4.2.

Bonding, the first technique schematically depicted in Figure 4.2(a), can be achieved by bonding two materials directly or through the use of some type of interlayer, like a transient liquid phase[26]. Typically bonding requires elevated temperatures and pressures. The primary advantage of bonding is that each material can be independently fabricated using the best process for that material and then brought together. In this way both materials, say Si and GaAs, are of high-quality before and after the bonding process. A limitation of bonding, however, lies in the choice of the materials that can be bonded together. The limitation stems from the need to have bulk materials strong enough to manipulate and bond together. For this reason only materials able to be produced in bulk can be bonded together. An added limitation embedded in the previous argument is the limit of available sizes of bulk materials. For example, in trying to bond say GaAs to Si, one is limited by the smaller size of the GaAs wafer.

Direct bonding, bonding of the two materials directly together without the use of an interlayer, is particularly difficult to accomplish on a reproducible level with a large area because the process is so sensitive to particles and surface roughness. Bonding using an interlayer, for example a transient liquid phase, is much more forgiving to particles and surface roughness but may not have the thermal budget of direct bonding as the interlayer usually has a lower melting point. Regardless of the method of bonding, bonding is typically limited to about 100 mm in diameter because of the differences in thermal expansion coefficients. With the other two methodologies shown in Figure 4.2(b) and (c), materials not available in bulk can be integrated, for example $Si_{0.5}Ge_{0.5}$ can be integrated on Si.

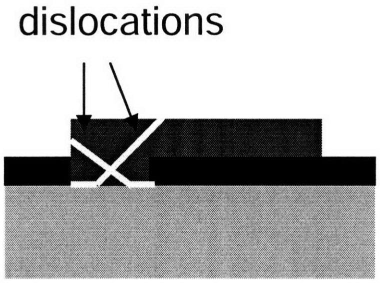

a

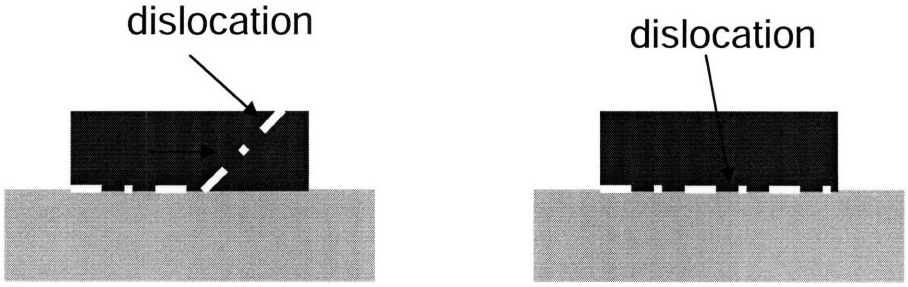

b

Figure 4.3 Two small area growth techniques for lattice-mismatched materials. (a) represents the necking process that can occur in ELO. In (b) a dislocation that intersects the growth surface can be made to glide out of the edge of a mesa through more growth or thermal cycling.

Small area growth techniques, like epitaxial lateral overgrowth (ELO) [27], or patterned substrates[28, 29] can be used to integrate high-quality materials. Two small area growth techniques are depicted in Figure 4.3. First in ELO, through a process reminiscent of necking in crystal pulling, dislocations may be forced to exit the crystal because of the geometry of the glide planes in the vicinity of where the crystal was seeded as depicted in Figure 4.3(a) (for example, dislocations in Zinc-blende and Diamond structure materials usually glide on {111}-type planes). In this way, areas away from the seeded region can be made free of dislocations. Another small area technique to reduce ρ_t is through patterning. By growing in a small area less than 100 μm and more typically on the order of 1 μm lateral dimensions[28], the likelihood a dislocation will glide until it reaches the edge is high thereby ensuring a low density of dislocations at the surface where devices typically reside. If dislocations, as grown, do not exit through the side of one of these mesas, thermal cycling may drive the dislocation along until it does[29]. This process is schematically depicted in Figure 4.3(b) where a dislocation that initially intersected the surface continues to glide out of the side of the crystal. As mentioned earlier, small area growth techniques allow commercially unavailable lattice constants and materials. However, the major drawback for these methods is that the small areas grown are too limiting for use in most commercial applications.

Graded buffers (unlike small area growth techniques) enable large areas and (unlike bonding) enable commercially unavailable lattice constants. There are drawbacks to graded buffers as well, however. The first is that only materials with a similar crystal structure to the substrate can be grown on that substrate. The second is that typically thick films must be grown, and the larger the lattice-mismatch (f) between the two materials, the thicker the graded buffer has to be due to dislocation engineering requirements. For example, to relieve a 4% lattice-mismatch a graded buffer has to be around 10 μm thick in order to allow for low enough dislocation densities to achieve working minority carrier devices[30, 31]. Previous results show that thinner graded buffers lead to an increase in dislocation density[32]; however, recent work by Gupta *et al.* suggests that with careful engineering the dislocation density can be minimized using a significantly thinner graded buffer[33].

4.2. Compositionally Graded Buffers

Since compositionally graded buffers are used extensively in this work, the strategies and requirements to maintain low ρ_t through the use of graded buffers will be discussed in some detail. As a preface to this discussion of graded buffers, a discussion of dislocations and the desired microstructure of a single lattice-mismatched layer is required to understand why graded buffers are important.

Misfit dislocations, those that reside at the film/substrate interface, are necessary to relieve the lattice-mismatch stress between two materials. Because dislocations must end at an interface and they deleteriously affect devices, ideally all dislocations would go from one end of the crystal to another, like the longer dislocation in Figure 4.4(a), thereby avoiding the growth surface where devices may reside. Since this is a difficult microstructure to achieve in crystals the size of semiconductor wafers (50-300 mm in diameter), it is desirable to have the longest misfit dislocations possible similar to the shorter dislocation in Figure 4.4(a).

Figure 4.4 depicts two possible dislocation microstructures that a single lattice-mismatched film could adopt to relax. The misfit dislocation length in both Figure 4.4(a) and (b) are the same indicating that both films are equally relaxed. The difference, then, lies in the number of dislocations required to produce this total misfit dislocation length which relaxes the film. In Figure 4.4(a), only two dislocations were required while, in Figure 4.4(b) five were required. As a result of needing more dislocations to relax the film the threading dislocation density, ρ_t (the density of dislocations that intersect the surface), is significantly higher in Figure 4.4(b).

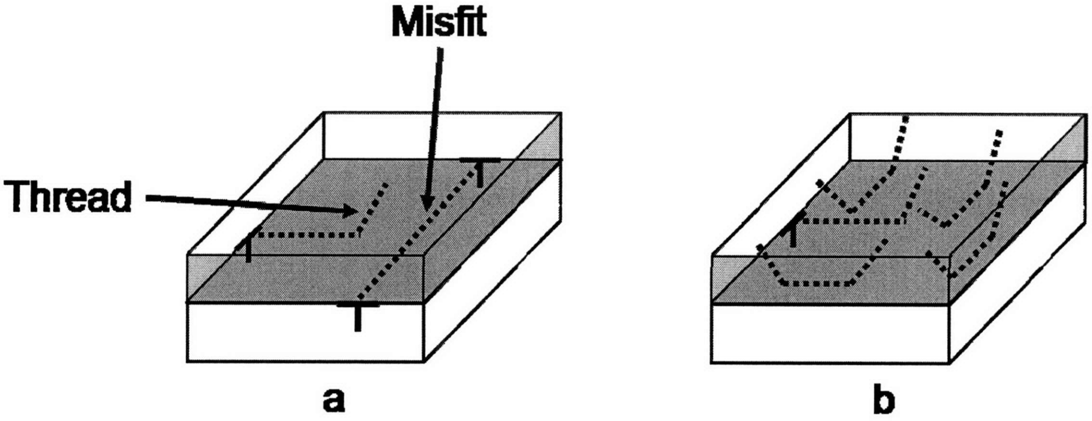

Figure 4.4: Schematic diagram comparing the microstructure of a low dislocation density material (a) with a structure with higher dislocation density (b). This figure is used to illustrate the various requirements in order to maintain a low threading dislocation densitiy.

In order to obtain the dislocation morphology depicted in Figure 4.4(a) (a morphology consisting of long misfit dislocation length and low ρ_t) in a single lattice-mismatched layer two conditions must be met: new dislocation nucleation must be minimized and fast dislocation glide must be enabled. Limiting dislocation nucleation is critical to maintaining low ρ_t and can be achieved by growing a small lattice-mismatched material on the substrate as high large misfit enhances dislocation nucleation. With this in mind, the morphologies depicted in Figure 4.4(a) and (b) could correspond to two different films: one with a small and the other with a large lattice-mismatch, respectively.

Dislocation nucleation is also strongly influenced by the substrate orientation. Lee *et al.* have found that even with very small lattice-mismatches ($Si_{0.97}Ga_{0.03}$ on Si, f=0.12%) rampant dislocation nucleation is unavoidable for lattice-mismatched films grown on the (110), (111) and (112) wafer orientations[34]. Lee's results suggest that dislocation nucleation is suppressed on the (001) surface. The suppression of dislocation nucleation on the (001) surface may be why single crystal semiconductors have traditionally been pulled in this direction in Czochralski crystal growth[35]. Consequently, Figure 4.4(a) and (b) could correspond to the same lattice-mismatched film grown on two different substrate orientations, say, (001) and (110) respectively.

As mentioned earlier, fast dislocation glide is also required to minimize ρ_t. With this requirement in mind, Figure 4.4(a) and (b) could refer to films that have fast and slow dislocation-glide-velocity, respectively. Dislocation-glide-velocities are have been found to obey the semi-empirical equation below[36, 37].

$$v_{\perp} = C\varepsilon^{m}e^{(-E_a/kT)}$$ **Equation 10**

In this expression ε is the strain, T the absolute temperature, C and m are constants used as fitting parameters and E_a is the activation energy, and k is the Boltzmann constant. Consequently, in order to achieve a low threading dislocation density, one should increase the growth temperature of the film. Leitz *et al.* have performed this experiment and have seen an exponential decrease in ρ_t as the growth temperature is increased; their data is shown in Figure 4.5[38].

Examination of Equation 10 above may also lead one to think an increase in ε will increase the dislocation glide velocity, $v_\perp$, and decrease ρ_t as well. However, to increase ε one must increase the lattice-mismatch, f, and films with larger mismatches nucleate dislocations more easily.

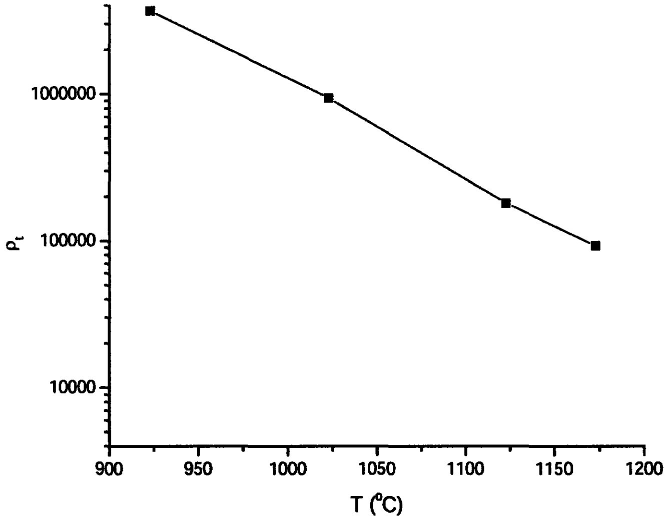

Figure 4.5 Threading dislocation density, ρ_t, versus temperature for graded buffers on Si to a final composition of $Si_{0.7}Ge_{0.3}$ from Leitz *et al*[38].

Even after using (001) substrates and growing small-lattice-mismatched films at high temperatures, one may still end up with a high threading dislocation density material. This unexpected increase in dislocation density after following the criteria outlined previously have been attributed to the arrest of dislocation glide[21, 39-42]. Dislocation glide can be arrested by surface roughness[39, 40], other dislocations[43], crystal defects[43, 44], high-energy boundaries[41, 42], branch defects[21], or composition variation caused by phase separation. In this way, Figure 4.4(a) and (b) could then correspond to materials where dislocations are free to glide and where dislocation glide is arrested, respectively.

Thus far only single lattice-mismatched layers have been discussed. A graded buffer can be imagined as a series of single lattice-mismatched steps. A successful graded buffer, therefore, is a series of small lattice-mismatched steps designed to maintain a low threading dislocation density. Part of the design of a graded buffer must be to ensure that each layer as it grows relaxes partially before changing the composition again. This process ensures that the next film is also only a small lattice-mismatch. In essence each step of a graded buffer must satisfy the criteria illustrated in the previous pages to ensure low threading dislocation density. Therefore each layer of the buffer must be: of small lattice-mismatch, on a (001) substrate, relaxed, grown at high temperatures, and without dislocation glide being arrested. As will be discussed later, these criteria can be difficult to achieve for each layer and composition. A schematic and a Cross Sectional Transmission Electron Microscopy (XTEM) micrograph of a largely ideal graded buffer along with a graded buffer whose misfit lengths are short are shown in Figure 4.6. The XTEM micrograph in Figure 4.6(b) has very short misfit lengths because dislocation glide was arrested by composition variations. This microstructure leads to high ρ_t. A successful graded buffer, on the other hand, prevents nucleation of new dislocations, the result is that existing dislocations are, in essence, recycled and used to relax each film in the graded buffer; this process is shown schematically in Figure 4.6(a).

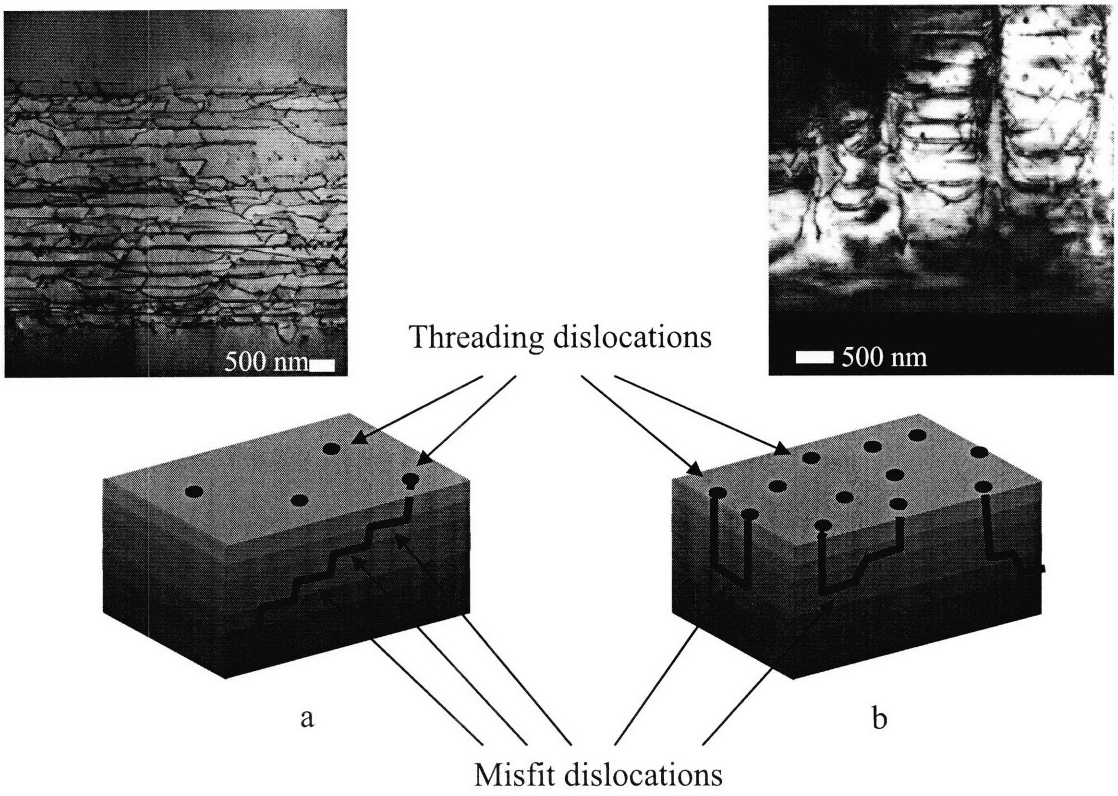

Figure 4.6 Schematic diagrams of a series of small lattice-mismatch layers that comprise a graded buffer. (a) shows how dislocations can continue to glide up through the graded buffer relieving lattice-mismatch at each interface thereby reusing existing dislocations without needing to nucleate new dislocations to relieve the lattice-mismatch. A XTEM micrograph of a graded buffer that successful reuses dislocations at each interface is shown above the schematic. In contrast to the graded buffer that reuses dislocations at each interface, (b) schematically depicts a graded buffer that has had to nucleate more dislocations to relieve the lattice-mismatch because of the short misfit dislocation lengths associated with each dislocation. Above the schematic is a micrograph where dislocations are being blocked by composition variations greatly increasing the threading dislocation density.

4.3. Motivation for the Routes Taken

At times dislocation inducing lattice-mismatch is required to achieve desired device characteristics. Compositionally graded buffers allow a larger amount of lattice-mismatch maintaining high-quality material over the whole wafer. Compositionally graded buffers require knowledge about dislocation nucleation and dislocation control.

Implementation of graded buffers have been used in a number of different semiconductor systems to be able to integrate high-quality materials together including the SiGe on Si[39, 45, 46], InGaAs on GaAs[41, 42], and InGaP on GaP[21].

Much work has been done in the SiGe materials system to not just integrate Ge onto Si[39, 45, 46]; but, to use lattice constants in between that of Si and Ge to enhance mobilities of electrons and holes[47]. In addition, the SiGe graded buffer has been used to enable the first reproducible, room-temperature, epitaxially grown GaAs based lasers on Si[31]. This work seeks to go beyond the GaAs lattice constant towards InP and to lead the way towards InP grown on Si.

From results from this study, it was clear fairly early that a high-quality $In_{0.34}Ga_{0.66}As$ graded buffer could be grown to which has a lattice constant over half way between that of GaAs and InP. However, the InGaAs materials system could not be used to further increase the lattice constant towards InP because we find that phase separations causes dislocation blocking. Consequently, the research split into two routes in an attempt to achieve high-quality InP on GaAs. The first route involved using other III-V materials systems enabled by of the added degrees of freedom associated with ternary and quaternary III-V semiconductors. Eventually, a graded buffer using the InGaAs and InGaP materials systems yielded high-quality InP on GaAs. This work is discussed first.

The second route attempted to use the $In_{0.34}Ga_{0.66}As$ platform as a platform on which thin InP layers were grown. It is known that InP grown directly on GaAs leads to very high threading dislocation densities. However, InP on this $In_{0.34}Ga_{0.66}As$ platform had never been attempted and it was hypothesized that the InP would relax controllably without much dislocation nucleation. Dislocation nucleation was extensive, however, and the InP film relaxed via a secondary-slip system.

Chapter 5. Characterization Methods

5.1. Overview of Characterization Methods

The primary methods used to characterize samples in this work are TEM (Transmission Electron Microscopy) and XRD (X-Ray Diffraction). XRD was used to determine the composition and strain of the semiconductor films. TEM was used to determine the threading dislocation density as well as whether phase separation took place and, if it did, at about what composition it occurred in the graded buffers. XTEM was also used to determine film thicknesses and amount of plastic relaxation. Composition variations were determined by EDS (Energy Dispersive Spectroscopy) analysis in STEM, or by using moiré fringe calculations determined in TEM. The surface roughness and morphology was determined by AFM (Atomic Force Microscopy). PL was used to characterize the quality of graded buffers with InP lattice constants compared to bulk InP.

5.1.1 Transmission Electron Microscopy (TEM)

Transmission Electron Microscopy (TEM) is a powerful characterization technique in materials science. This technique is extremely sensitive to distortions in the lattice as these distortions yield diffraction contrast and can be used to determine, amount other things, the dislocation densities, types of dislocations, atomic displacements, and thicknesses of films. TEM was used extensively in this study; for that reason a brief introduction on the technique is in order. Hirsch *et al.*[48] and Fultz and Howe[49] have written excellent books for more discussion on TEM.

Transmission electron microscopy involves the use of electrons as waves to image samples at high magnifications. The wavelength an electrons is approximated by using the de Broglie equation below.

$$\lambda = \frac{h}{m_e v} = \frac{h}{\sqrt{2 m_e e V}}$$ **Equation 11**

where λ is the wavelength, h Planks constant, m_e the mass of the electron, v the velocity of the electron, e is the charge on the electron and V is the voltage the electron is accelerated through. A shorter wavelength (the higher the acceleration voltage of the electron) leads to a higher possible resolution.

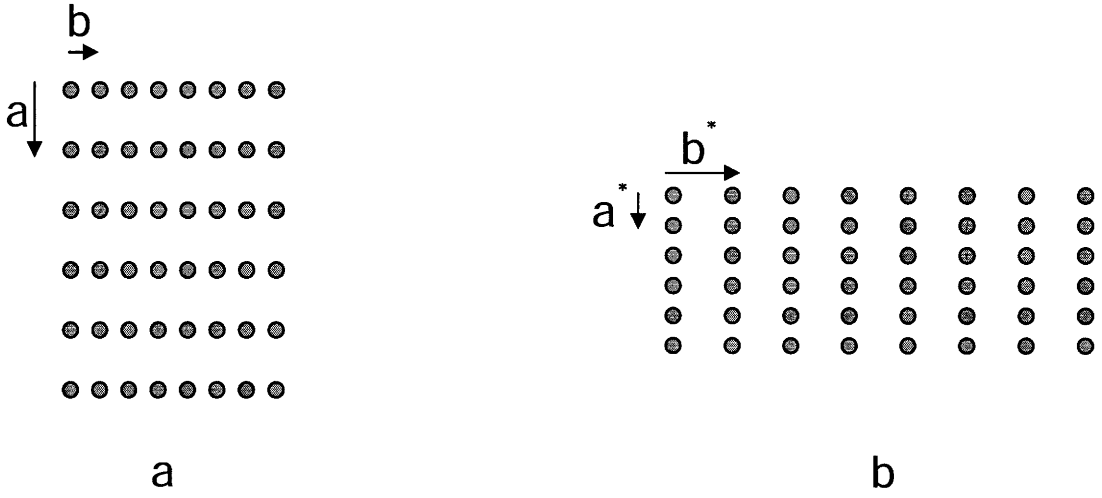

Figure 5.1: Real lattice (a) and a reciprocal lattice (b) in two dimensions. The relationship between the real lattice and the reciprocal lattice

It is useful to think bout the possible resolution of a given measurement technique using the reciprocal lattice and Ewald sphere construction. If there is a set of periodic scatters, say atoms, whose periodicity is a, b, and c, in the x, y, and z directions, respectively [see Figure 5.1(a)], one can construct a reciprocal lattice with similar periodicity to the real lattice accept the distances between the lattice points are $a^* = 1/a$, $b^* = 1/b$, and $c^* = 1/c$, respectively (see Figure 5.1(b)). The reciprocal lattice is a useful framework because one can construct an Ewald sphere (Ewald circle in two dimensions as depicted in Figure 5.2) whose intersections with the reciprocal lattice denote the conditions for constructive contrast. The size of the Ewald Sphere is governed by the wavelength of the incident wave with the radius of the Ewald sphere being the reciprocal of the wavelength of the incident wave. Figure 5.2 shows a reciprocal lattice with three Ewald circles corresponding to $\lambda_0 << \lambda_1 < \lambda_2$. The smallest wavelength, λ_0, could resolve the distance between the b atoms in the real space lattice; whereas the longest wavelength, λ_2, would only get diffraction spots from the atoms spaced b apart. (Diffraction occurs when the wavelength of light is on the order of the distance between scattering centers. However, to resolve the scattering centers, the wavelength of light must be a few orders of magnitude smaller then the scattering centers.) To illustrate the relationship between incident wavelength and resolution, the acceleration voltage for the electrons was 200keV in the microscopes used in this work, yielding a de Broglie wavelength for the electrons of about 2.7 pm while the point-to-point resolution (at least in the JEOL 2010) was 0.19 nm.

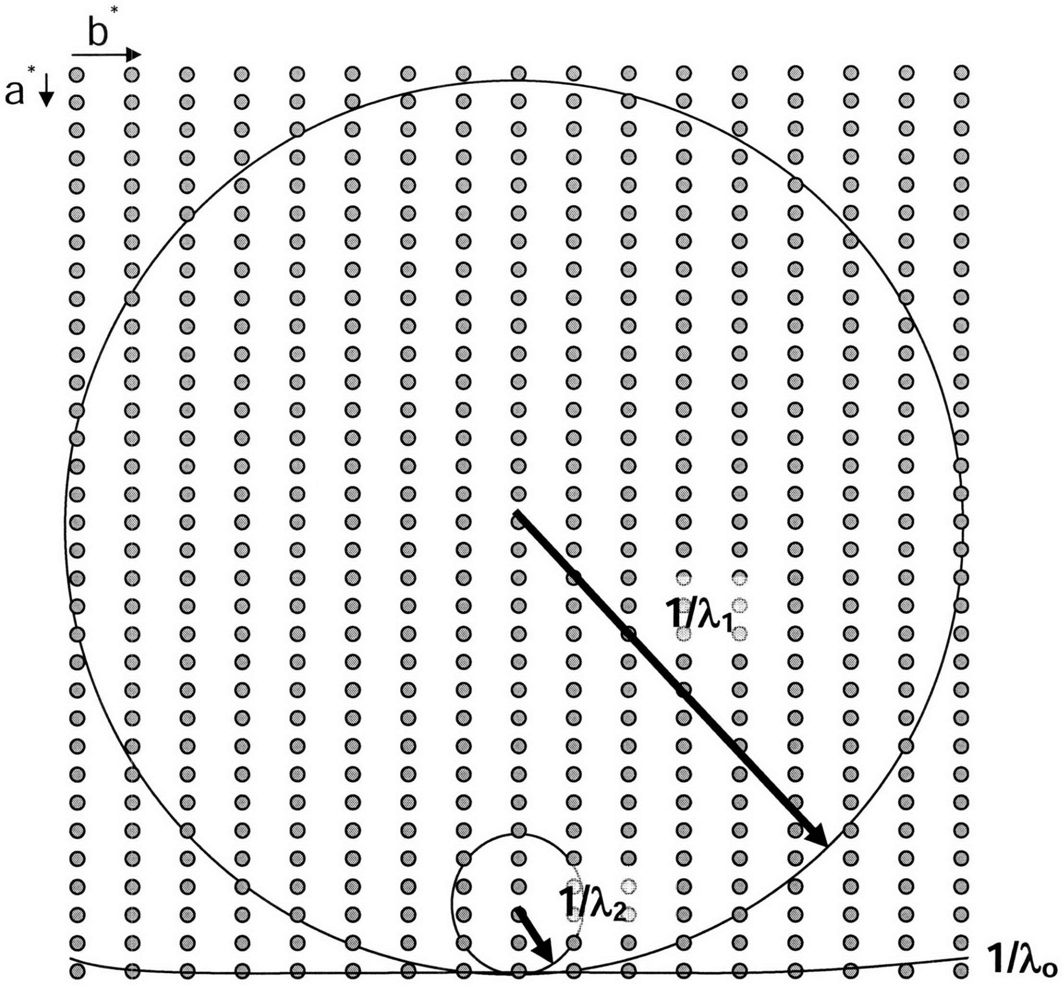

Figure 5.2 Reciprocal lattice corresponding to the crystal lattice in the previous figure with two Ewald spheres with radi of $1/\lambda_1$ and $1/\lambda_2$ with $\lambda_1 < \lambda_2$. A third Ewald sphere corresponding to $1/\lambda_o$ with $\lambda_o << \lambda_1$ is partially shown. As a consequence of the Ewald sphere with radius of λ_1 having a larger radius then λ_2, that Ewald sphere intersects the reciprocal lattice in more places and can thus have more constructive interference events. However, since the Ewald sphere corresponding to λ_o is significantly larger, many lattice points are on the sphere and the radiation of wavelength λ_o can resolve the distance between lattice points in the b direction.

The resolution in TEM has been explained; however, part of the power of TEM comes from the types of image contrast that TEM produces. Of the conventional types of contrast that can occur in TEM (diffraction, mass and thickness contrasts) diffraction contrast is usually the dominant form of contrast. In this work, diffraction contrast is observed from thickness and bend contours, dislocations, moiré fringes, stacking faults and strain fields. The standard diffraction conditions used in this work are the $\vec{g} = \langle 220 \rangle$ and $\vec{g} = \langle 400 \rangle$ two-beam diffraction conditions on the <110>-type poles for XTEM and the (001) pole for PVTEM (Plan View Transmission Electron Microscopy). Two-beam diffraction conditions a few degrees away from the pole were used to ensure a good two-beam condition and to best determine what diffraction condition the contrast seen in the micrograph was from.

In an ideal two-beam diffraction condition where there is only one excited diffraction spot, in addition to the transmitted beam, one can get two types of images. In this type of configuration a bright-field (BF) or dark-field (DF) image can be obtained if one selects electrons (using an aperture) from the transmitted or diffracted beam, respectively. The relationship between selection of a particular diffraction spot and the image obtained from that spot is illustrated in Figure 5.3. Electrons can be bent into a diffraction spot by bent planes in the sample as schematically illustrated in Figure 5.3. As a consequence of being bent away from the straight through condition (the straight through condition creates the bright-field image, BF), regions which caused the electrons to be bent appear dark in the BF image. These regions correspond to the bent planes. As these electrons were bent away into the diffraction spot, if one were to look at the electrons bent into the diffraction spot in the DF image one would see a bright image corresponding to the location of the bent planes. A perfect two-beam condition is never attained, however, as more then two diffraction spots are excited in practice. Consequently, there is not necessarily a one-to-one correspondence between the BF and DF images as discussed here. A good two-beam condition can be achieved by moving a few degrees away from the pole to minimize the excitation of other diffraction conditions.

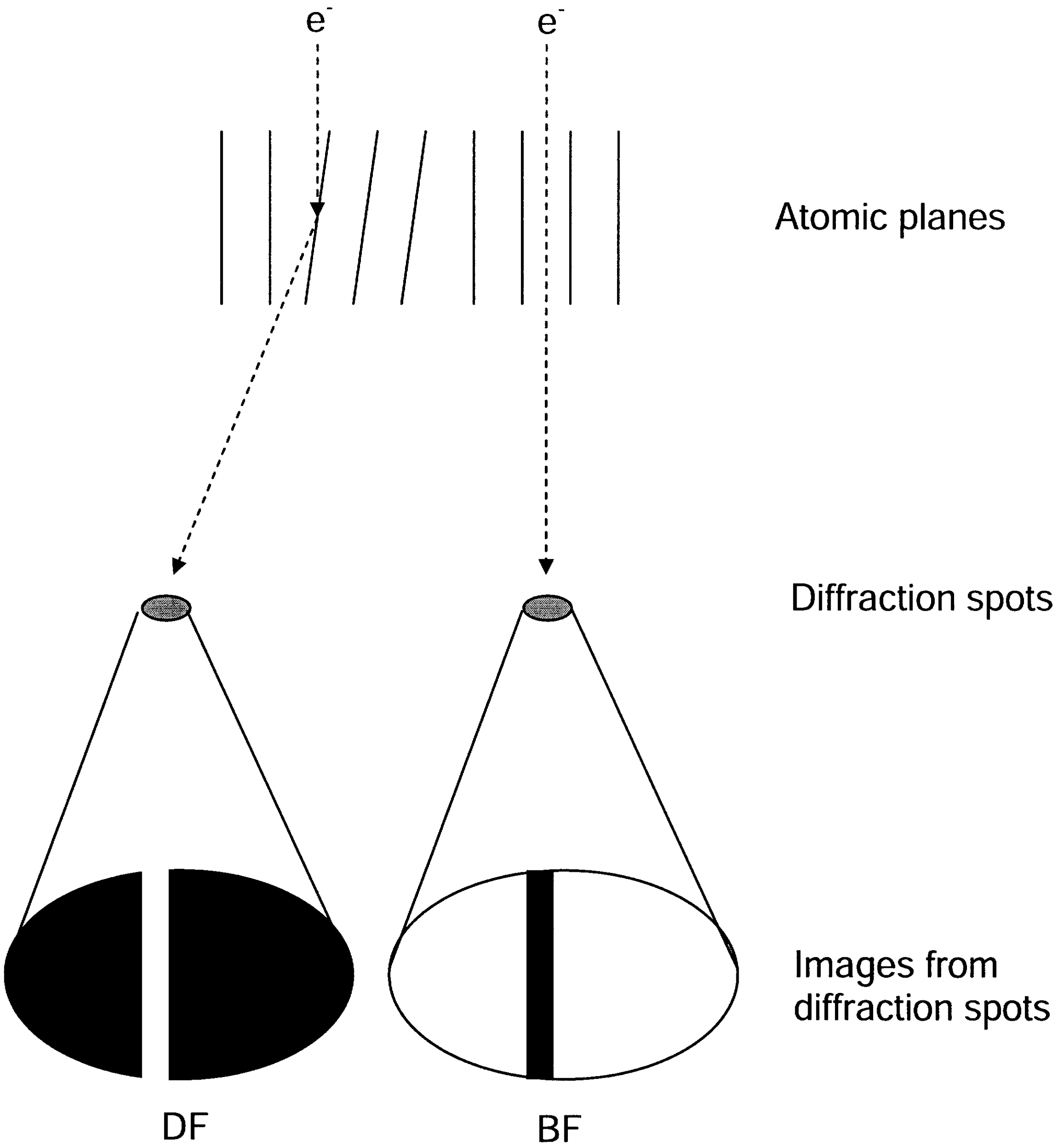

Figure 5.3 Schematic relationship between a TEM image and the lattice planes in a two-beam diffraction condition. The bent planes diffract electrons into a different diffraction spot. If one were to look at the image from that diffraction spot, one would see a bright region (in the dark field, DF, image) corresponding to the bent planes. However, since electrons are being bent from the straight through image (the bright-field, BF, image) the region of the image corresponding to those bent planes appears dark as the electrons are being diverted to the DF image.

TEM Methods

Two semi-quantitative TEM analysis methods were used in this study and outlined below: $\vec{g} \cdot \vec{b}$ analysis and calculation of interplanar spacing using moiré fringes. A powerful tool used in transmission electron microscopy is $\vec{g} \cdot \vec{b}$ analysis (or, more generally, $\vec{g} \cdot \vec{r}$ analysis) where $\vec{g}$ is the diffraction vector and $\vec{b}$ is the Burgers vector ($\vec{r}$ is the displacement vector). In $\vec{g} \cdot \vec{b}$ analysis one can determine the Burgers vector of a dislocation (or the displacement vector, $\vec{r}$). A dislocation (or other type of displacement) will go out of contrast, disappear, if the diffraction conditions satisfy the following two equations where $\vec{u}$ is the line direction along which the displacement occurs:

$$\vec{g} \cdot \vec{b} = 0 \qquad \textbf{Equation 12}$$

and

$$\vec{g} \cdot (\vec{b} \times \vec{u}) = 0 . \qquad \textbf{Equation 13}$$

(In the case of a displacement vector, $\vec{r}$, associated with some distortion in the lattice usually only the first equation, $\vec{g} \cdot \vec{r} = 0$, needs to be satisfied because almost invariably the line direction is perpendicular to the displacement vector.) Using this type of analysis one can determine what type of dislocations are present and what direction the displacement vector points offering information on the distortion of the lattice.

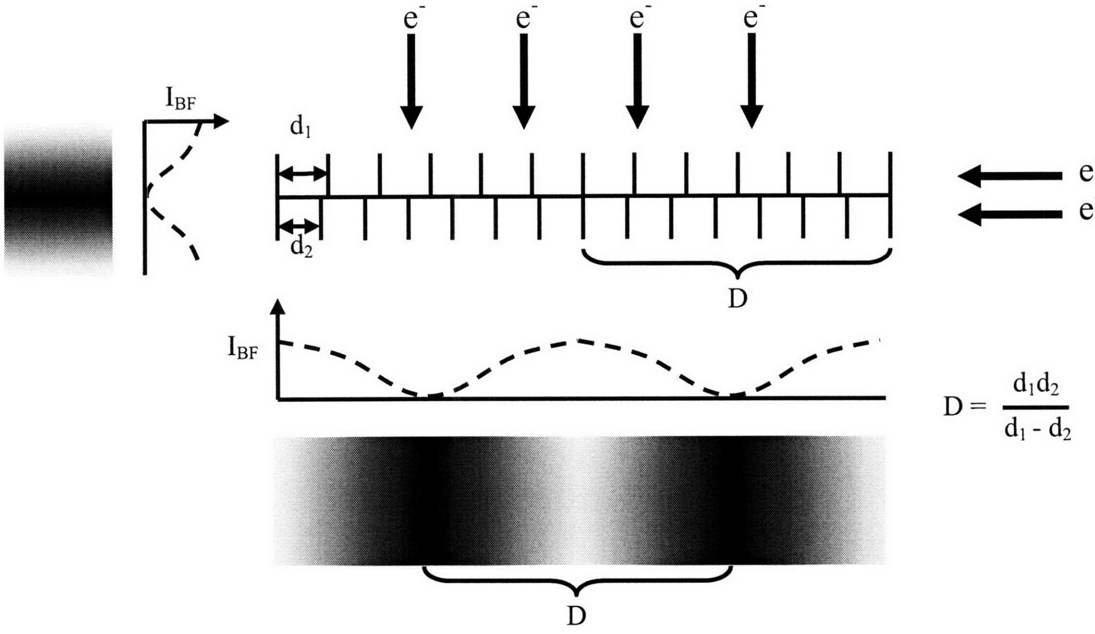

Figure 5.4 Diffraction contrast associated with changes in lattice sizes. If the electron beam is parallel to the interface where the lattice parameter change occurs (horizontal electron beam in the figure above), there may be a just one dark contrast region corresponding to the plane where the change in lattice constant occurs. However, if the electron beam is partially perpendicular (vertical electron beam in the figure above) to the change in lattice constant, moiré fringes can result with a characteristic wavelength D given by the equation above. I_{BF} is the intensity in the bright-field image as a function of distance.

Another type of diffraction contrast method used in this work to quantitatively calculate lattice parameter changes is moiré fringe contrast. Moiré fringe contrast results when the incident electron beam has a component perpendicular to an interface across which there is a change in lattice constant. This is schematically represented by the vertical electron beams in Figure 5.4. (In this work moiré fringe contrast was used to determine the lattice parameter of Ga enriched precipitates in the matrix.) When the electron beam is perpendicular to this interface, a characteristic wavelength, D, between contrast fringes occurs. By measuring D, in Figure 5.4, and knowing the interplanar spacing (d_1) in the matrix, one can determine the interplanar spacing (d_2) of the precipitate using the following equation:

$$D = \frac{d_1 d_2}{d_1 - d_2}$$ **Equation 14**

If the incident electron beam is parallel to the interface along which marks the change in lattice constant (the horizontal electron beam in Figure 5.4), then there is only one region with contrast (as opposed to the periodic contrast seen in the other direction) and that contrast region is associated with the interface itself.

More traditional two-beam condition TEM was used to determine threading dislocation densities throughout this work. TEM is the standard method by which other counting methods (like etch pit density, cathodoluminescence, spatially resolved photoluminescence, and electron beam induce current) of counting dislocations are measured against. The problem with using TEM to determine ρ_t is that for $\rho_t <$ $5\text{x}10^5/\text{cm}^2$ the amount of area needed to get a statistically meaningful ρ_t becomes unwieldy. However, TEM is the only methodology that can be employed for $\rho_t >$ $10^9/\text{cm}^2$ because the resolution by other methodologies is limited.

5.1.2 X-Ray Diffraction (XRD)

X-ray diffraction involves bombarding a material with electromagnetic waves whose wavelength is on the order of angstroms to determine interplanar spacing, orientation, or symmetry of a crystal. A brief description of x-ray diffraction will be discussed here, Cullity provides a more in-depth discussion on general x-ray diffraction[50]. For a more in-depth discussion on the details of how to extract lattice constants and tilts of epitaxial films from reciprocal space maps which was done in this work see [51, 52].

X-ray diffraction is a powerful technique which was used to determine the spacing between lattice planes in this work. As mentioned earlier, when an incident wave with wavelength, λ, interacts with periodic scattering centers whose periodicity is on the order of λ, diffraction occurs. This diffraction can be constructive or destructive; the standard condition for constructive x-ray diffraction on a lattice with planes distance, d, apart is the Bragg condition below.

$$n\lambda = 2d \sin\theta$$ **Equation 15**

where n is an integer and represents the order of reflection, and θ is the incident angle upon the lattice planes. A schematic of this situation for constructive diffraction is depicted in Figure 5.5(a). Figure 5.5(a) shows a symmetric scan configuration where the incident angle, θ_1, is the same as the reflected angle as referenced from the surface. The symmetric configuration enables the determination of the out of plane lattice constant, d_1, along the [001] direction. Figure 5.5(b) shows an asymmetric configuration so called because the angle of incidence is not equal to the angle of reflection from the point of view of the surface. The asymmetric configuration allows the determination of a lattice constant, d_2, having both in- and out-of-plane components d_3 and d_1, respectively. After determining d_1 and d_2 one can calculate d_3 and then determine the composition and strain of the film knowing the Poissons ratio. McGill goes through the equations to determine the composition, strain, misfit and relaxation from d_1 and d_3 in her thesis[53].

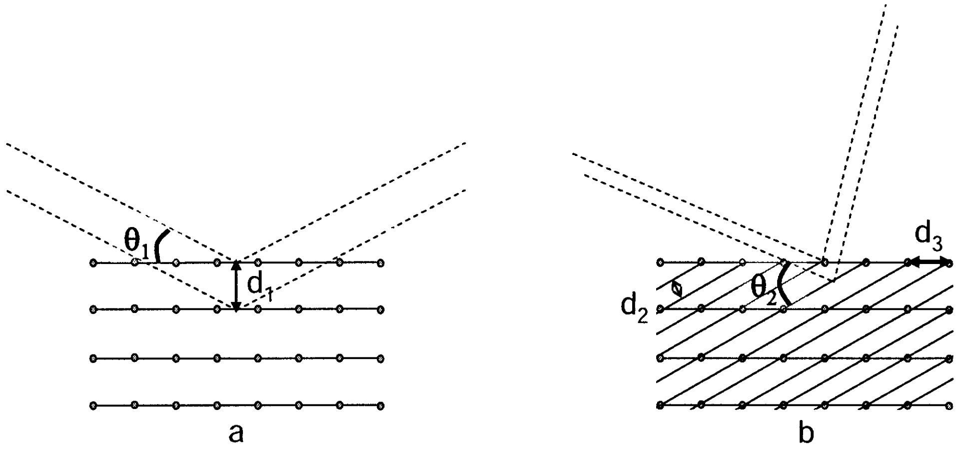

Figure 5.5 Incident light at an angle θ is constructively diffracted following Equation 15 above in two configurations symmetric (a), and asymmetric (b). The symmetric configuration named because the incident angle is the same as the reflected angle relative to the surface of the material can be used to determine the out of plane lattice constant, d_1 (the lattice constant along the [001] direction). The asymmetric configuration allows the determination of a plane, d_2, with in and out of plan components, d_3 and d_1 respectively.

5.1.3 Scanning Transmission Electron Microscopy (STEM) and Energy Dispersive Spectroscopy (EDS)

Scanning transmission electron microscopy (STEM) is very similar to TEM except that the location of the electron beam can be controlled and rastered in this technique across a sample. STEM (Scanning Transmission Electron Microscopy) in conjunction with Energy Dispersive Spectroscopy (EDS) is a powerful tool for elemental analysis. EDS examines the photon energy associated with deep level electron transitions and can thereby be used to identify which elements are present. Control of the electron beam in STEM is necessary to know which region of the sample the x-rays are coming from. In this work, STEM and EDS were used to determine that a compositional change caused the strain contrast viewed in TEM foils.

5.1.4 Atomic Force Microscopy (AFM)

Atomic Force Microscopy (AFM) is a very high-resolution technique for measuring the topology of a sample. Tapping mode AFM was performed in this study. Tapping mode involves bringing a sharp AFM tip close to the surface of the sample until it starts to interact with the surface. The resolution of an atomic force microscope can be better than one angstrom.

5.1.5 Photoluminescence (PL)

Photoluminescence (PL) is a method by which one can determine characteristic electron transitions within a material, like the electron transitions associated with the bandgap. PL involves illuminating a sample with light, usually a laser, whose photon energy is larger then that of the bandgap to excite free carriers that will later recombine and luminescence light whose energy is that of the bandgap. PL is a powerful tool to get a sense for the quality of a material, not just the bandgap. The quality of a film can be determined using low temperature and comparative PL. The FWHM (Full Width at Half Maximum) of the PL spectra may be due to thermal fluctuations or to defect states below the bandgap. At low temperatures, the thermal vibrations usually do not play a role in the observed FWHM; consequently, the FWHM observed is due to defect levels and is an indication of the quality of the material. Relative intensities from two samples can also be used to compare the quality of one material relative to another. To be quantitative, however, care must be taken to ensure that each sample is aligned exactly the same. Not all PL setups have this capability, as the one used in this work did not. Consequently, the relative intensities seen in this work is only qualitative.

Chapter 6. High-Quality InP on GaAs using Graded Buffers and Avoiding Phase Separation

6.1. Introduction

The properties of InP and other similar lattice constant materials enables state-of-the-art electronic and optical devices. The primary use for InP substrates is to supply the telecommunications industry with lasers and detectors at 1550 nm, the low absorption wavelength in SiO_2 fiber optics. To utilize the InP lattice constant for its electrical applications, near-lattice-matched InGaAs is used to enable a variety of high-performance electronics, including an HBT by Hafez *et al.* which achieved a record 604 GHz using compressive $In_{0.63}Ga_{0.37}As$ on InP[1].

Bringing the excellent optical and electrical properties of InP and related materials to other platforms, like GaAs and Si, offers both cost and performance benefits. InP wafers are expensive and typically small (2"-4") because they are used in fairly niche applications. In addition to the larger cost per area associated with fabricating smaller wafers, the use of small wafers also implies the use of older fabrication technology. To reduce cost and enable use of more state-of-the-art fabrication facilities, growth of high-quality InP on GaAs is a worthy goal, as InP devices could be manufactured in the lower cost GaAs infrastructure and also be monolithically integrated with GaAs devices to offer better performance.

The engineered accommodation of lattice-mismatch is needed in order to have high-quality InP on GaAs. Different methods can be employed to integrate high-quality lattice-mismatched semiconductors, including graded buffers, small-area growth techniques like ELO (Epitaxial Lateral Overgrowth), and direct bonding. Direct bonding ensures the quality of the material as the quality depends on the starting material. Direct bonding, however, limits integration to commercially availably materials which poses two drawbacks: (1) only discrete lattice constants are available, and (2) only particular diameters are available. In addition, even if conventional lattice constants and diameters are desired, and smaller wafer diameters are tolerable, there are technical roadblocks. For example, due to the differences in thermal expansion coefficients, when bonding GaAs to Si the largest area possible is limited to about 100 mm diameter even though Si is available as 300 mm wafers.

Unlike with bonding, small-area growth techniques and graded buffers both enable a continuum of lattice constants. These lattice constants between bulk substrates offer novel band offsets and may enable novel devices. The drawback of small-area growth techniques is that only areas on the order of 100 μm^2 or less can be high-quality. More typically to ensure high-quality material for larger mismatch systems, areas less than 1 μm^2 are required[28].

Graded buffers offer the solution to the drawbacks of each of the aforementioned techniques, allowing for a continuum of lattice constants with large areas limited only by the starting substrate. A drawback of graded buffers is that low threading dislocation densities in the final layer are dictated by dislocation velocities, and unhindered dislocation glide requires microns of thickness to relax the lattice and retain low threading dislocation density. Thinner films have been observed to increase the threading dislocation density, ρ_t[32].

We briefly review graded buffer layers in more idealized systems. For a more thorough review of lattice-mismatched semiconductors, see [7]. In idealized graded buffers on (001) substrates in diamond or zinc-blende semiconductors, existing dislocations glide along {111} planes leaving misfit dislocations at the substrate/film interface when the critical thickness, h_c, is exceeded [7, 54]. The misfit dislocations relieve the lattice-mismatch, f, between the substrate and the film given by

$$f = \frac{a_s - a_f}{a_f}$$ **Equation 16**

where a_s and a_f are the substrate and film lattice constants respectively. The extension of misfit dislocations by glide along the substrate/film interface allows more relaxation of the film without the need to nucleate new dislocations. Since dislocations must end at a surface, dislocation nucleation inevitably increases the number of dislocations that intersect the surface and is minimized in ideal graded buffers. These dislocation segments that intersect the surface are called threading dislocations. Because they enter device layers built on the surface, these threading dislocations degrade the electrical and optical properties by both serving as scattering centers to reduce free carrier mobilities as well as providing a band gap state where electrons and holes recombine to reduce the minority carrier lifetime. As a result, a common figure of merit for materials is the threading dislocation density, ρ_t, and it is used extensively in this work as the primary figure of merit. Both ideal and non-ideal graded buffers contain threading dislocations; the difference is in the number. An ideal graded buffer will have ρ_t in the low $10^6/\text{cm}^2$ or lower, good enough for minority carrier devices like lasers[30, 31], while a non-ideal graded buffer will have a larger ρ_t. A schematic representation of an idealized graded buffer is shown in Figure 6.1(a) with a XTEM (Cross Sectional Transmission Electron Microscopy) micrograph of a fairly ideal graded buffer.

A non-ideal graded buffer involves deviations from what was described above usually by either the existence of obstructions which pin dislocations and/or inducing rampant nucleation of new dislocations, both of which result in large ρ_t. The later, uncontrolled and rampant dislocation nucleation, can occur on non-standard, non-(001), wafer orientations[34]; or occurs with the deposition of a film with a large lattice-mismatch[7]. The former, dislocation pinning, has been attributed to surface roughness and microstructures with diffraction contrast observed in transmission electron microscopy (TEM). Surface roughness has been seen to pin dislocations[39, 55, 56] and CMP (Chemical-Mechanical Polishing) has been used to reduce the surface roughness and prevent dislocation pinning to maintain a low ρ_t [40]. In the InGaP and InGaAs system dislocation glide is halted by regions that display high diffraction contrast in TEM [21, 24, 41, 42]. In this work, this diffraction contrast is correlated to composition variations.

Though treated independently here, dislocation pinning is often a precursor to dislocation nucleation. When threading dislocations are blocked, strain relieving misfit dislocations that trail the gliding threading dislocations do not extend along the interface between the lattice-mismatched film and the substrate. Blocked dislocations prevent further relaxation of the lattice-mismatched films. As a result of dislocations being blocked, as the film thickness increases the film will need to nucleate dislocations to relax. Since nucleation of new dislocations occurs at the surface, rampant nucleation greatly increases ρ_t [see Figure 6.1(b)]. Figures 6.1(a) and (b) illustrate schematically the effect of dislocation blocking on the threading dislocation density. In both Figures 6.1(a) and (b) the length of misfit dislocations at the interfaces in the graded buffer is the same indicating the films are equally relaxed; however, in order to achieve the same length of misfit dislocations in Figure 6.1(b), more dislocations were needed to be nucleated thus leading to higher ρ_t.

The graded buffer then has two primary purposes: (1) to maintain a controlled and small constant stress to prevent uncontrolled and rampant dislocation nucleation and (2) to keep existing dislocations moving to relieve the lattice-mismatch. Using existing dislocations to relieve lattice-mismatch ensures relaxation without needing to nucleate many dislocations thus maintaining a low ρ_t. A secondary purpose of graded buffers is that they keep dislocations separated in space to minimize dislocation-dislocation pinning and thus work-hardening. In theory, by using a graded buffer any lattice-mismatch may be slowly accommodated by a similar crystal structure.

In practice dislocations can be pinned in the graded buffers preventing high-quality integration of materials. The primary cause of dislocation pinning in the materials reported in this paper is composition variations caused by phase separation. The composition variations are not the subtle composition undulations that can vary over the cm or mm length scale due to reactor inhomogeneities. Instead, the composition variations observed in this paper are localized and occur semi periodically on the order of 5 μm or even tens of nm. These variations can also have large gradients in composition.

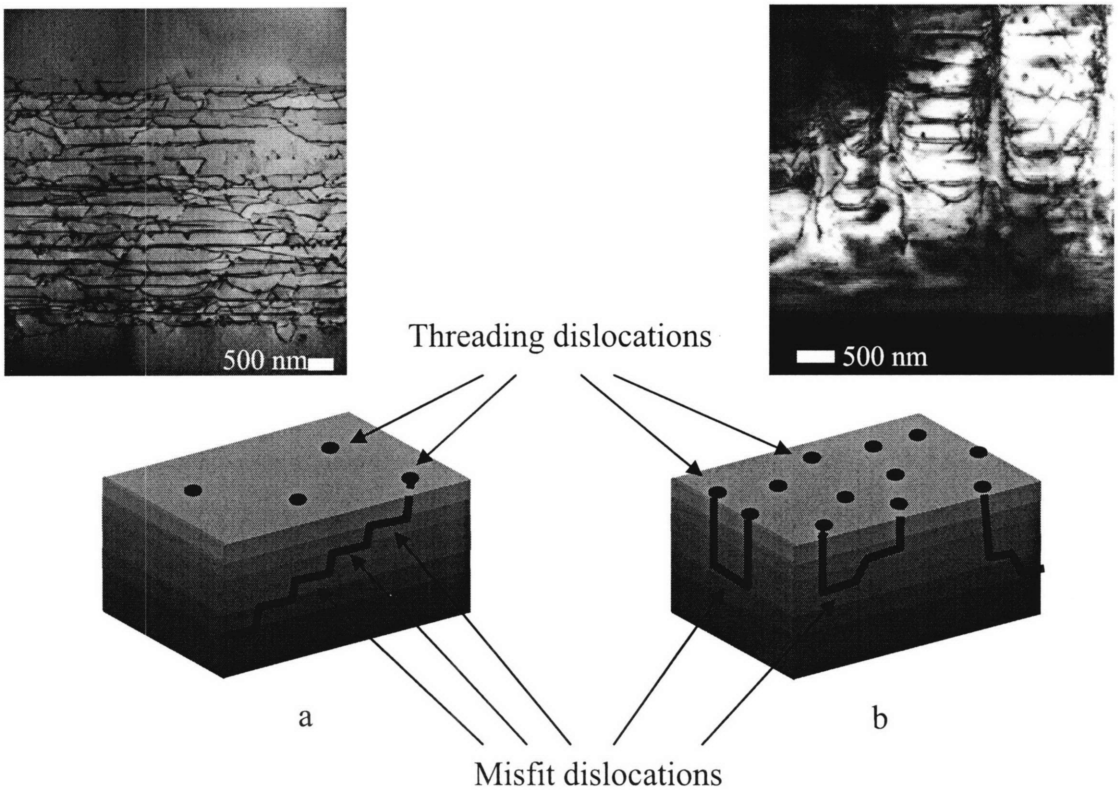

Figure 6.1: Schematic diagram of a graded buffer with a low ρ_t (a) and with a high ρ_t (b) along with XTEM micrographs of what the schematic represents. A low ρ_t graded buffer allows a dislocation to glide over many interfaces extending the misfit dislocation without increasing ρ_t. A graded buffer with a high ρ_t will have many short misfits and each misfit has two threading dislocations and therefore the material will have a large ρ_t. The situation in Figure 6.1 (b) is typically caused by threading dislocations being blocked. The XTEM micrograph in (a) is an InGaAs buffer grown at 725 °C while the one in (b) is an InGaP buffer grown at 600 °C.

6.2. Phase Diagrams

As mentioned earlier, composition variations, induced by phase separation, pin dislocations and greatly increases ρ_t. In fact, if the composition variation is large enough, it can nucleate dislocations when the lattice-mismatch between it and the surrounding matrix is large enough. Since phase separation pins dislocations, understanding phase separation and how to avoid it is crucial to achieving low ρ_t materials.

The phase diagrams for III-V semiconductor surfaces under CVD (Chemical Vapor Deposition) growth conditions are not fully understood. For the growth temperatures and compositions used in this study, phase separation was not expected in the InAs-GaAs or the InP-GaP bulk phase diagrams according to the thermodynamic bulk phase diagrams, see Figure 6.2[20]. (In this study the temperature and composition closest to the conditions for phase separation predicted in the miscibility gap in Figure 6.2 was $In_{0.82}Ga_{0.18}P$ grown at 600 °C which should be about 170 °C above the miscibility gap.)

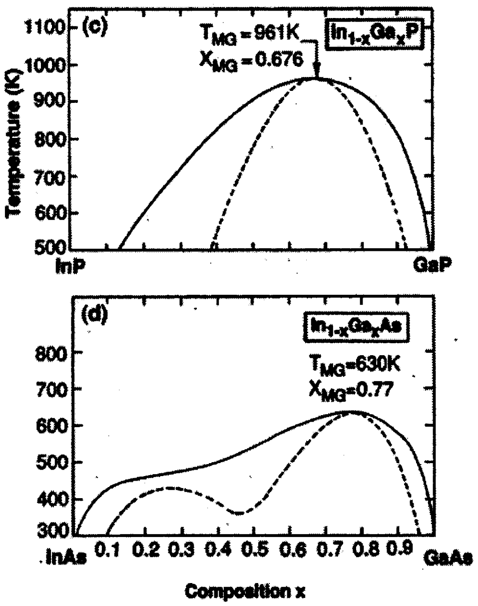

Figure 6.2. Calculated phase diagrams for InP-GaP and InAs-GaAs[20]. In all of the figures T_{MG} and X_{MG} indicate the temperature and composition of the highest point in the miscibility gap.

The phase diagrams in Figure 6.2 were calculated for bulk alloys without considering coherency strain effects which should give an upper bound to the misciblity gap. This work reports composition variations due to phase separation at growth temperatures above this calculated phase separation at the surface during growth via surface diffusion. Free surfaces allow phase separation to occur even when it is unfavorable in the bulk. For example, Kubo *et al.* have observed spinodal decomposition in (001) thin brass foils above the expected decomposition temperature[57, 58]. They surmise that elastic strain energy that represses spinodal decomposition in the bulk is no longer present in thin foils. Because phase separation was observed in the semiconductor alloys studied in this work coupled with the fact that the phase diagrams in Figure 6.2 does not include any coherency terms (which should give an upper bound on phase separation) may suggest there is some condition during CVD growth that is not captured in the calculation of the phase diagram.

In this paper particular growth conditions of InGaAs, InGaP and InAl(Ga)As resulted in Ga enriched regions. These Ga enriched regions were found to block dislocations in the graded buffer preventing the formation of high-quality relaxed semiconductor material. Framing the formation of Ga-enriched regions as a sign of phase separation, we hypothesized that growth at higher temperatures and compositions close to the binary compounds would avoid phase separation. Using this methodology prevented the formation of the Ga-enriched regions and enabled previously unattainable low threading dislocation density, $1.2\text{x}10^6/\text{cm}^2$, InP on GaAs by growth of graded buffers. PL (Photoluminescence) structures were grown on this graded material and on bulk InP. The integrated intensity of the PL structure on this graded buffer was comparable at room temperature and at 20K to the one on bulk InP, attesting to the achievement of low threading dislocation density InP on GaAs. Using kinetics as well as thermodynamics considerations, we address the regimes where phase separation can be avoided (at both low and high temperatures) and attempt to explain results in literature based on this model. Even though phase separation can be avoided at low temperatures, we conclude, since dislocation glide velocity is exponentially dependant on temperature, that only high-temperature growths can yield low dislocation density materials.

6.3. Experimental Procedures

Before growth, GaAs substrates were cleaned in two solutions. First a 10:1 H_2O:HCl solution for 1 min to achieve a hydrophobic surface. The substrate was rinsed with deionized water and then placed in a 20:1:1 H_2SO_4:H_2O:H_2O_2 for 15 s to mildly etch the surface. Finally, after rinsing again, the substrate was again placed in the first solution for one minute, rinsed, and then dried with N_2.

Semiconductor films were grown on this GaAs using an atmospheric pressure Thomas Swan, 2" horizontal MOCVD (Metal Organic Chemical Vapor Deposition) system. The precursors used in this study were tri-methyl In (TMIn), tri-methyl Ga (TMGa), tri-methyl Al (TMAl), AsH_3 and PH_3. The growth temperatures used in this study were from 600-750 °C; but for most films was 725 °C. The substrates were placed on the upstream side of the approximately 7" long susceptor not in a rotating pocket in the center of the susceptor designed to hold the wafer. The placement of the wafer on the upstream side was critical because at the high growth temperatures used in this study most of the In is deposited at the front of the susceptor, consequently, little TMIn gets to the center of the susceptor and makes growth of high In-content films grown at the center impossible.

After placing the GaAs substrate on the upstream side, they were heated to a temperature of 700 °C under an AsH_3 overpressure to remove any native oxide. Before growth of lattice-mismatched films, a fresh GaAs film was grown. The lowest V/III ratio used in growing these materials was 71.

The films were characterized *ex situ* using TEM, x-ray diffraction, atomic force microscopy (AFM) and scanning transmission electron microscopy (STEM). TEM was performed at 200 keV on JEOL 200, 2000 and 2010 microscopes. The TEM samples were prepared by mechanical polishing to a thickness of about 10 μm and thinned to electron transparency using a Gatan Dual Ion Mill or a Gatan Precision Ion Polishing System (PIPS). All XTEM samples were cleaved along <110> directions. The XTEM samples were prepared using the PIPS with a 5° incident Ar ion beam at 5 keV and 5 mA. The PVTEM (Plan View Transmission Electron Microscopy) samples were prepared using the Gatan Dual Ion Miller at 11°, 0.5-1 mA and 6 keV. Most InP containing sample were milled the same as above except with 3 keV to reduce milling damage. The threading dislocation density, ρ_t, was determined in these materials using PVTEM. For the good quality material ($\rho_t \leq 2\text{x}10^6/\text{cm}^2$), ρ_t was determined after viewing >1000 μm^2 of area in a g=<220>-type diffraction condition. The composition and strain of the films were determined using the (004) and (224) peaks in a Bede triple axis x-ray diffractometer using a Rigaku RU200 generator operated at 60 kV and 200 mA. STEM composition analysis was performed using a VGHB603 operated at 250kV and using an Oxford Windowless X-Ray detector. For surface analysis the Nanoscope III AFM operated in tapping mode using a Si cantilever was used. PL was done using an Ar ion laser with main emission lines around 488 nm and a power of about 80mW. The photo-induced emission passed through an Acton SpectroPro 275 monochromator with about 1 nm spectral resolution before it reached a Ge detector.

6.4. Alloys for Achieving Relaxed InP on GaAs

As evidenced by the energy gap vs. lattice constant diagram (Figure 6.3), there are many materials paths one can choose to slowly increase the lattice constant toward InP starting from GaAs in the InGaAsP and InAlGaAs materials systems. These paths provide a number of different routes to achieve high-quality InP on GaAs. Naturally, the more options, the more work that must be done to perform an exhaustive study. However, because composition variations in some materials systems pin dislocations, the ability to use different materials systems to take different paths to avoid these composition variations is key in trying to achieve high-quality ($\rho_t \leq 2\text{x}10^6/\text{cm}^2$) InP on GaAs (lattice-mismatch of 3.7%). In this study a number of materials paths have been taken including graded buffers using the InGaAs, InGaP, InAlAs, InGaAlAs materials systems as well as a InGaAs to InGaP hybrid path. The focus of this work is on the InGaAs and InGaP materials systems with a short discussion on effects of the addition of Al. As we show, a general theme to avoid phase separation is to grow at higher temperatures and adjust compositions to avoid phase separation.

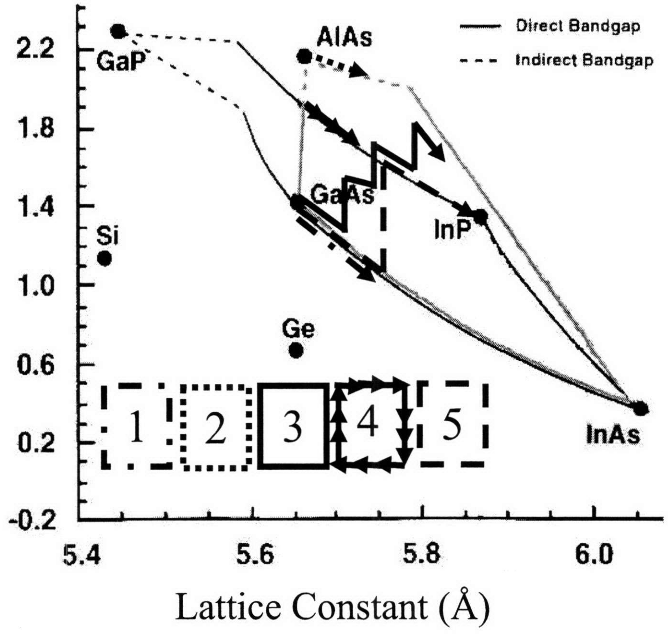

Figure 6.3: Energy gap (E_g) vs. Lattice constant diagram for the InGaAsP and InAlGaAs materials systems. The Si and Ge are included as reference and to draw attention to the fact that GaAs is nearly lattice matched to Ge for future integration on Si. The arrows and numbers indicate different ternary and quaternary materials paths that were explored in increasing the lattice constant towards InP in different samples. The numbers correspond to the "Path Taken" field in Table 1.

Sample	T_g (°C)	Path Taken	Grading Rate (%f/μm)	Growth Rate (Å/s)	V/III (minimum)	ρ_t (cm^{-2})	Phase Separation Composition
650$In_{0.36}Ga_{0.64}As$	625	1	0.50	7.5-11.9	94	9.8x10^6	$In_{0.26}Ga_{0.74}As$
725$In_{0.34}Ga_{0.66}As$	725	1	0.44	6.7-11.3	92	9x10^5	$In_{0.32}Ga_{0.68}As$
725$In_{0.42}Ga_{0.58}As$	725	1	0.45	6.8-12.6	87	>3.1x10^7	$In_{0.32}Ga_{0.68}As$
750$In_{0.3}Al_{0.7}As$	750	2	0.43	6.7-10.6	126	3.5x10^8	?
750$In_{0.43}Al_xGa_{(0.57-x)}As$	750	3	0.43	6.7-13.1	82	1.3x10^6	?
625$In_{0.82}Ga_{0.18}P$	625	4	0.26	5.9-8.7	71	2.3x10^9	$In_{0.68}Ga_{0.32}P$
725$In_{0.25}Ga_{0.75}As$/600$In_{0.73}Ga_{0.27}P$	725 & 600	5	0.35	5.3-10.1	133	3.4x10^8	$In_{0.94}Ga_{0.06}P$
725$In_{0.32}Ga_{0.68}As$/625$In_{0.8}Ga_{0.2}P$	725 & 625	5	0.39	5.3-10.1	133	1.4x10^8	$In_{0.9}Ga_{0.1}P$
725$In_{0.3}Ga_{0.7}As$/700$In_{0.77}Ga_{0.23}P$	725 & 725	5	0.32	5.8-9.4	79	1.2x10^6	n/a

Table 1: Growth details and summary of results for most samples discussed in this paper. The table includes seven headings of which from left to right are: the growth temperature, the path taken (see Figure 6.3), the grading rate in %misfit/μm, the minimum V/III ratio, the threading dislocation density, and at what, if any, composition phase separation occurred. The "Path Taken" field indicates which ternary material system a sample utilized to increase the lattice constant towards InP.

When looking at the E_g (Band gap) vs. Lattice Constant diagram in Figure 6.3, there are three paths using different ternary materials systems to get from the GaAs lattice constant to that of InP, namely InGaAs, InGaP and InAlAs. Though many MBE (Molecular Beam Epitaxy) studies prefer the InAlAs materials system[59-61], this study began with the InGaAs materials system because the addition of In to GaAs is an ideal system for study, has enabled the first HEMT (High-Electron Mobility Transistor) devices[62], and has led to promising graded buffer results by Bulsara *et al.* [41, 42]. (The InGaAs materials system is path 1 in Figure 6.3.)

6.4.1 InGaAs Graded Buffers

We first discuss the 650 °C growth temperature results for relaxed InGaAs alloys on GaAs. (The details of growth including growth temperature, T_g, grading rate, and V/III ratio are in Table 1.) AFM, and bright-field (BF) XTEM and PVTEM micrographs of sample 650$In_{0.36}Ga_{0.64}As$ are shown in Figure 6.4. (In this paper, the naming convention of each sample lists the growth temperature and composition.) Diffraction contrast regions are visible in XTEM and PVTEM and are notated as PS for phase separation. (We later show that these regions yield diffraction contrast because they are Ga-enriched.)

Due to the known growth rates and final composition, the approximate composition where PS (Phase Separation) started in XTEM could be inferred. We determined the composition at which phase separation started by identifying the location in the graded buffer XTEM micrograph where diffraction contrast first appeared. Since the graded composition profile is known, the composition of In can be determined from the location in XTEM. For sample 650$In_{0.36}Ga_{0.64}As$ Ga-enriched, phase separated regions started to form around $In_{0.26}Ga_{0.74}As$.

Interestingly, the phase separated regions in the PVTEM micrograph Figure 6.4(c) sometimes follow a <100> direction. As a result, the XTEM sample sectioned and prepared along a <110> direction intersects these planar defects at ~45°. Consequently, upon close inspection moiré fringes result from the change in lattice constant between the planar defect and the matrix in Figure 6.4(b). The moiré fringes have a longer wavelength near the substrate than close to the growth surface. The contrast in Figure 6.4(c) is somewhat reminiscent of APBs (Anti-Phase Boundary). However, the planar regions causing the strain contrast from phase separation in these samples do not enclose areas in PVTEM like planar APBs. The features present in these samples are regions of strain contrast that meander off exact <100> directions and terminate without enclosing regions as seen in Figure 6.4(c).

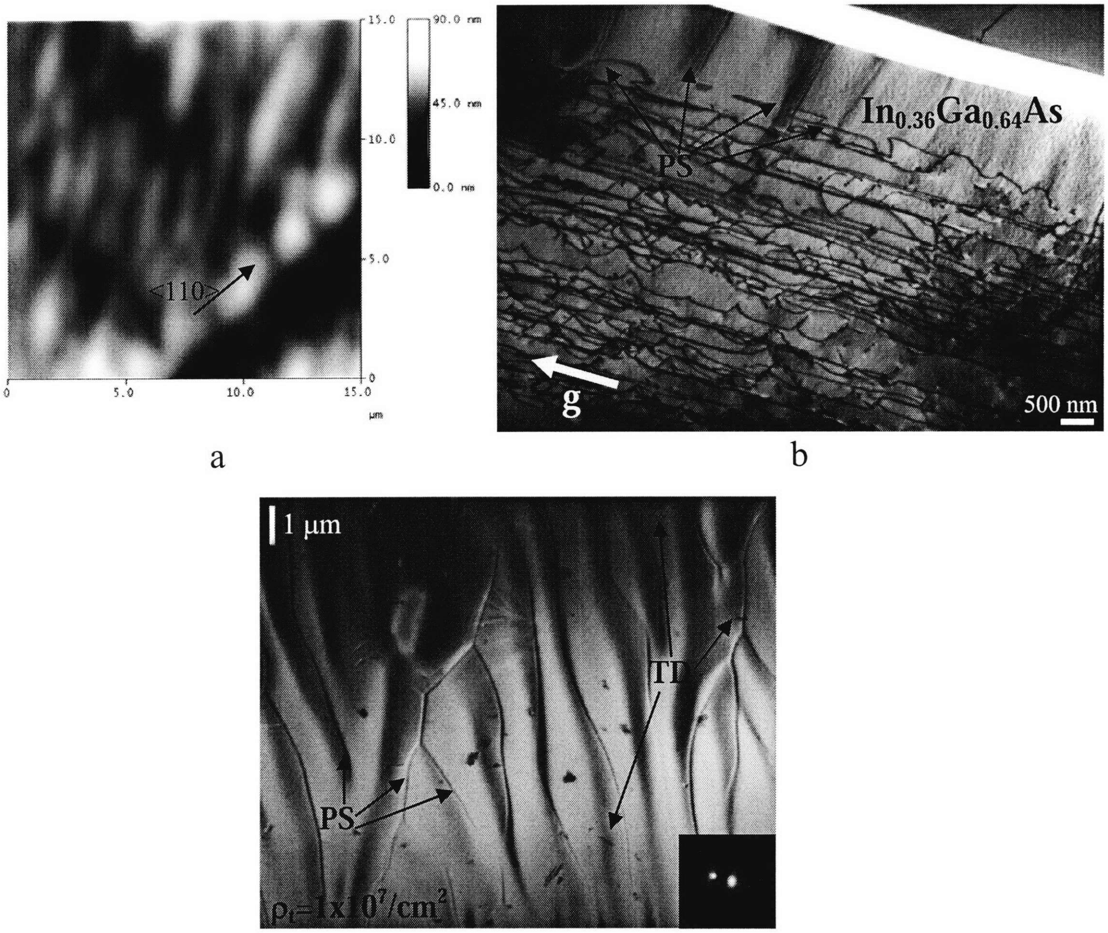

a

b

c

Figure 6.4: Sample 650$In_{0.36}Ga_{0.64}As$ (The naming convention lists the growth temperature and final composition.) in (a) AFM, and (b) bright-field, g=<220>, XTEM, and (c) bright-field, g=<220> PVTEM micrographs. In the XTEM picture, the In-depletion begins around 26% In. The periodicity of the wavy-like defects is about 1 μm determined by the PVTEM micrograph. Phase separation (PS) and threading dislocations (TD) are identified in the TEM micrographs.

The composition variations in sample 650$In_{0.36}Ga_{0.64}As$ produced high strain regions as evidenced in the TEM micrographs in Figure 6.4. These strained regions blocked dislocation glide and led to high threading dislocation densities. Using empirical knowledge that higher temperatures should promote disorder and remove phase separation, the InGaAs graded buffer growth temperature was increased to 725 °C and indeed we were able to achieve high-quality ($\rho_t=9\text{x}10^5/\text{cm}^2$) relaxed InGaAs out to a lattice constant of 5.792Å. This lattice constant corresponds to a mismatch of 2.4% and a composition of $In_{0.34}Ga_{0.66}As$. This sample, sample 725$In_{0.34}Ga_{0.66}As$, is shown in Figure 6.5 consisting of a bright-field XTEM and PVTEM micrographs of this high-quality material. The growth of this high-quality material was enabled by the suppression of phase separation evidenced by the lack of diffraction contrast in TEM.

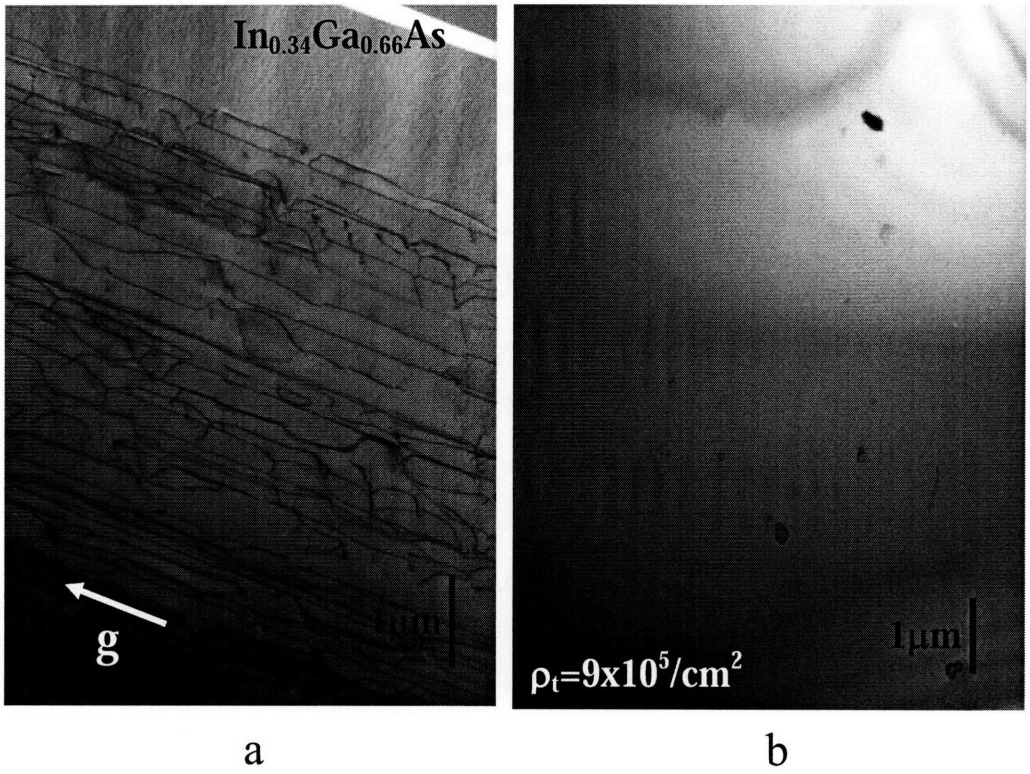

Figure 6.5. Sample 725$In_{0.34}Ga_{0.66}As$ in bright-field g=<220> XTEM (a) and PVTEM (b) micrographs of high-quality $In_{0.34}Ga_{0.66}As$ on GaAs grown at 725 °C with a threading dislocation denisity of $\rho_t=9x10^5/cm^2$.

After increasing the growth temperature, T_g, from 625 to 725 °C, we achieved high-quality $In_{0.34}Ga_{0.66}As$ only to observe that increasing the In content beyond $In_{0.34}Ga_{0.66}As$ again leads to Ga-enriched regions that pin dislocations causing the dislocation density to increase (Figure 6.6). Sample 725$In_{0.42}Ga_{0.58}As$ depicted in Figure 6.6 with a final relaxed composition of $In_{0.42}Ga_{0.58}As$ In has a much larger $\rho_t >$

$3.1 \times 10^7/cm^2$, over 30 times larger then sample $725In_{0.34}Ga_{0.66}As$. The actual threading dislocation density is likely to be much greater, as it is difficult to count all of the threading dislocations in the dislocation pile-up regions.

This phase separation causes an increase in ρ_t because dislocation glide is arrested. Some dislocations appear to be blocked [circled in Figure 6.6(c)] while others might have been generated by the strongly contrasting regions [see the circled region in Figure 6.6(b)]. The pinning and possible generation of dislocations at these defects accounts for the increase in ρ_t compared to sample $725In_{0.34}Ga_{0.66}As$. The microstructure of the phase separation observed in XTEM in sample $725In_{0.42}Ga_{0.58}As$ appears different than that of sample $650In_{0.36}Ga_{0.64}As$ depicted in Figure 6.4(b). Upon close inspection, moiré fringes are visible in Figure 6.4(b) but not in Figure 6.6(b). The origin of this difference will be discussed later.

In sample $725In_{0.42}Ga_{0.58}As$ the onset of Ga-enrichment starts to appear around 32% In determined by the depth at which the diffraction contrast appeared in XTEM. Interestingly, with an increase in T_g from 650 °C to 725 °C the composition where phase separation is first seen increased from $In_{0.26}Ga_{0.74}As$ to about $In_{0.32}Ga_{0.68}As$. This result is consistent with what one would expect in phase separated materials as a given alloy is more miscible at higher temperatures (see also Figure 6.2 and Kim *et al.*[21]).

In analyzing Figure 6.6 a strong correlation between the phase separation and trenches becomes evident and leads to implications as to the mechanisms of phase separation formation. Figure 6.6(a) shows an AFM micrograph of sample $725In_{0.42}Ga_{0.58}As$. The AFM image depicts trenches with a periodicity of ~5 μm. A similar periodicity is evident in the PVTEM image [Figure 6.6(c)] between the dark diffraction contrast regions. The dark contrast regions in the XTEM micrograph in

Figure 6.6(b) are also about 5 μm apart. Each contrast region in XTEM is associated with a trench leading to a strong correlation between the AFM surface trenches and the strongly diffracting regions in both bright-field TEM images. Wang *et al.* has also correlated AFM surface roughness with phase separation[63].

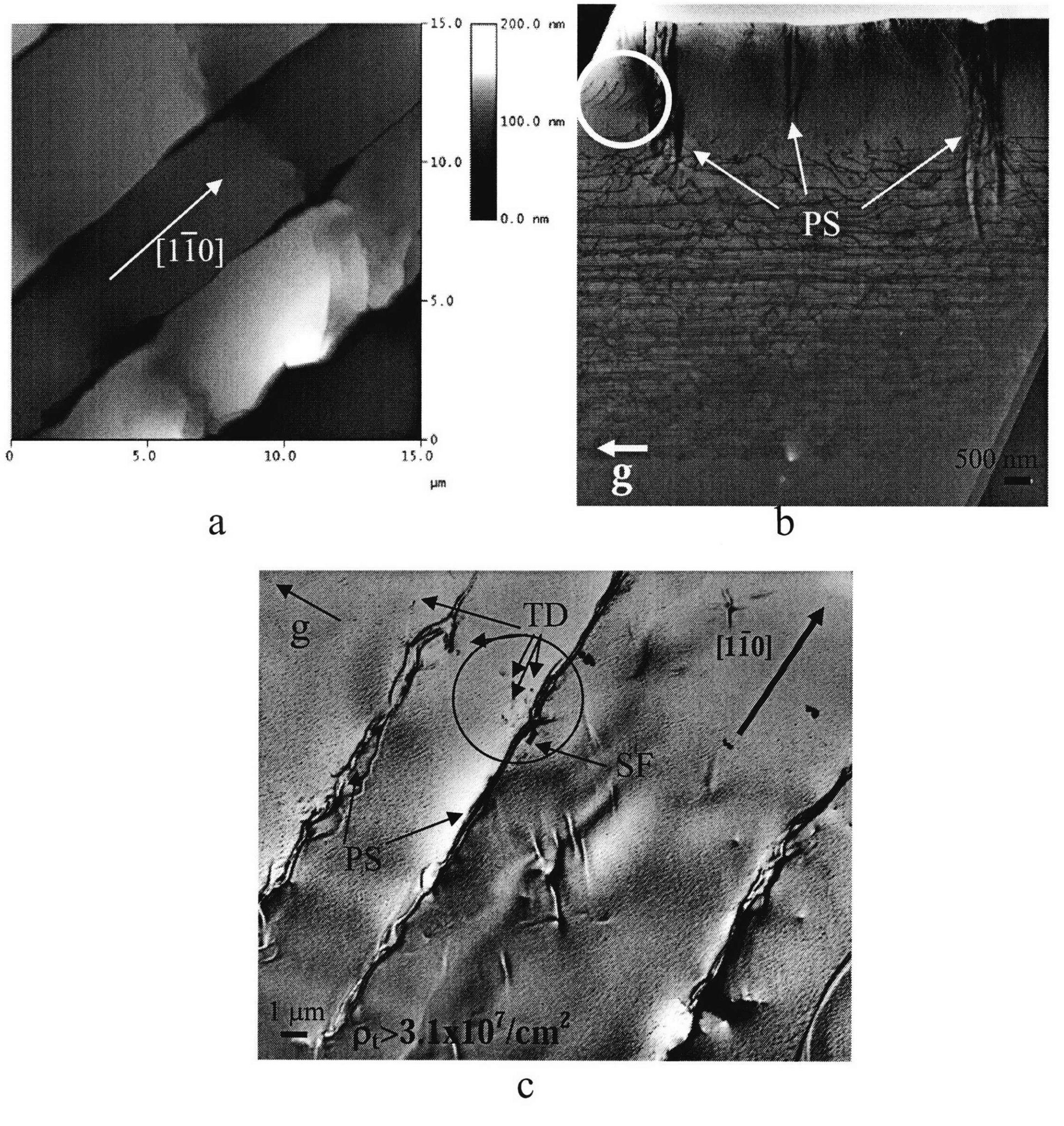

Figure 6.6. (a) AFM, (b) BF, g=<220>, XTEM, and (c) BF, g=<220>, PVTEM micrographs of sample 725$In_{0.42}Ga_{0.58}As$. In micrograph (a), the periodicity between the trenches in AFM correlated well with the periodicity of the strong contrast lines along the <110> in (c) with a wavelength of about 5 μm. In the XTEM micrograph (b) the strong contrast defects are associated with a trench in the surface and that the deeper the trench the earlier the defect was formed. Finally, the strong contrast regions pin threading dislocations (TD) and cause a stacking fault (SF) circled in (c).

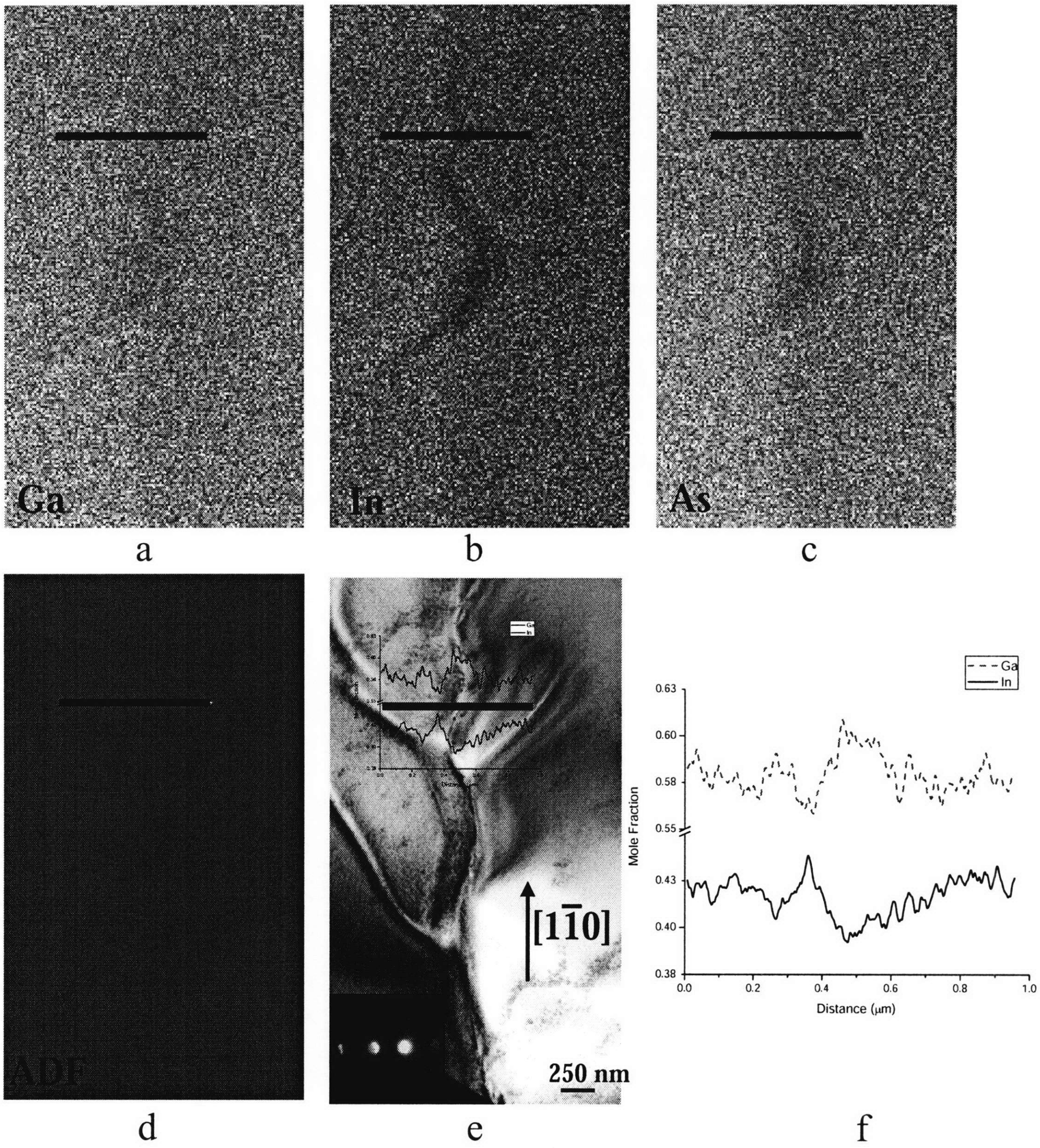

Figure 6.7. STEM results from sample 725$In_{0.42}Ga_{0.58}As$ in plan view. Figures (a), (b), and (c) are compositional maps of Ga, In and As respectively taken in a STEM using EDS. (d) is an annular dark field image of the same region taken just before collecting the compositional maps in (a), (b), and (c). (e) is a bright-field TEM micrograph (g=<220>) of the same area as depicted in (a)-(d). A compositional line scan taken along the black line denoted in (a)-(e) is shown in (f) and a small version of this is placed on top of (e) to show the correlation between the Ga enrichment, the In depletion and the strong contrast exhibited in the TEM micrograph. Note that both the As map and ADF image indicate that the material is thinner in the vicinity of the Ga-rich region. Finally, close inspection reveal that there are dislocations pinned along the Ga-rich defect in (e).

To correlate Ga-enriched regions to TEM diffraction contrast EDS (Energy Dispersive Spectroscopy) in a STEM was performed on sample 725$In_{0.42}Ga_{0.58}As$. Figure 6.7 shows the compositional maps, an ADF (Annular Dark Field) image, and <220>, bright-field image of the same area. In the STEM element maps, the whiter regions correspond to areas of greater elemental signal. All STEM maps in this work were collected in weakly diffracting conditions and in this case is evidenced by the ADF image in Figure 6.7(d) to prevent erroneous results due to ALCHEMI (Atomic Location by Channeling-Enhanced Microanalysis).

Interpretation of EDS composition line scans and maps is not completely straightforward because the signal depends not only on the composition of the films but also on the thickness and diffraction condition of the sample as well. Consequently, in a weekly diffraction condition the As signal should be proportional only to the volume of the sample. Therefore, the reduction in As intensity in the region of the different contrast implies that there is a trench associated with that diffraction contrast region. This result gives further evidence there is a trench associated with the phase separation. Notice that in Figure 6.7(a) there is not a significant change in the Ga composition across the defect in spite of the fact that there is less material in the trench. With this in mind, in order to determine the actual composition of the material, throughout this paper In and Ga EDS x-ray counts were normalized by the group V EDS counts (be it As or P) in order account for thickness variations. Once this ratio was obtained for the In and Ga counts, these ratios were scaled to match the composition of the matrix, as determined using (004) and (224) reflections in triple-axis X-ray diffraction. The region where the line scan in Figure 6.7(f) was taken is indicated by a line in Figures 6.7(a)-(e). Figure 6.7(f) shows the percentages of the In and Ga content and is superimposed onto the Figure 6.7(e) to compare the diffraction contrast with the composition variation. Despite the noise that is evident in Figure 6.7(f), overarching increases in Ga content correlate with decreases in In and vice versa.

Others have performed EDS on phase separated regions in semiconductors and have found similarly that, for example in GaInAsSb, the smaller lattice constant material, in this case GaAs rich, appears to thread through a matrix of larger lattice constant material, rich in InSb[64]. Others have seen composition variations corresponding to strain contrast regions in TEM in GaAs/InAs short period superlattices (SPS) and the InGaAsP materials system as well[65-68].

Phase separation is not only affected by temperature and composition. Wafer orientation also affects the formation of phase separation as well[57, 58, 69]. The two plan view images in Figure 6.8 are from samples grown together side-by-side in the reactor to a final composition of $In_{0.32}Ga_{0.68}As$ and a temperature of 725 °C. The sample shown in Figure 6.8(a) was grown on a nominally (001) GaAs wafer while Figure 6.8(b) is from a sample which was grown on a substrate off-cut 2° towards the (101) pole. Phase separation is clearly visible along the $[1\bar{1}0]$ direction in Figure 6.8(b). (Phase separation appears to prefer the $[1\bar{1}0]$ over the [110].) Interestingly, this morphology along $[1\bar{1}0]$ is formed by smaller lines along the $[0\bar{1}0]$ and is somewhat different to the morphology in Figure 6.6 where the phase separation regions along $[0\bar{1}0]$ are not as obvious. Kubo *et al.* also observed a strong dependence on the morphology of phase transformed regions on orientation noticing phase transformation on {001} foil but not on {110} or {111}surfaces in brass foils[57, 58]. It is clear from these results that the phase separation mechanism depends strongly on the wafer miscut when in the region of potential immiscibility. The ability for In to cluster into regions on the surface, thereby creating Ga-rich regions, is encouraged by wafer miscut for our growth conditions. Figure 6.8(b) also shows threading dislocations (marked TD) pinned against the strain contrast caused by the composition variations. In both figures surface step bunching is present, though the off-cut sample seems to have stronger surface step bunching then the on-axis sample.

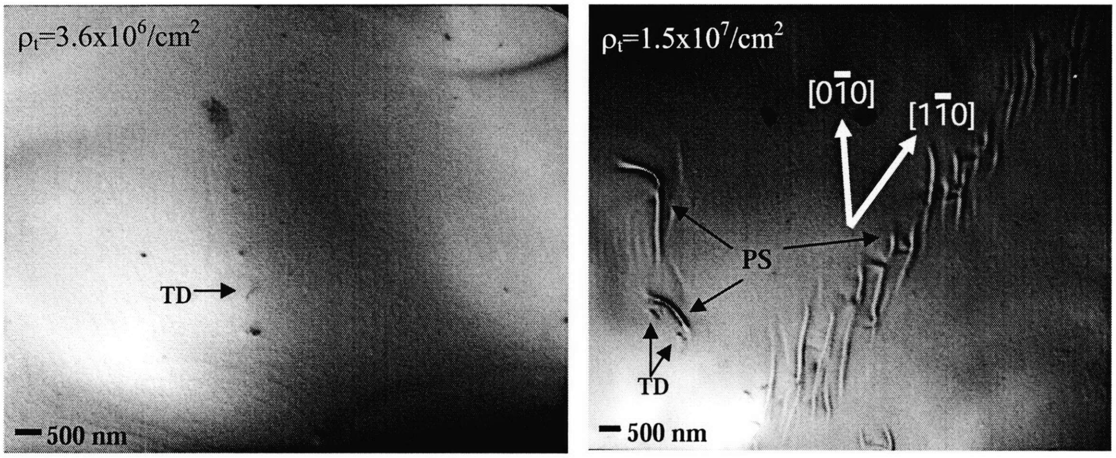

a

b

Figure 6.8. Plan view TEM micrographs of two samples grown side-by-side during the same growth to a final composition of $In_{0.32}Ga_{0.68}As$ at 725 °C. The sample depicted in micrograph (a) was grown on an on-axis GaAs substrate while that shown in (b) was grown on a GaAs substrate that was cut 2° towards the (101) pole. Notice the In-depleted regions imparting strong contrast to (b) and how these region pin dislocations in the lower left-hand corner.

To see the evolution of the microstructure for 2° offcut substrates, a sample with a graded buffer to a final composition of $In_{0.35}Ga_{0.65}As$ was growth at 725 °C, shown in Figure 6.9. This sample is similar to that depicted in Figure 6.8(b) except for the final composition of the graded buffer. By comparing Figure 6.8(b) to Figure 6.9(c), one can see that the phase separated regions cover more of the surface in Figure 6.9(c) but still follow the $[1\bar{1}0]$ direction.

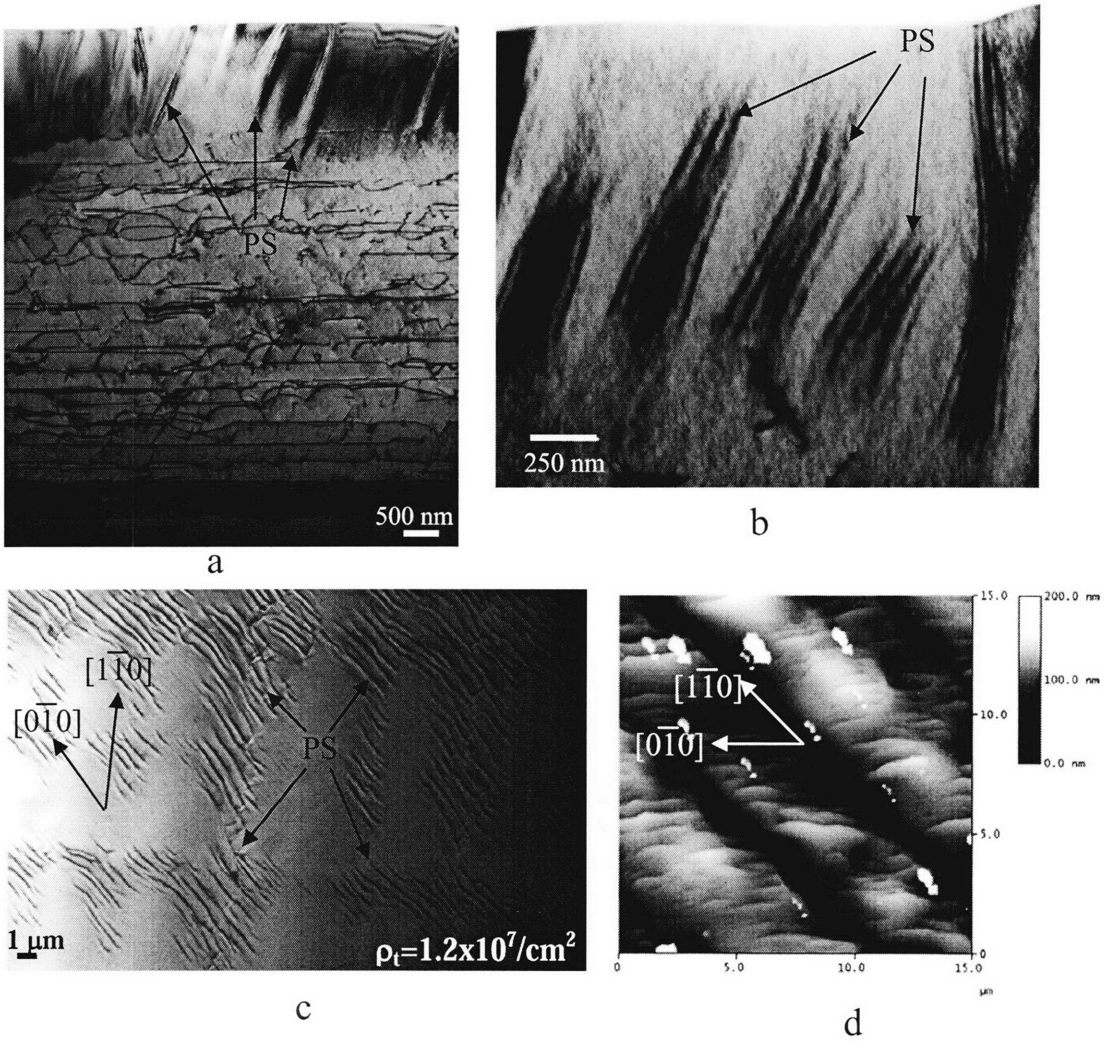

Figure 6.9: InGaAs graded buffer to a final composition of $In_{0.35}Ga_{0.65}As$ grown at 725 °C on a 2° offcut wafer towards the (101) pole. Figures (a)-(c) are BF, g=<220>, TEM micrographs. Figure (a) is a XTEM micrograph while Figure (b) is a magnified picture of the moiré fringes in the cap. Notice that the moiré fringes have a longer wavelength towards the bottom of the figure then the wavelength towards the top. Figure (c) is a large area PVTEM micrograph. The periodicity of the vertical lines are about 4-5 µm similar to the distance between the diagonal trenches shown in (d).

The microstructures observed in the above figures are caused by composition variations due to phase separation and an understanding of the orientation of phase separation and XTEM foils can explain why the microstructures appear differently in the InGaAs materials system as depicted in Figures 6.4(b), 6.6(b), and 6.9(a) and (b). The phase separation observed in these samples forms platelets and analysis of PVTEM and XTEM micrographs is required to understand the differences in the microstructure observed in TEM. As seen in PVTEM, phase separation can trace lines predominantly along $\left[1\bar{1}0\right]$ (as in Figure 6.6) or predominantly along the $\left[0\bar{1}0\right]$ (as in Figure 6.4, Figure 6.8(b), and Figure 6.9) but organized along $\left[1\bar{1}0\right]$. Related to the morphology in PVTEM, sometimes in XTEM phase separation manifests itself as vertical columns (as in Figure 6.6) other times the phase separation appears as black and white periodic fringes (as in Figure 6.4 and Figure 6.9). There is a correlation between how the phase separation is oriented in PVTEM and how it appears in XTEM.

In plan view when phase separated regions form planes along <110>-type directions as in Figure 6.6, the diffraction contrast appears as vertical columns in XTEM. On the other hand, when phase separation forms planes along a <100> direction in plan view, in XTEM the phase separation appears as periodic black and white moiré fringes. The moiré fringes appear in XTEM because the XTEM samples were sectioned along a <110> direction and, as a result, the phase separated planes cut through the XTEM foils at a ~45° angle and so the electron beam has a component normal to the platelet/matrix interface leading to moiré fringes (see reference [49] for more details on moiré fringes).

Moiré fringe confirmation was verified by performing tilt experiments illustrated by Fultz and Howe (see pages 389-392 in [49]). Knowing that these are moiré fringes, the contrast can be used to determine the lattice constant difference between the phase separated region and the matrix. For a moiré boundary, we can use the following relation to calculate the moiré fringe spacing difference given the lattice constant of the phase separated region and matrix:

$$D = \frac{d_1 d_2}{d_1 - d_2} \qquad \textbf{Equation 17}$$

where D is the distance between moiré fringes, d_1 and d_2 are the lattice plane distances. Using the moiré fringe spacing in Figure 6.9(b) we calculated there is a ~4% Ga enrichment compared to the matrix at the bottom of the boundary while more towards the surface there was ~6% enrichment this difference in Ga enrichment is evidenced by the variations in the moiré fringe wavelength. This composition variation is similar to those observed in other STEM analysis discussed later.

Further exploration is required to understand why phase separation traces along the <110> (Figure 6.6) and sometimes a hybrid of the two (Figure 6.8 and Figure 6.9). In most cubic materials phase separation occurs along the <100> direction because it is the softest direction elastically[70]. Therefore <110> orientation of the Ga-enirhced platelets is a surprising result. The <110> alignment of the <010> oriented features is reminiscent of the typical "cross-hatch" patterns that form on relaxed mismatched materials[71]. Just as the underlying strain from misfit dislocations produces the characteristic cross-hatch pattern the underlying strain may also play a role in determining the microstructure of phase separation leading to phase separation tracing out <110> directions usually composed of phase separation along <100> directions.

The origin of the cross-hatch pattern is from the strain fields at the surface produced by the underlying misfit dislocation network that relieves the lattice-mismatch stress between a film and the underlying substrate. These dislocations are finite sources of strain relief spaced unevenly across the interface and, consequently, cause varying strain states at the surface with some regions under tension and others under compression. Since the misfit dislocation array lies along <110> directions, as a result of 60° dislocation glide[7], the strain fields produced and enveloping them also lie along <110> directions. In Figure 6.8(b) and Figure 6.9(c) the <100> phase separation traces <110> directions.

The strain fields associated with misfit dislocation arrays cause the characteristic cross-hatch pattern associated with graded buffers[71-73] where regions under tension grow faster then regions under compression[72]. In addition to causing the cross-hatch pattern, strain is known to affect phase separation formation in materials. For example, in Al-Cu alloys a stress as small as 73.5 MPa can alter the formation of phase separation [74-76] and applied stress can even change the miscibility gap[77]. In metal systems where strain was shown to affect phase separation, the resulting phase separation manifested in a way such that the phase separation reduced the strain [74-76]. Thus, the presence of compressive strain would enhance Ga enrichment increasing T_{MG} thus expanding the miscibility gap in the regions on the surface under compression. Consequently, the trench regions in the cross-hatch pattern under compression lead to the first instances of phase separation. This appears to be the case in comparing the AFM, PVTEM and XTEM in Figure 6.6 where there is a strong correlation between the phase separated regions in PVTEM and the trenches in AFM. This type of correlation is also applicable in Figure 6.9 as well. Because phase separation is affected by strain, phase separation can act as a strain-field map to distinguish regions of compression and tension on the surface, as in Figure 6.9(c). (It should be noted that the smaller Ga atom cannot by itself account for the trench depth observed.)

6.4.2 In(Ga)AlAs Graded Buffers

Since the MOCVD system used in this work was not designed for growth temperatures much beyond 725 °C, increasing the temperature further was not an option to attain high-quality InP on GaAs. Consequently, other materials systems to avoid phase separation were investigated like in the In(Ga)AlAs and the InGaP systems, paths 2-5 in Figure 6.3.

On the path toward high-quality InP on GaAs the InGaAlAs materials system was also explored with limited success, see paths 2 and 3 in Figure 6.3. The addition of Al may effectively repress the miscibility gap and allow for higher In content films without having composition variations strong enough to block dislocation glide in some InGaAlAs materials. Threading dislocation densities did increase in a InAlAs graded buffer with a final composition of $In_{0.3}Al_{0.7}As$ was reached at 750 °C, $\rho_t=3.5x10^7/cm^2$ (see path 2 in Figure 6.3) indicating that Al by itself actually deteriorated the graded buffer quality compared to InGaAs. However, experimentation with the quaternary InGaAlAs showed that by increasing Al along with In, high-quality $In_{0.43}Ga_{0.14}Al_{0.43}As$ with $\rho_t=1.3x10^6/cm^2$ could be achieved (path 3 in Figure 6.3). The PVTEM images of these samples are shown in Figure 6.10. It is not clear at this time why the results for InAlAs and the quaternary are different. Despite the numerous strain contrast features at high density in Figure 6.10(b), a low threading dislocation density was achieved indicating that numerous weak strained regions may be better than few highly strained contrast features in agreement with work by Kim *et al*[21]. Some further work in the InAlGaAs materials system was attempted with no further progress attained.

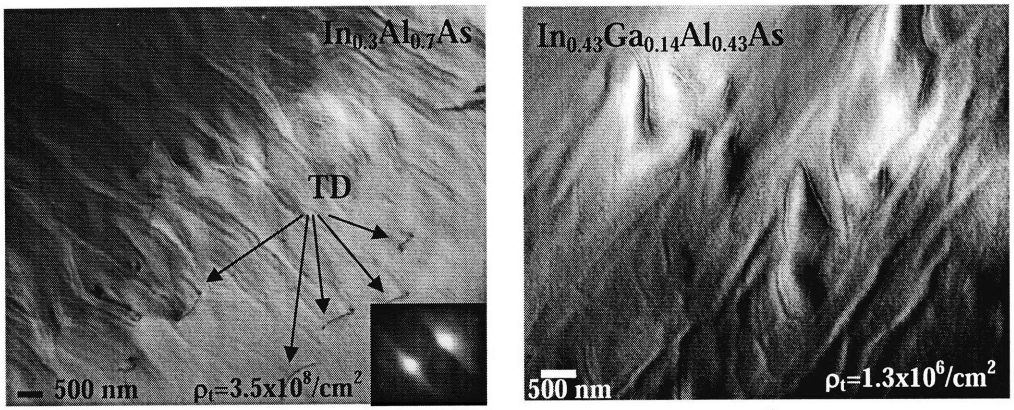

a b

Figure 6.10: PVTEM of graded $In_{0.3}Al_{0.7}As$ (a) and graded $In_{0.43}Ga_{0.14}Al_{0.43}As$ (b) samples. The $In_{0.3}Al_{0.7}As$ sample has a high ρ_t while the $In_{0.43}Ga_{0.14}Al_{0.43}As$ has a low ρ_t. The $In_{0.43}Ga_{0.14}Al_{0.43}As$ is on a graded buffer that increases the In content and the Al content together.

6.4.3 InGaP Graded Buffers

Since the InGaAs and the In(Ga)AlAs materials systems had limited success in achieving high-quality InP on GaAs, the InGaP material system was also explored. To this end, an InGaP graded buffer on GaAs was grown at 625 °C, sample 625$In_{0.82}Ga_{0.18}P$. The structure initially had lattice-matched $In_{0.49}Ga_{0.51}P$ on GaAs, and gradually increased the In composition at a rate 4.3%In/μm to a final composition of $In_{0.82}Ga_{0.18}P$ (the same lattice constant as $In_{0.28}Ga_{0.72}As$). In Figure 6.11(a) that the Ga-enriched regions start to form about half way into the buffer around the composition $In_{0.68}Ga_{0.32}P$ determined using the XTEM micrograph. Note that, in general, phase separation in the InGaP system produces more highly strained contrast features compared to InGaAs.

The observed diffraction contrast is caused by changes in the lattice constant and produces displacement vectors. The displacement vectors caused by the stronger InGaP phase composition variations are perpendicular to the Ga-enriched planes or platelets. The platelets tend to lie along low-index planes with the displacement vector lying parallel with the substrate surface. The diffraction contrast can be made to disappear in TEM when the diffraction vector, **g**, in a two-beam condition lies parallel with the intersection of the Ga-enriched platelet and the growth surface. This occurs because the diffraction contrast disappears when the displacement vector, **r**, which is normal to the Ga-enriched platelet, is perpendicular to the diffraction vector, **g**, according to the equation

$$\vec{g} \cdot \vec{r} = 0 . \qquad \textbf{Equation 18}$$

For this reason, since the Ga-enriched planes lie along both <110> directions in Figure 6.11(c) and one set would disappear for a given **g**=<220> diffraction condition, the **g**=<400> micrograph shows both sets of phase separation regions are in contrast. This figure enables the correlation between the TEM diffraction contrast and the Ga-enrichment in Figure 6.11(d). (Mahajan *et al.* have seen the same contrast disappear when **g** was parallel to the defect in lattice-matched material[78].) Also apparent in Figure 6.11, is that larger TEM contrast is associated with larger composition fluctuations seen especially in Figure 6.11 (a) and (b). The composition variation in sample 625$In_{0.82}Ga_{0.18}P$ caused a great increase in ρ_t to $2.3x10^9/cm^2$.

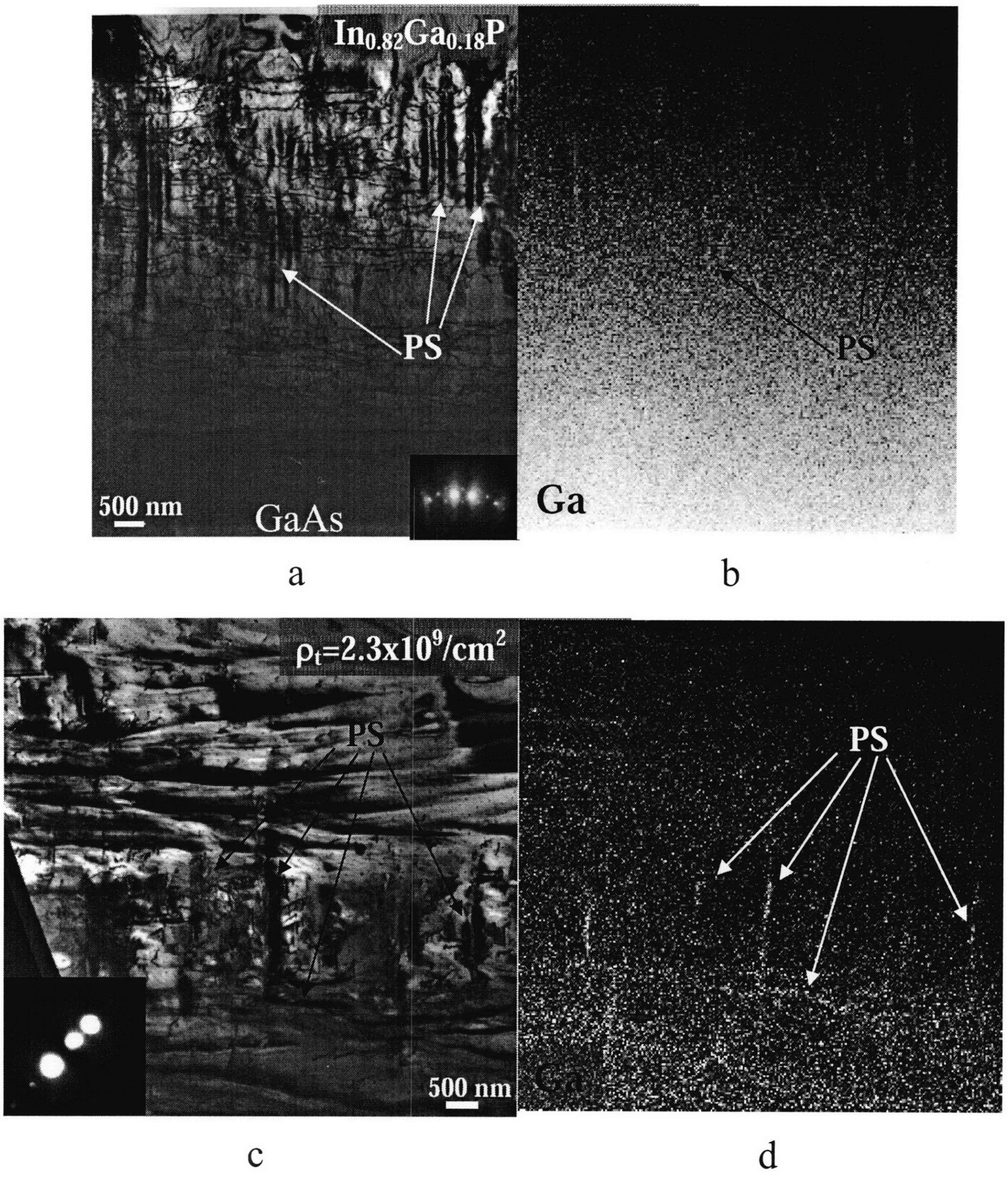

a b

c d

Figure 6.11: TEM and EDS micrographs of sample 625$In_{0.82}Ga_{0.18}P$. Figure 6.11(a) and (b) are XTEM micrograph and Ga XSTEM map respectively while (c) and (d) PVTEM (in the g=<040>) micrograph and Ga PVSTEM map respectively. Figure 6.11(a) and Figure 6.11(b) are taken from the same area just as (c) and (d) are. Notice the onset of the In-depleted defects occurs about half way into the cross section in Figure 6.11(a) around the composition of $In_{0.68}Ga_{0.32}P$.

6.4.4 Hybrid Graded buffers using InGaAs and InGaP

Since strong phase separation was observed in sample 625$In_{0.82}Ga_{0.18}P$ and recalling that compositions near a pure component in a phase diagram are less likely to encounter phase separation, the In-rich side of the InP-GaP phase diagram was explored. The exploration of In-rich InGaP compositions was enabled by using the high-quality $In_{0.34}Ga_{0.66}As$ discussed earlier as a platform on which InGaP graded buffers could be grown. ($In_{0.34}Ga_{0.66}As$ is lattice-matched to $In_{0.81}Ga_{0.19}P$.) By building InGaP alloys on top of this InGaAs platform, very high concentrations of In will exist in all the InGaP graded buffer alloys, in principle minimizing phase separation effects and possibly leading to high-quality materials between the $In_{0.34}Ga_{0.66}As$ and InP lattice constants (path 5 in Figure 6.3). An $In_{0.25}Ga_{0.75}As$ graded buffer grown at 725 °C was used as a platform on top of which lattice-matched $In_{0.73}Ga_{0.27}P$ was grown at 600 °C and graded to InP. Figure 6.12 shows the STEM and TEM results from sample 725$In_{0.25}Ga_{0.75}As$/600$In_{0.73}Ga_{0.27}P$ and depicts Ga-enriched regions.

The STEM results for this sample in Figure 6.12 show a one-to-one correlation between Ga-enrichment and strong diffraction contrast. Figure 6.12(a)-(e) demonstrate that the regions with strong **g**=<220> contrast are poor in In and rich in Ga with no apparent change in the P except with thickness of the XTEM foil which accounts for less signal towards the top of the figure. The white horizontal line notated in Figures 6.12 (a)-(e) is the region where the line scan shown in Figure 6.12(f) was taken. To aid the eye and demonstrate the correlation between composition variation and diffraction contrast, a small line scan is superimposed on Figure 6.12(e). The elemental maps and line scans were taken in a poorly diffracting condition to avoid ALCHEMI evidenced in the ADF image in Figure 6.12(d).

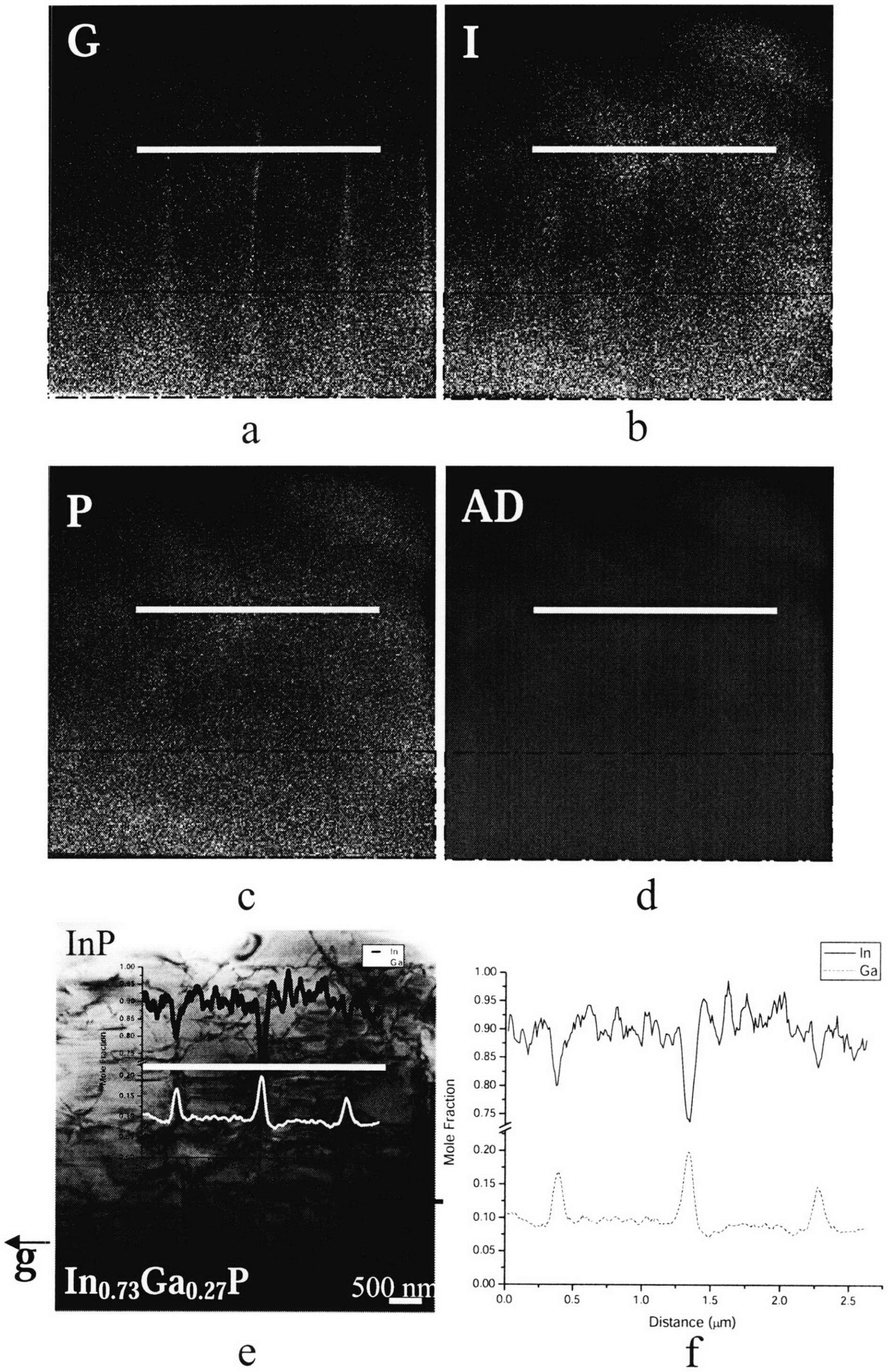

a b c d e f

Figure 6.12. InGaP graded buffer grown at 600 °C on an InGaAs virtual substrate. Figures (a)-(e) are cross section micrographs of the same region. Micrographs (a)-(d) are STEM results including a Ga element map (a), an In element map (b), a P element map (c) and an ADF image taken of the region under the diffraction condition in which the maps were taken. Micrograph (e) is a XTEM in a <220> beam condition. Figures (a)-(e) all have a line through them to denote the region the line scan shown in (f) was taken. Micrograph (e) has the line scan in (f) superimposed onto it to demonstrate how the composition line scan correlates with the diffraction contrast in the XTEM micrograph.

In Figures 6.12(a)-(d) a lattice-matched InGaP on InGaAs layer is highlighted with a box at the bottom of each figure. This layer was designed to be at a constant composition because the fluxes of precursor gases and the growth temperature were held constant during growth of this layer. Within this layer there is a change in morphology of the Ga-enriched region, however. Initially, the composition variation is slight and the distance between the vertical Ga-enrichments is small at the InGaAs/InGaP interface. However, as the constant flux layer is grown, the Ga-enriched regions narrow (the distance between them increases) and the Ga enrichment increases. (The extent of composition variation increasing as a function of thickness of the film was predicted by Ipatova *et al.* [79].)

These data reinforce the observations in Figure 6.4(b) and Figure 6.9(b) that shows that the moiré fringes have a larger wavelength towards the substrate and smaller wavelength as the growth continues as a larger wavelength implies smaller composition variation. The data also suggest that surface diffusion is the mechanism by which the phase separated regions are created. Since the phase separated region in the constant precursor flux and temperature layer undergoes a gradual change in morphology one can deduce that this is not a bulk phenomenon because if it were this entire layer, grown using the same conditions (same temperature, strain and gas flow settings), would have the same morphology. Bulk diffusion is known to be prohibitively slow even at growth temperatures ($1.4\text{x}10^{-18}\text{cm}^2/\text{s}$ in bulk GaAs at 700 °C) in these materials[80, 81] and though others have theorized that PS is caused by surface diffusion[67, 82] the morphological evolution of the phase separation we observe here is evidence to support this notion. Once fluctuations in strain and In composition exist, In tends to migrate away from the Ga-rich areas, further enhancing the Ga enrichment. Also, the change in morphology as the layer grown under the same conditions suggests the microstructure of a new layer is dependent on the strain state of the layer beneath in a similar manner as it is affected by the strain-state of the surface due to the misfit dislocation network.

Phase separation induced composition variations were large in this sample and led to a ρ_t=3.4x10^8/cm^2. The line scan from Figure 6.12 data indicates over 11% Ga composition difference between the matrix and inside the Ga-enriched region. Finally, as the graded buffer In content increases towards InP, eventually the Ga-enrichment becomes unstable and disappears. This occurs in sample 725$In_{0.25}Ga_{0.75}As$/600$In_{0.73}Ga_{0.27}P$ at around $In_{0.94}Ga_{0.06}P$.

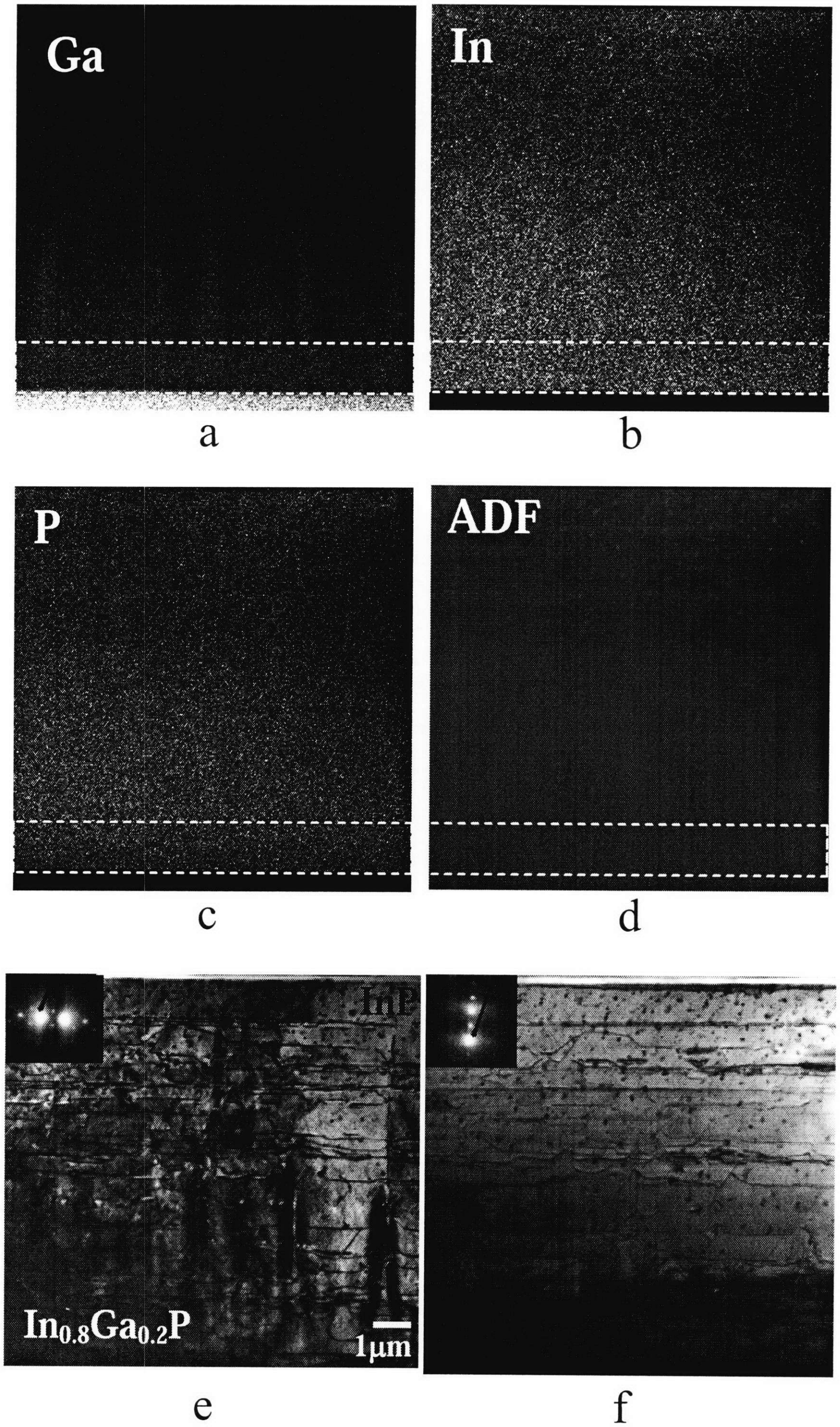

Figure 6.13. Figures (a)-(f) are cross section micrographs of sample 725$In_{0.32}Ga_{0.68}As$/625$In_{0.8}Ga_{0.2}P$ of the same region. Micrographs (a)-(d) are STEM results including a Ga element map (a), an In element map (b), a P element map (c) and the ADF image taken of the region under the diffraction condition in which the maps were taken. Micrograph (e) is a XTEM in a <220> beam condition while Figure (f) a XTEM micrograph is in an <004> beam condition. Note that the dark specks in Figure 6.13(e) and (f) are milling damage artifacts.

In an effort to avoid phase separation to reduce ρ_t, the InGaP graded buffer was grown at a higher temperature on the InGaAs platform, with a growth temperature increase from 600 °C to 625 °C. Figure 6.13 shows the InGaP graded buffer grown on an $In_{0.32}Ga_{0.68}As$ platform starting with an initial lattice-matched $In_{0.8}Ga_{0.2}P$. The InGaP material was grown at 625 °C while the InGaAs platform was grown at 725 °C. Similarly with Figure 6.12, highlighted by a dotted rectangle in Figure 6.13(a)-(d) the constant-flux and nominally $In_{0.8}Ga_{0.2}P$ layer has Ga enrichment that is first slight and wide and, as the growth continues, the Ga-enrichment becomes more localized while the enrichment increases. Evidenced by the STEM results, the 25 °C increase in growth temperature was not sufficient to move the InGaP graded buffer out of the phase-separated region.

Despite the overall failure to avoid phase separation, smaller composition variations were observed in Figure 6.13 compared to Figure 6.12 as evidenced in three ways: first from the weaker diffraction contrast in Figure 6.13(e), second from the fact that dislocations are more strongly blocked in Figure 6.12(e) than in Figure 6.13(e) and third from the EDS elemental maps. At 625 °C the Ga-enriched regions disappear around 9.5% Ga where as at 600 °C they were stable to around 6% Ga, seen in XTEM, implying that the Ga-enriched regions were more stable at 600 °C than at 625 °C. At 625 °C the apparent edges of the miscibility gap are at $In_{0.68}Ga_{0.32}P$ from Figure 6.11 and at about $In_{0.9}Ga_{0.1}P$ from Figure 6.13. This observation of Ga segregation fromo In-rich InGaP points to the possibility of an In-rich compound that is stable during growth conditions on the surface around $In_{0.75}Ga_{0.25}As$.

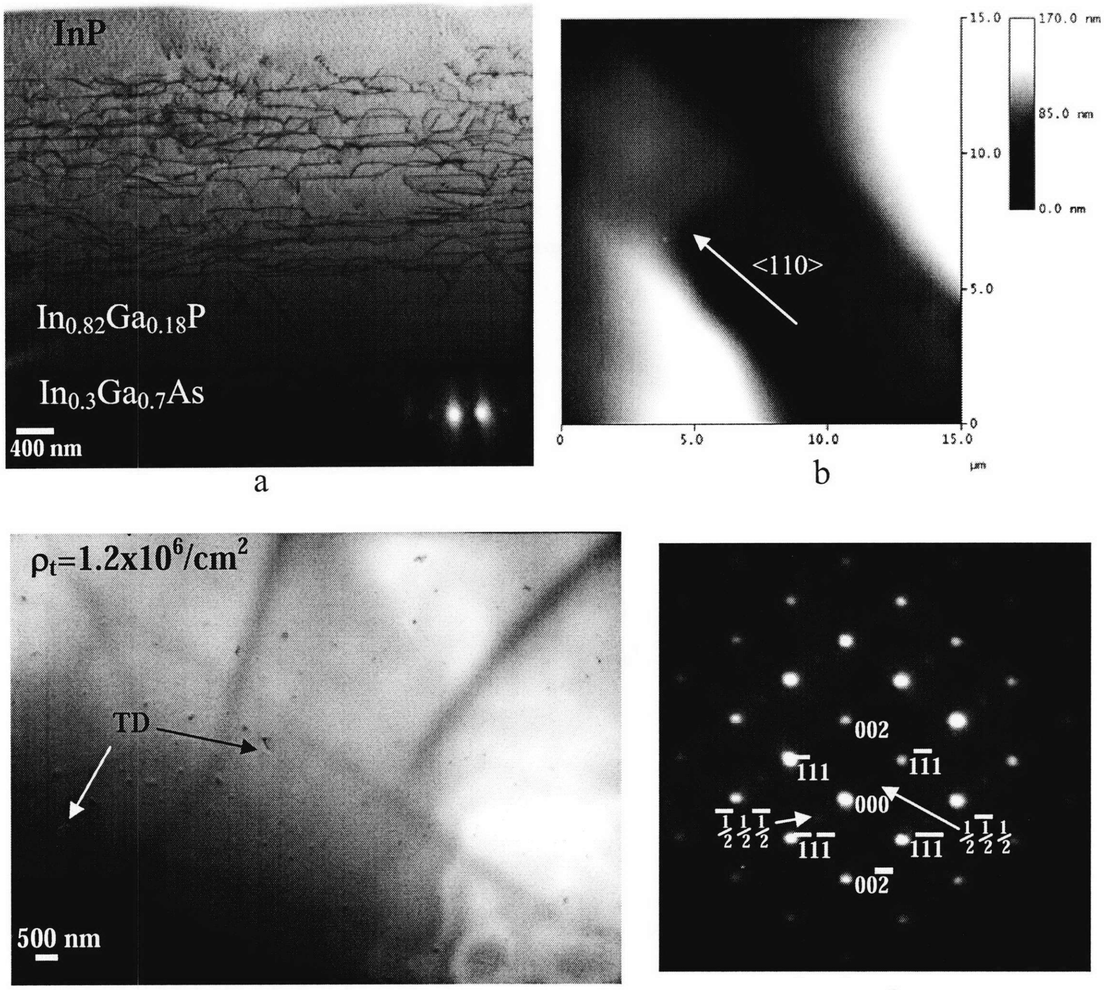

a b

c d

Figure 6.14. InGaAs and InGaP graded buffer with an InP cap on GaAs in XTEM (a), AFM (b), and PVTEM (c). Figure 6.14(a) and (c) are BF TEM images in the g=<220> diffraction condition. The RMS roughness of the AFM image, Figure 6.14(b), is 61.9 nm over the 15 μm X 15 μm area. The features other than the threading dislocations in the PVTEM are believed to be mill damage. In the micrograph in (d) CuPt-B ordering is visible in the InGaP graded layers.

As an increase of the growth temperature of the InGaP graded buffer by 25 °C reduced the extant of phase separation a further increase in the growth temperature was explored. The sample in Figure 6.14 was very similar to the hybrid samples described earlier, depicted in Figure 6.12 and Figure 6.13, except the InGaP was grown at 700 °C. Figure 6.14(a)-(d) shows the XTEM, PVTEM, AFM and on-pole diffraction micrographs respectively of sample 725$In_{0.3}Ga_{0.7}As$/700$In_{0.77}Ga_{0.23}P$, a graded buffer from GaAs to

InP using the InGaAs and InGaP materials systems. In this sample an InGaAs graded buffer platform was grown to a final composition of $In_{0.3}Ga_{0.7}As$ at 725 °C on top of which an InGaP graded buffer was grown at 700 °C to InP. We show here that phase separated regions are avoided and no threading dislocations can be seen in the cap in XTEM. In contrast to the InGaP graded buffers grown at lower temperatures (see Figures 6.11, 6.12, and 6.13), in Figure 6.14 there are no strong-contrast-regions perpendicular to the substrate surface that are caused by phase separation. As a result of being able to avoid phase separation, the threading dislocation density, as determined over many PVTEM micrographs, was $1.2 \times 10^6/cm^2$. The RMS (Root Mean Square) roughness over an area 15μm × 15μm was 61.9 nm and no trenches associated with phase separation were observed. CuPt-B ordering is observed in the InGaP graded buffer and is evident by the extra diffraction spots along one of the <111>-type directions in Figure 6.14(d) [83].

As discussed in the InGaAs materials system, the stress state of a material affects phase separation. In metal systems when the stress state was shown to affect phase separation, the phase separation led to a reduction in the elastic stress in the material[74-76]. This is also observed in InGaP, the phase separation by increasing the Ga content reduces the compressive lattice-mismatch strain in these graded buffer materials. As Figure 6.13(f) is taken in the [004] diffraction condition, this suggests that the displacement vector caused by the Ga-enriched phase separated regions lies in the (001) plane because, similarly to dislocations, when the displacement vector, **r**, is perpendicular to the diffraction vector, **g**, the contrast disappears. Knowing that these defects are Ga enriched suggests that the displacement vector reduces the strain in the compressive graded buffer films.

6.4.5 Dislocation Interactions with Phase Separation

Our work in metamorphic systems has been instrumental in our ability to understand the defects we observe in a broad context and allows us to engineer deposition to reduce the threading dislocation density. Many others have observed similar microstructure in III-V semiconductors[21, 23, 24, 41, 61, 64, 68, 78, 84-91]. Kim *et al.* spoke of the "strength" of what he called "branch defects" whose strength paralleled the strength of the TEM diffraction contrast[21]. In this work we have been able to identify branch defects as composition variations with the "strength" of the branch defects corresponding to the degree of composition variation. Kim *et al.* have observed that the increase in "strength" of branch defects increased the ρ_t by hindering dislocation glide.

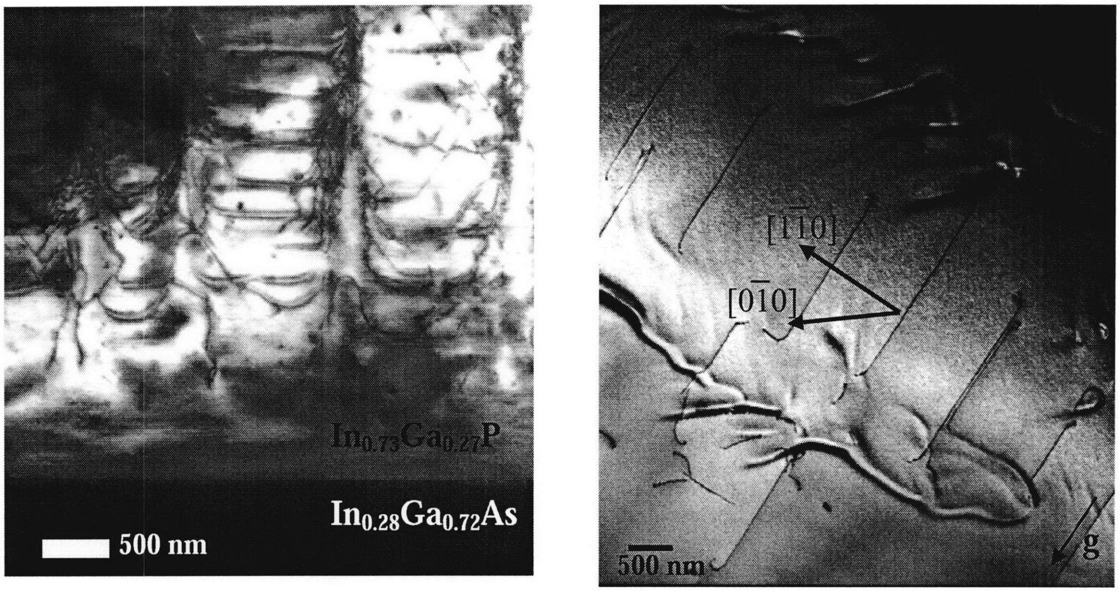

g →   a   b

Figure 6.15: Dislocations being pinned by composition variations in BF XTEM InGaP (a) and PVTEM $In_{0.36}Ga_{0.64}As$ (b). The XTEM micrograph (a) is enlargement from Figure 6.12 to show how the dislocations are completely blocked by the Ga enriched regions as they climb up the sides of the phase separation. The PVTEM micrograph (b) shows misfit dislocations being blocked by phase separated regions as the dislocations stop along the Ga enriched regions.

Dislocations are blocked and possibly generated by phase separation as depicted in Figure 6.15(a) and (b). The degree of composition variation leads to three regimes of interaction between these composition variations and dislocations. The first regime, where the composition variation is low and therefore the overall strength of the barrier to dislocation glide is low, is marked by no increase in threading dislocation density. Figure 6.10(b) is an example, where InGaAlAs has many slight composition variations, but, none large enough to stop threading dislocations, leading to a low ρ_t=1.3x10^6. The second regime, where the composition variations are greater, is marked by dislocation pileups at the phase separated regimes and thus an increase in ρ_t as shown in Figures 6.4, 6.6, 6.8(b), and 6.12 where threads arrest and possibly even nucleate in regions of composition changes yielding an elevated ρ_t. Phase separation has been shown to lead to dislocation pileups in other materials; for example it has been used to toughen metals[92, 93]. The third and final regime, where composition variations are large, is marked by dislocations being split into their partials producing a stacking fault. It is known in semiconductors that when a mixed dislocation goes through a region in tension (like a Ga-enriched region), the dislocation can separate into two partial dislocations[94] connected by a stacking fault. In Figure 6.16(a) and Figure 6.16(b) PVTEM micrographs from the same samples as depicted in Figure 6.12 and Figure 6.13, respectively, are shown. In the sample that has larger composition variations and effectively net tensile regions, $725In_{0.25}Ga_{0.75}As/600In_{0.73}Ga_{0.27}P$, stacking faults in plan view are seen, while sample $725In_{0.32}Ga_{0.68}As/625In_{0.8}\,Ga_{0.2}P$ shows no stacking faults.

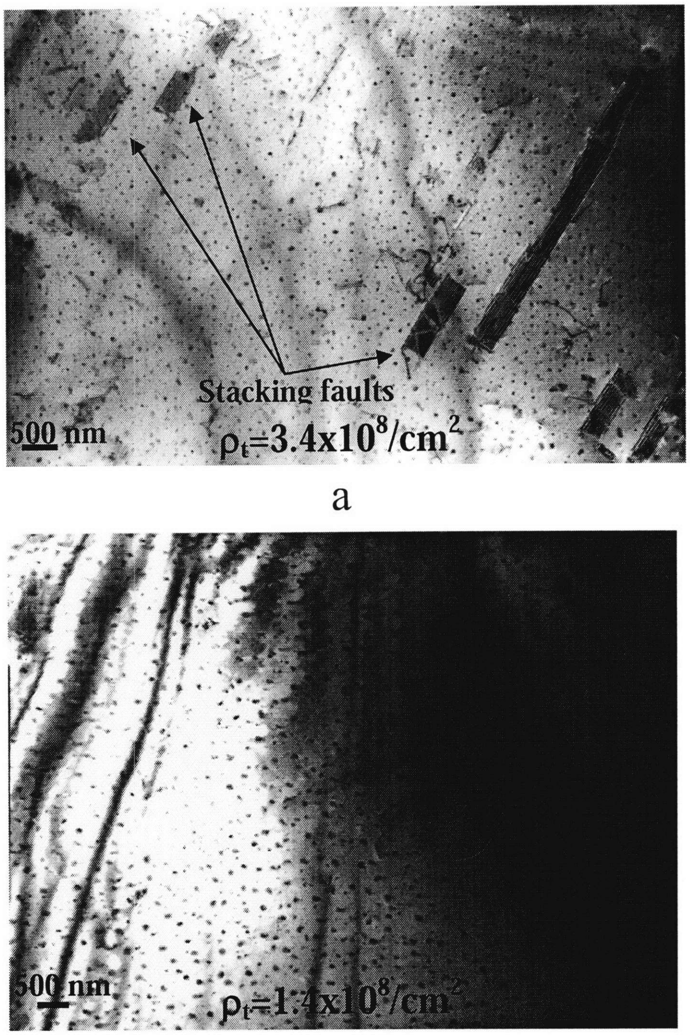

a

b

Figure 6.16: PVTEM micrographs of sample 725$In_{0.25}Ga_{0.75}As$/600$In_{0.73}Ga_{0.27}P$ (a) and sample 725$In_{0.32}Ga_{0.68}As$/625$In_{0.8}Ga_{0.2}P$ (b). Notice that there are many stacking faults in the low temperature grown InGaP (a) while there are none in the InGaP grown at 625 °C. The presence of stacking faults suggests that the partial dislocations which bind either end of the stacking fault were separated when the dislocation glided through a tensile region. The presence of stacking faults further supports the presence of Ga-enriched regions with a smaller lattice constant[94]. The dark, small, and round speckles uniformly distributed in both figures are damage cause by ion milling.

6.4.6 Growth Conditions to Avoid Phase Separation in Metamorphic In-Based Graded Layers

In addition to thermodynamics, kinetics must be considered when analyzing and engineering microstructures. A tool that envelops both thermodynamics and kinetics of phase transformations is the Time-Temperature-Transformation Curve (TTT Curve) depicted in Figure 6.17. The TTT curve, also called a C curve for its shape, illustrates the important role of time in determining microstructure. There are two regions in the TTT curve: the first is above and to the left of the curve and the second is below and to the right. The first region indicates an area where roughly no phase transformation in the system has occurred. The second region, to the right of the curve, is roughly where all of the material has undergone a phase transformation. Another aspect common in all TTT curves is the "C" shape. This shape indicates that longer times are required to transform a material from one phase to another at both low and high temperatures. This separation of the two regimes where phase separation can be avoided comes from the competition of thermodynamic driving force and diffusion.

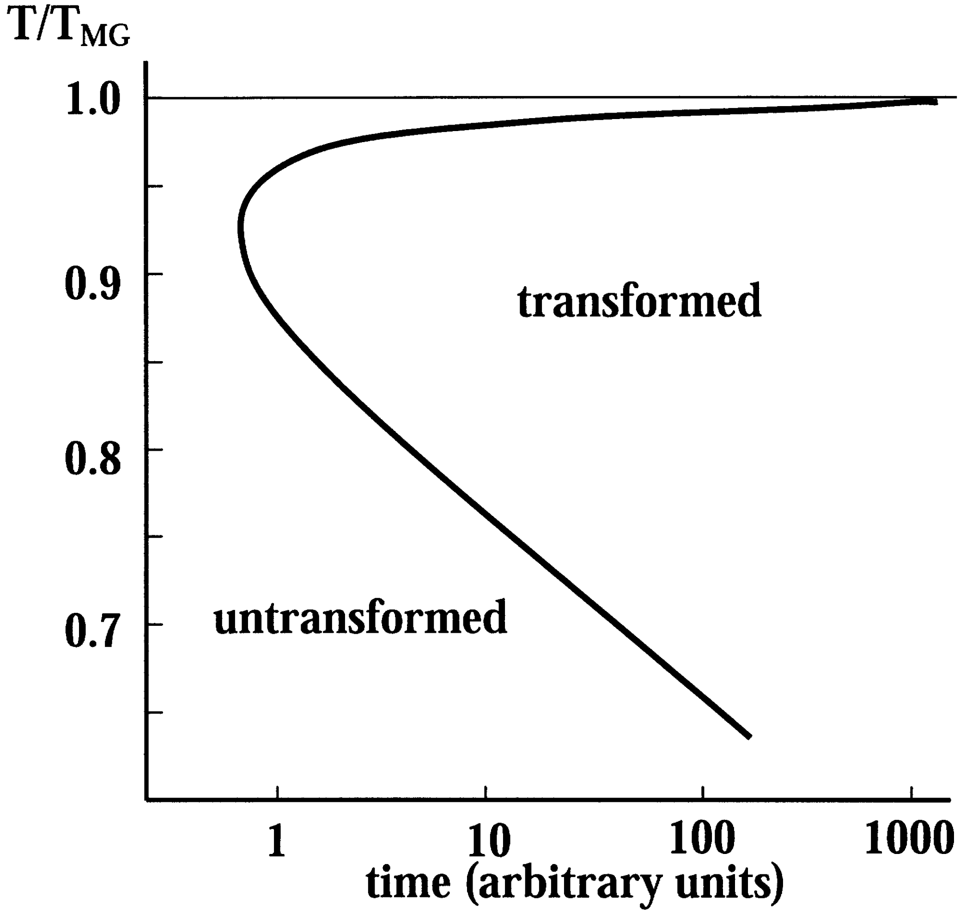

Figure 6.17 Schematic Time-Temperature-Transformation Curve (TTT Curve) designed after Huston *et al.* for a phase transformation[95]. The region to the left of the curve represents the conditions, time at a given temperature, of an untransformed material while the region to the right represents the conditions to transform a material. The curve represents schematically the conditions for which phase transformation starts to occur.

The driving force (thermodynamics) pushes the transformation forward while the diffusion (kinetics) allows the transformation to occur. At low temperatures, the driving force pushing the system towards phase separation is large; however, because diffusion can be negligible, the time required for the system to phase separate can be nominally infinite. At high temperatures as T approaches T_{MG}, the critical temperature above which no transformation occurs, the driving force is quite low and times required for phase separation become infinite again.

Using the TTT curve one can explain and predict the microstructure a material system will attain under certain growth conditions, and can explain our results and those in literature. When growing graded buffers at low temperatures, as is typical in MBE and some OMVPE growth, phase separation was not observed[42, 59, 64, 88]. However, after increasing the growth temperature, phase separation can be observed [21, 41, 42, 87, 88]. In two works, Bulsara *et al.* explored the conditions for the TEM contrast, what we interpret as phase separation, in the InGaAs materials system using MBE and MOVPE (Metal Organic Vapor Phase Epitaxy)[41, 42]. Interestingly, in these two works in the same materials system he was able to observe both an upper and lower limit in temperature above and below which, respectively, no phase separation was observed. At sufficiently high temperatures for a given composition, phase separation disappears as seen in this work and in others by Bulsara, Kim, and Mcgill[21, 24, 41, 42]. (Higher temperatures can usually only be attained with MOCVD as opposed to MBE due to the ability to supply an over pressure of both group III and V elements.)

There is some evidence that the phase separation in our samples may be similar to spinodal decomposition, in which a characteristic wavelength of decomposition is associated with a particular temperature of the transformation and is predicted to occur by Zunger[20] and Stringfellow[19]. In spinodally decomposed materials this wavelength increases with increasing temperature. Increasing wavelength with temperature has been reported by Kim *et al.* in the InGaP materials system[21]. In Figures 6.8, 6.9, and to a lesser extent in Figure 6.6, a characteristic wavelength is visible along a <100> direction. The wavelength illustrated in Figures 6.6, 6.8 and 6.9 is around 400 nm, which is significantly longer than the expected wavelengths associated with typical bulk spinodal decomposition which are often < 20 nm. Consequently, these longer wavelengths may actually suggest cellular precipitation instead of spinodal decomposition especially since the characteristic wavelength in both spinodal decomposition [95] and cellular precipitation[96, 97] are expected to increase with increasing temperature. Cellular precipitation may be a likely candidate because cellular precipitation requires an interface with enhanced diffusion. Zunger [20] and Stringfellow[19], however, suspect spinodal decomposition in these materials as they have calculated positive enthalpies of mixing in these materials systems. Other authors have seen contrast on a finer scale like Mahajan *et al.* with a 15 nm periodicity[78], and Chu *et al.* with a periodicity of 5-15 nm in TEM[98] both in InGaAsP. Both Mahajan and Chu observe a coarser periodicity as well, however. These variations in wavelength make conclusions as to the mechanism of the phase separation periodicity difficult.

As phase separation in graded buffers is unwanted, influencing the morphology of the phase separation can be achieved by considering thermodynamics and kinetics. Changing the growth temperature, as illustrated in this work, changes the thermodynamics and can be used to avoid phase separation. In addition, if we assume there is a driving force on the surface to create compositional variations (thermodynamics), as there is in some systems described in this paper, kinetic constraints may prevent this composition variation from forming. Gonzalez *et al.* have observed that an increase in V/III ratio reduces phase separation[99] since the group III element surface diffusivity is reduced. Similarly, one could increase the growth rate as Wang *et al.* have done[63] to lock atoms into the bulk before they have a chance to find a cluster of like atoms and reduce the phase separation. Thus for thin-film systems, the distance an adatom travels on the surface is the key parameter. This distance is affected by surface diffusivity, D_s, and time to quenching (i.e. when the surface atoms are locked into a position in the bulk). Since the time an adatom resides on the surface is inversely proportional to the growth rate, G_r, $\sqrt{D_s / G_r}$ is a key parameter in determining whether phase separation occurs. Decreasing D_s and increasing in G_r will minimize phase separation.

Consideration of the thermodynamics and kinetics of phase separation is necessary but not sufficient to achieve low ρ_t and ensure high-quality material, however. To minimize ρ_t, misfit dislocation length must be maximized over many interfaces. Phase separation can easily become the limiting factor and thus control the misfit dislocation length yielding a ρ_t on the order of $10^9/\text{cm}^2$. However, once phase separation is avoided threading dislocation velocity dictates misfit dislocation lengths and because dislocation velocity is exponentially dependent on growth temperature, growth at high temperatures becomes critical to reduce ρ_t. Consequently, using low temperature growth to avoid phase separation results in ρ_t of $10^7/\text{cm}^2$ or higher[88]. As a result, one must use high growth temperatures close to or beyond T_{MG} to avoid phase separation. The use of high temperatures satisfies both criteria, of avoiding phase separation and keeping dislocation velocities high to achieve low threading dislocation densities. In this way low threading dislocation densities of 10^5-$10^6/\text{cm}^2$ can be achieved.

Figure 6.18 illustrates the importance of using high growth temperatures to avoid phase separation. Figure 6.18 shows bright-field XTEM and PVTEM micrographs of a commercially available $In_{0.52}Al_{0.48}As$ graded buffer grown by MBE at a temperature << 600 °C. The InAlAs graded buffer has a HEMT device layer on the top. While there is no strong phase separation evident, the dislocation density is $\rho_t \sim 10^8/\text{cm}^2$ (evident by the observation of a dislocation intersecting the surface in XTEM) and is high because the growth temperature of this material is low, and therefore the threading dislocation velocity is low.

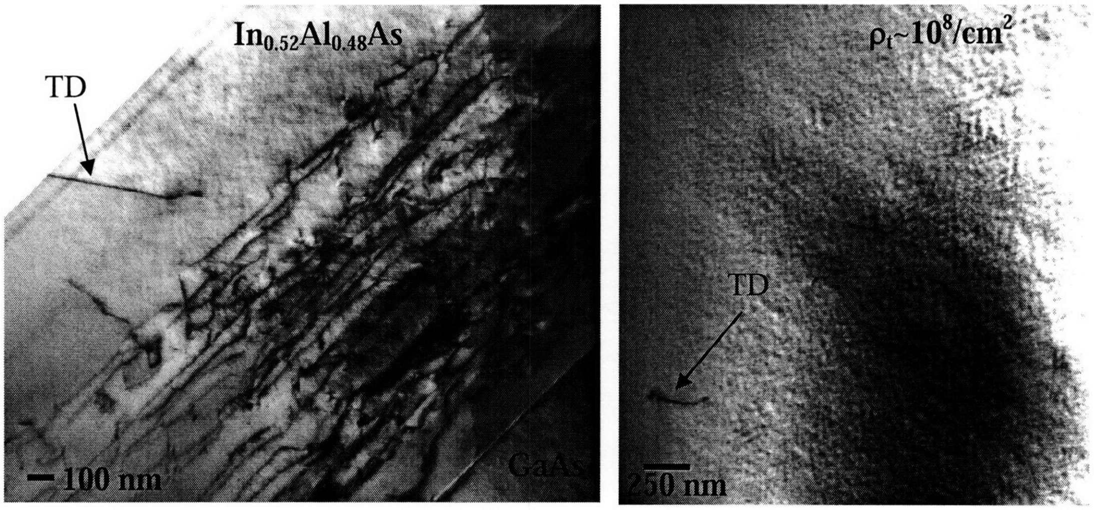

a

b

Figure 6.18. Bright-field, g=<220> XTEM (a) and PVTEM (b) micrographs of a commercially available MBE grown In$_{0.52}$Al$_{0.48}$As graded buffer on GaAs using the InAlAs materials system. There does not seem to be any large composition variations. However, a fine speckle contrast is visible in both (a) and (b) and may be the results of slow diffusion at low growth temperatures typical of MBE growth.

Figure 6.19 schematically summarizes the discussion of the affects of temperatures on ρ_t in the previous discussion for materials systems with and without phase separation. For a material without phase separation, like the SiGe system, ρ_t is exponentially dependent on temperature. A material with phase separation follows the same ρ_t curve as one without phase separation at high and low temperatures. In region (I) of Figure 6.19 for a material with phase separation, composition variations are slight with a high frequency or non-existent because the surface diffusion is low. Consequently, increases in growth temperature correlate with a decrease in ρ_t because dislocation velocities are increasing and they are not hindered by the weak composition variations. However, further increases in temperature leads to region (II) and phase separation starts hindering dislocation movement, thus increasing ρ_t. Composition variations caused by phase separation is strong in the third region (III) resulting in insurmountable barriers for dislocations to glide through despite their high velocities (see Figure 6.15 for blocked dislocations in both the InGaAs and InGaP materials systems). Region (IV) is the optimal region to grow graded buffers because no phase separation is present and dislocation velocities are high.

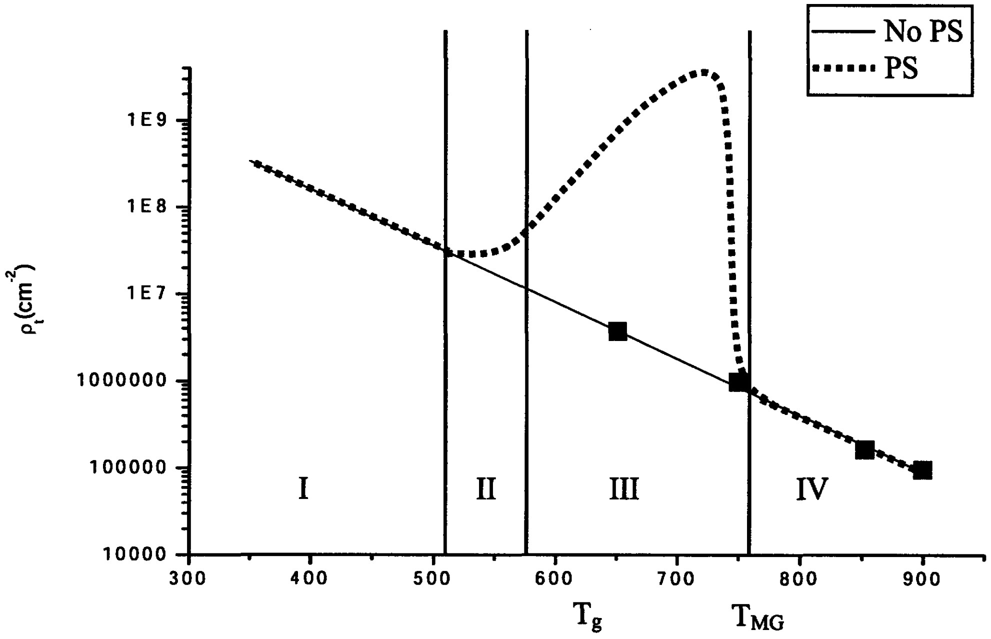

Figure 6.19. Schematic graph showing threading dislocation density, ρ_t, as a function of growth temperature, T_g, for a materials system with phase separation (PS) and for the same system if one could repress phase separation (No PS). There are four regions associated with this plot, (I) no phase separation with slow dislocation velocities, (II) dislocation velocities increase and phase separation is weak, (III) phase separation is strong, (IV) no phase separation and fast dislocation velocities. The "No PS" line is based on real data in the SiGe system from Leitz *et al.*[100] and the 4 squares are actual data points in the SiGe system.

6.4.7 Photoluminescence Comparison

Our analysis and understanding of phase separation in III-V semiconductors have allowed us to demonstrate low dislocation density InP on GaAs through a hybrid InGaAs and InGaP graded buffer (see Figure 6.14). To further demonstrate the quality of the graded buffer and establish its use for minority carrier devices, a PL structure was grown on top of a similar InGaAs and InGaP hybrid graded buffer as depicted in Figure 6.14 [see Figure 6.20(a)]. The PL structure consisted of a 55 nm $In_{0.54}Ga_{0.46}As$ well and 120 nm InP clad, which were grown at 725 °C. The PL structure had a fairly thick 55 nm $In_{0.54}Ga_{0.46}As$ well to avoid quantum confinement effects which would hinder analysis of the material quality because quantum wells are affected less by ρ_t[101].

For comparison, the same PL structure that was grown on the graded buffer was also grown on an InP substrate and on a GaAs substrate without a graded buffer as control samples. With this sample set, we compared the quality of our graded buffer to an InP substrate and to a PL structure grown directly on GaAs. The PL structure on InP consisted of a homoepitaxial InP layer grown at 725 °C followed by the $In_{0.54}Ga_{0.46}As$ well and approximately 120 nm InP cap layer. The PL structure on GaAs was fabricated by first depositing about 100 nm of InP at 500 °C to ensure a smooth, specular film on top of which the PL structure explained above was grown [Figure 6.20(b)]. (Fastenau *et al.* have suggested that InP grown on GaAs from 460-500 °C yields the best electron transport properties[60].) The threading dislocation density of the PL structure on GaAs is very high $\rho_t > 1\times10^8/cm^2$ due to the large amount of lattice-mismatch relieved abruptly across a single interface. AFM was performed on the final structures and the RMS roughness over a 15μm × 15μm area was 1.3 nm on the bulk InP sample and 15.7 nm on the low-temperature-grown InP sample. Both appeared specular to the unaided eye.

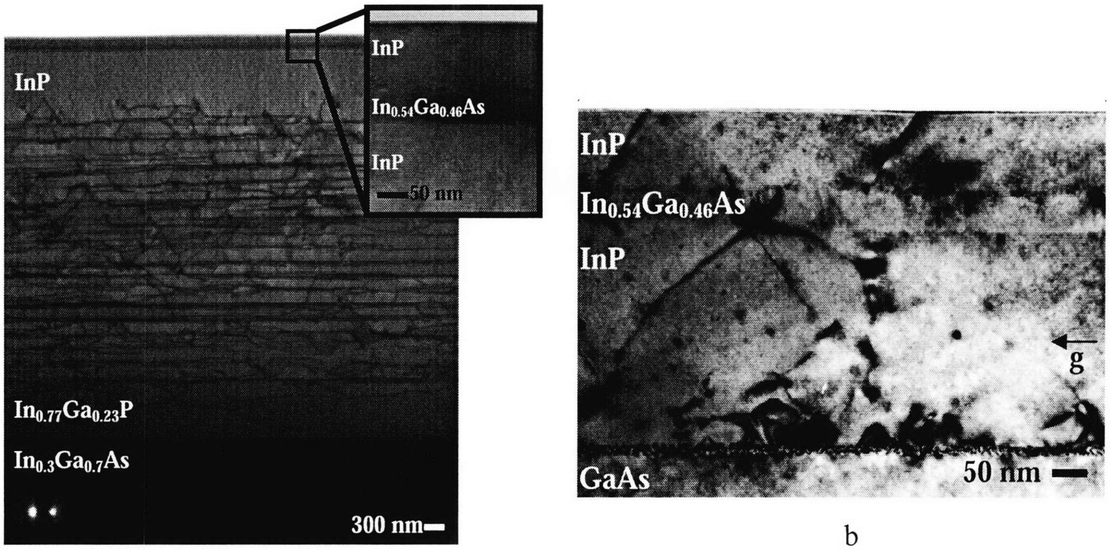

b

a

Figure 6.20. PL structures grown on GaAs (a) with a graded buffer and (b) without a graded buffer. The PL structure consists of a 55 nm $In_{0.54}Ga_{0.46}As$ well clad with InP. Notice in (b) the large density of misfit dislocations at the InP/GaAs interface visible because the sample is slightly tilted.

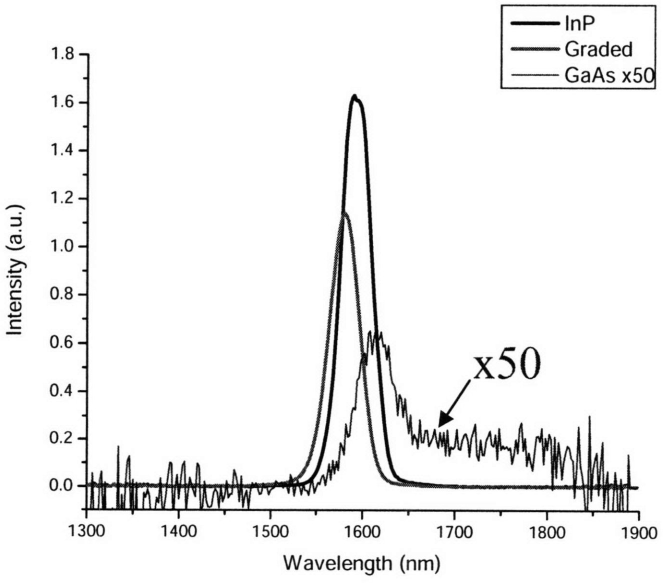

Figure 6.21: PL data taken at 20K of a 55 nm $In_{0.54}Ga_{0.46}As$ well on three different platforms using a Ge detector. These three InP platforms are (1) an InP bulk substrate (denoted as InP), (2) an InGaAs to InGaP graded buffer structure outlined above (denoted as Graded), and (3) an InP layer grown at 500 °C on GaAs (denoted as GaAs x50) listed by intensity from highest to lowest in Figure 6.21. The PL data of the structure grown on low temperature InP on GaAs was multiplied by a factor of 50 to be able to see the peak on the same scale as the other two. The integrated intensity of the $In_{0.54}Ga_{0.46}As$ on the graded structure was about 70% of that grown on bulk InP. The FWHM of the three peaks, from highest to lowest, were about 39 nm for the InP and graded structures and 48 nm for the GaAs structure. Notice the long red tail in Figure 6.21 for the PL structure on GaAs.

Room- and low-temperature (20K) PL were performed on the three aforementioned samples: InP on bulk substrate, InP on a graded buffer, and InP grown at 500 °C on GaAs. All PL data at 20K and at room temperature were calibrated for detector and grating response using a tungsten light source. Figure 6.21 shows the results of the low-temperature measurements. In Figure 6.21 three peaks are evident, those of the $In_{0.54}Ga_{0.46}As$ on bulk InP, on our graded buffer, and on low temperature InP on GaAs. The PL response for the structure grown on low-temperature InP on GaAs was multiplied by a factor of 50 to be able to show the plot on the same graph. Though not a completely quantitative metric to compare the qualities of two different materials, comparison of the integrated intensities of the PL structure on our graded buffer is about 70% of the integrated intensity of the same structure on InP. The FWHM (Full Width at Half Maximum) of the PL structure on InP and the graded buffer were approximately the same, namely 39 nm; while the FWHM of the PL structure grown on the low-temperature InP on GaAs was about 48 nm. Interestingly, in the PL structure on GaAs a long red tail is evident indicative of a large number of defects at energy levels below the bandgap. Another observation is that the peak energy of the quantum well luminescence is different in the samples: 1596 nm, 1584 nm, and 1620 nm for the PL structure on InP, the graded buffer and on GaAs, respectively. The blue shift of the PL structure on the graded buffer is probably because the InP on the graded buffer is slightly compressed (by 0.14%) leading to a blue shift.

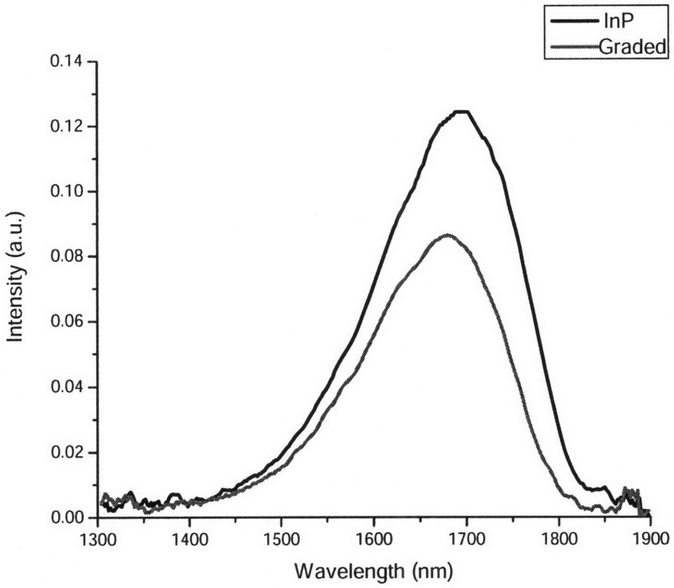

Figure 6.22. Room temperature PL on a 55 nm $In_{0.54}Ga_{0.46}As$ well clad with about 120 nm of InP on an InP bulk substrate and an InGaAs to InGaP graded buffer structure outlined above. PL data of the structure grown on low temperature InP on GaAs is not displayed because no peak was evident above background noise. The integrated intensity of the PL structure grown on the optimized graded buffer was about 68% of the intensity on the InP bulk substrate. The FWHM for both peaks are 184 and 185 nm for the PL structure on InP and on the graded buffer respectively.

Since most devices need to work at room temperature, good room temperature PL is critical for commercialization of a device and is a difficult standard to achieve. The room temperature PL results are shown in Figure 6.22. Only the data from the PL structure on InP and on the graded buffer are shown because the PL structure on the low-temperature-grown InP did not luminescence at a level above the detector noise at room temperature. As with the low-temperature data, the PL peak from the graded buffer is bluer than the peak from bulk InP. The FWHM of these two peaks are 184 and 185 nm for the PL structure on InP and on the graded buffer respectively (this corresponds to about 3.2kT). The ratio of the integrated intensities of the two peaks at room temperature is 68% at room temperature compared to 70% at 20K. Thus there was not much change between the integrated intensity ratio at room temperature and 20K. The lack of temperature dependence suggests that there are relatively few defect transitions to freeze out in the PL structure grown on the graded buffer, and therefore the lower intensity from the graded buffer may not be the result of defects. Given the minimum error in quantitative PL comparison combined with the fact that carriers may reach the highly dislocated buffer below the heterostructure, the luminescence intensity is approximately the same within the accuracy of the experiment. These PL results suggest that the quality of the InP on GaAs using the hybrid graded buffer can be used for minority carrier devices.

The PL luminescence from our InP/GaAs using optimized graded buffers is a significant improvement over other room temperature PL data comparing structures grown on InP to those on GaAs. Tangring *et al.* have reported PL data on $In_{0.34}Ga_{0.66}As$ graded buffers grown at 450 °C by MBE with a factor of 6 lower on their structures grown on GaAs[102] compared to InGaAsP on InP. With the framework schematically illustrated in Figure 6.19 established, the factor of 6 lower intensity from graded buffers by Tangring *et al.* may be due to the fact that they are growing at low temperatures, namely 450 °C, in region I in Figure 6.19[102]. In this region they are able to avoid phase separation but they are not able to achieve $\rho_t \sim 10^6/cm^2$ because of their low growth temperatures and hence their factor of 6 lower intensity.

6.5. Conclusion

To achieve high-quality InP on GaAs, an understanding of phase separation in these materials was required. As part of that understanding, a one-to-one correlation between diffraction contrast in TEM and Ga-enrichment was demonstrated (see Figures 6.7, 6.11, 6.12, and 6.13). A strong correlation between trenches observed through AFM micrographs and phase separation in TEM was also observed in Figures 6.4, 6.6, and 6.9. Because dislocations were strongly blocked by these Ga-enriched regions, the ρ_t could increase by over a factor of 2000 over an optimized material. Strain appears to play a strong role in the formation of these Ga-enriched regions sometimes causing the Ga-enrichment to lie along <110> directions instead of the elastically soft <100> type directions and also causing the variations in morphology, width and strength, for a layer grown under the same circumstances. Also derived from analysis of layers grown under the same conditions, is that the morphology of the film changed with growth implies that surface diffusion enabled this morphology and that subsequent growth freezes in surface structures. Phase separation decreases by decreasing the surface diffusion and/or increasing the growth rate of the film. In the $In_xGa_{1-x}P$ materials system with $x > 0.73$ at 600 and 625 °C the material phase separates to a Ga rich component.

Through the understanding of the phase separation process, two alloy systems were used with appropriate growth temperatures to avoid phase separation and achieve high-quality InP on GaAs. The quality of the hybrid InGaAs and InGaP graded buffer resulted in InP on GaAs with low ρ_t, ρ_t=1.2x10^6/cm^2, and PL luminescence comparable to bulk InP. The lack of temperature dependence on the ratio of the luminescence intensity is further testament to the comparable quality of the InP on GaAs using the hybrid graded buffer. This comparable PL intensity suggests the optimized hybrid graded buffer can enable InP-based minority carrier devices on GaAs .

An implication of this work is that any lattice constant between GaAs and InP can be created with a level of threading dislocations sufficient for minority and majority carrier devices. This achievement may allow the use of novel high band offsets, like between indirect $In_{0.25}Al_{0.75}As$ and direct $In_{0.25}Ga_{0.75}As$ with a band offset of approximately 1.1eV.

Chapter 7. Relaxation of Highly Strained InP and InGaAs

As mentioned earlier, the research towards high-quality InP on GaAs took two paths. The first path, discussed in the previous chapter, led to the successful demonstration of high-quality InP on GaAs by using the hybrid InGaAs and InGaP graded buffer. The second path utilized the $In_{0.34}Ga_{0.66}As$ platform which was developed early on. This platform was used to grow lattice-mismatched InP directly on this $In_{0.34}Ga_{0.66}As$. Since $In_{0.36}Ga_{0.64}As$ is close to the InP lattice constant, it is reasonable to explore growing the low mismatched InP/ $In_{0.36}Ga_{0.64}As$ to see if a low threading dislocation density can be achieved in a relaxed InP layer.

InP grown directly on GaAs leads to poor material quality with threading dislocation densities > 10^8 /cm^2. However, InP grown on lattice constants between GaAs and InP has not been previously explored. An InP film was grown on the relaxed $In_{0.36}Ga_{0.64}As$/graded InGaAs/GaAs to determine if it would relax without the nucleation of many dislocations. Though dislocation nucleation was prevalent, the resulting work enabled insight into the activation of alternative slip systems in mismatched semiconductor epitaxy.

7.1. Introduction

This work investigates mismatched interfaces between InP and metamorphic templates with lattice constants between that of GaAs and InP. InP on GaAs is of interest to bring InP materials and devices to a GaAs platform. We investigate InP/InGaAs interfaces to determine the extent of mismatch that InP can experience and remain high-quality, low threading dislocation density. To that end, the dislocation morphology at the interface is key to determining if the InP can be of high-quality (i.e., have a low threading dislocation density).

Most often reported at lattice-mismatched interfaces are 60° dislocations belonging to the primary-slip system or Lomer edge dislocations at low and high strains, respectively. In the low lattice-mismatched regime (strain lower then about 1%) where 60° dislocations dominate the interface, there is a low threading dislocation density in the top layer. In the high lattice-mismatch regime, larger than about 2.5% strain, the interface is dominated by Lomer dislocations resulting in high threading dislocation densities. Usually there is a relatively sharp transition between the low and high mismatch strain regimes, where the presence of 60° misfit dislocations is replaced with the presence of Lomer edge dislocations. At the InP/InGaAs interface reported here, we observe a regime in which the primary 60° dislocation glide system begins to mix with the activation of a secondary-slip system at intermediate levels of mismatch strain.

The primary-slip system in the FCC (Face-Centered Cubic), diamond, and zinc-blende crystal structures is $a/2<110>\{111\}$, where dislocations have (the Burgers vector, $\vec{b}$) $\vec{b}=a/2<110>$, and they slip on $\{111\}$-type planes. The primary-slip system is not the only slip system observed in these materials, however. Secondary-slip systems have been observed in FCC metals and semiconductors. Slip on {100} planes in FCC metals have been observed by Karnthaler[103] and Carrard[104] while slip on {110} planes in FCC metals have been observed by Stevens[105], Le Hazif[106], and Pichaud[107]. Slip on {110} planes have also been observed by many in semiconductors as well[108-119] usually with films under high lattice-mismatch strains. Since slip on {110} planes was often observed in this study, henceforth in this paper the term secondary-slip dislocations will refer to dislocations that belong to the

$a/2<110>\{110\}$ system, those that glide on {110} planes with a $\vec{b}=a/2<110>$. Since these secondary-slip dislocations are pure edge, these dislocations will also be referred to as 90° dislocations in contrast to the primary-slip, 60° dislocations.

The factors that lead to relaxation via a slip system other than the primary are the difference between the Schmid factors of the two slip systems as well as the difference in Burgers vectors. For example, the primary-slip system may not be active because the Schmid factor is too low which resolves the shear stress onto the slip plane. For example, Zhang *et al.* have observed dislocations belonging to the $a/2<110>\{113\}$-slip system when growing lattice-mismatched $In_{0.1}Ga_{0.9}As$ on (110)-oriented GaAs[120, 121]. Also, the effective Burgers vector for the secondary-slip system can be larger than that of the primary-slip system. In the case of diamond or FCC structure materials, the secondary-slip system has a $\sqrt{2}$ larger effective Burgers vector that relieves about 40% more strain. However, the secondary-slip system can have a larger shear modulus, increasing the dislocation energy and partially or completely compensating for the increase in effective Burgers vector.

In this paper, we investigate the strain and temperature dependence on the activation of the secondary-slip system in the InP/InGaAs and InGaAs/InGaAs interfaces. A critical strain is identified for the semiconductors studied in this work to relax via the secondary-slip system. Once the secondary-slip system is active, relaxation of the film occurs via both the primary- and secondary-slip systems the extent of which is a function of temperature. Low temperatures favor relaxation via the secondary-slip system. Three regimes of semiconductor relaxation for the InP/InGaAs interface are observed in this work: the low lattice-mismatch regime which relaxes by 60° dislocations, the medium lattice-mismatch regime which relaxes by both primary- and secondary-slip systems, and the high lattice-mismatch regime which largely relaxes via Lomer edge dislocations. Lomer dislocations are a third type of dislocation seen in this work which belong to the a/2<110>{100} slip system whose Burgers vector lies completely in the (001) plane. Unlike the other two dislocations discussed, Lomer dislocations are sessile for growth on (001) crystals.

7.2. Experimental

Before growth, nominally on-axis (001) GaAs substrates were cleaned in two solutions. First a 10:1 H_2O:HCl solution for one minute to achieve a hydrophobic surface. The substrate was rinsed with deionized water and then placed in a 20:1:1 H_2SO_4:H_2O:H_2O_2 solution for 15 s to mildly etch the surface. Finally, after rinsing again, the substrate was again placed in the first solution for one minute, rinsed, and dried with N_2.

Semiconductor films were grown using an atmospheric pressure Thomas Swan, 2" horizontal MOCVD system. The precursors used in this study were tri-methyl In (TMIn), tri-methyl Ga (TMGa), AsH_3 and PH_3. The growth temperatures used in this study were from 500-750 °C. The substrates were placed on the upstream side of the approximately 7" long susceptor. They were not placed in a rotating pocket in the center of the susceptor designed to hold the wafer. The placement of the wafer on the upstream side of the susceptor was critical because at the high growth temperatures for the graded buffers used in this study, most of the In is deposited at the front of the susceptor. Consequently, little TMIn get to the center of the susceptor making high In content films grown in the center impossible.

After placing the GaAs substrate on the upstream side, it was heated to a temperature of 700 °C for 5 minutes under an AsH_3 overpressure to remove any native oxide. Before growth of lattice-mismatched films, a homoepitaxial GaAs film was grown at 700 °C. All of the samples grown in this study started with an InGaAs graded buffer. Figure 7.1(a) is a schematic illustration of these structures while Table 2 lists the key features of all of the samples in this work including: the composition of the highly stressed layer, its thickness (t), the temperature it was grown (T_g), and the final composition of the InGaAs graded buffer (x). The InGaAs graded buffer gradually increased the In composition to a final composition around $In_{0.36}Ga_{0.64}As$ (except for the sample 12 in Table 2). The InGaAs graded buffers were grown at 750 °C at a grading rate of 0.4% misfit /μm and were of high-quality having a threading dislocation density less then $2x10^6/cm^2$[41, 122]. Highly stressed layers of InP or $In_xGa_{1-x}As$ with x=0.53 or x=0.4 were then deposited on these InGaAs platforms at various temperatures and thicknesses. The InP growth rate at all temperatures was about 0.7 nm/s.

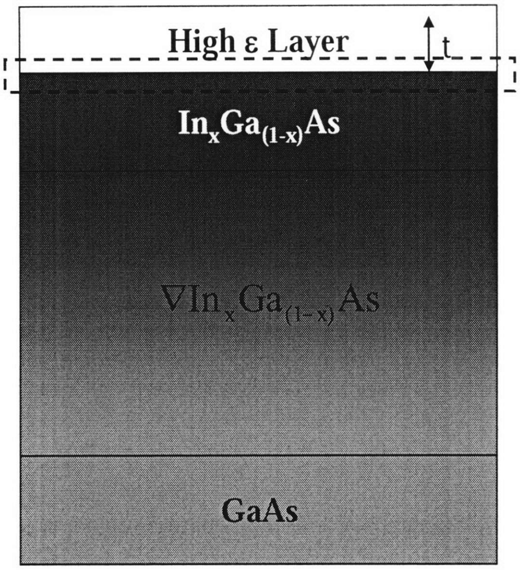

Figure 7.1: The structure of most samples in this study. The highly stressed layer, usually InP, is deposited on a graded buffer usually to a final composition around $In_{0.36}Ga_{0.64}As$. The highly stressed layers are of thickness (t), on a graded buffer whose final composition is x, see Table 2 for details about each sample.

Sample	x	High ε Layer	f	t (Å)	T_g (°C)	ε
1	0.35	InP	0.012	44	500	0.012
2	0.35	InP	0.012	95	500	0.012
3	0.38	InP	0.011	116	500	0.01
4	0.37	InP	0.011	150	500	0.009
5	0.34	InP	0.013	217	500	0.007
6	0.34	InP	0.013	576	500	0.007
7	0.34	InP	0.013	73	560	0.012
8	0.37	InP	0.011	138	560	0.009
9	0.37	InP	0.011	104	625	0.01
10	0.39	InP	0.01	185	625	0.008
11	0.35	$In_{0.53}Ga_{0.47}As$	0.012	185	500	0.008
12	0.1	$In_{0.4}Ga_{0.6}As$	0.021	185	500	0.008

Table 2: This table describes key features of samples 1-12 including the composition and thickness of the highly stressed layer (t), grown on top of a graded buffer with final composition, x. The composition of the graded buffer and the final layer dictate the lattice-mismatch (f) between them. The highly stressed layer was grown at a growth temperature, T_g. Both t and x refer to the t and x in Figure 7.1. The elastic strain remaining in the highly stressed layer (ε), is also listed above. Note that all InGaAs graded buffer platforms were grown at 750 °C.

The films were characterized *ex situ* using TEM and x-ray diffraction. TEM was performed at 200 keV on JEOL 200, 2000 and 2010 microscopes. The thicknesses of the highly stressed layers, being thin, were determined by high resolution TEM in the JEOL 2010. The TEM samples were prepared by mechanical polishing to a thickness of about 10 μm and thinned to electron transparency using a Gatan Dual Ion Mill or a Gatan Precision Ion Polishing System (PIPS). The composition and strain of the underlying InGaAs platforms were determined using the (004) and (224) peaks in a Bede triple axis x-ray diffractometer using a Rigaku RU200 generator operated at 60kV and 200mA.

7.2.1 TEM and $\vec{g}\cdot\vec{b}$ Analysis

In the case of semiconductors with (001) orientation under a small amount of compressive stress, the layers relax via the primary-slip system, $a/2<110>\{111\}$ [8]. For the (001) wafer orientation, the {111} glide planes intersect the growth plane along <110>-type directions, and therefore misfit dislocations lie along orthogonal $\langle 110\rangle$ directions in the (001) mismatched interface. Figure 7.2(b) shows a typical PVTEM micrograph highlighting the relaxation mechanism of a low lattice-mismatch InP film that was initially slightly compressed when grown on $In_{0.98}Ga_{0.02}P$. (This InP/InGaP very low mismatch interface is shown as an example of low lattice mismatch. Most of this paper explores the InP/InGaAs interfaces at larger lattice mismatches.) The misfit dislocations relieve the small compressive lattice-mismatch stress between the InP and InGaP. The interface where the misfit dislocations reside is highlighted by a box in the schematic diagram of the structure in Figure 7.2(a). For more details of this high-quality

InP on GaAs growth see reference [122]. As can be seen in Figure 7.2 (b), the misfit dislocations lie along the $\langle 110 \rangle$-type directions and indicate that relaxation occurred via the primary-slip system. Lomer dislocations also lie along $\langle 110 \rangle$ directions on the (001) surface, however. In order to determine that dislocations lying along $\langle 110 \rangle$ directions are primary-slip dislocations (so called 60° dislocations) and not Lomer dislocations, $\vec{g} \cdot \vec{b}$ analysis was performed.

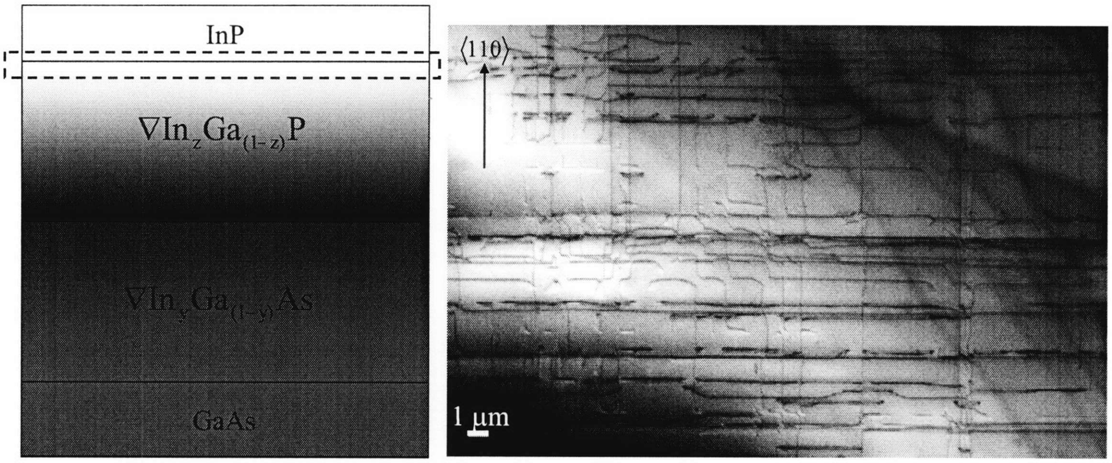

a

b

Figure 7.2: Relaxed InP that was under a small amount of compression via an InGaAs/InGaP graded buffer on GaAs[122]. (a) shows the structure upon which the InP film was grown. (b) shows a bright-field, $\vec{g} = \langle 220 \rangle$, PVTEM micrograph of relaxed InP/InGaP on a graded buffer whose final composition is $In_{0.98}Ga_{0.02}P$ just underneath the InP. The misfit dislocations seen in (b) are from the interface boxed in (a).

In the $\vec{g} \cdot \vec{b}$ analysis used in this paper, we perform a number of two-beam diffraction conditions in the TEM of the same area, noting the variation of contrast under different two-beam diffraction conditions, which excite the image with different diffraction vectors, $\vec{g}$. If a dislocation disappears (contrast is completely absent) in a particular two-beam condition, that dislocation has a Burgers vector, $\vec{b}$, and line direction, $\vec{u}$, in the diffraction condition that satisfies both[49]:

$$\vec{g} \cdot \vec{b} = 0 \qquad \textbf{Equation 19}$$

and

$$\vec{g} \cdot (\vec{b} \times \vec{u}) = 0. \qquad \textbf{Equation 20}$$

(In practice, dislocation contrast can disappear when Equations 19 and 20 are not exactly satisfied as well. Dislocations lose most contrast when $|\vec{g} \cdot \vec{b}| \leq \frac{1}{3}$ [49].)

Since both primary-slip (60° dislocations) and Lomer edge dislocations lie along $\langle 110 \rangle$ directions, $\vec{g} \cdot \vec{b}$ analysis is required to differentiate the two. Lomer dislocations disappear in one of the $\vec{g} = \langle 220 \rangle$ conditions (namely when $\vec{g}$ is parallel to $\vec{u}$) because Lomer dislocations satisfy both of the equations above while 60° dislocations do not. 60° dislocations can only satisfy $\vec{g} \cdot \vec{b} = 0$ when $\vec{g} = \langle 220 \rangle$ but they can not satisfy the second condition, $\vec{g} \cdot (\vec{b} \times \vec{u}) = 0$. Consequently, 60° dislocations maintain a residual contrast and do not disappear for the diffraction conditions available around the (001) pole. Hence dislocations lying along a $\langle 110 \rangle$ direction that disappear in a $\vec{g} = \langle 220 \rangle$ condition are Lomer dislocations while those that do not are 60° dislocations.

In this work, InP was observed to relax via the secondary-slip system when deposited on $In_{0.36}Ga_{0.64}As$. The extent of relaxation via the secondary-slip system was a function of temperature. High strains appear to be required for semiconductors to relax via the secondary-slip system.

7.3. Results

7.3.1 Highly strained InP films

In this section we discuss the effect of temperature on dislocation morphology at the InP/$In_{0.37}Ga_{0.63}As$ interface (sample 4, 8, and 9 in Table 2). Figure 7.3 illustrates the type of misfit dislocation network that relaxed a 10 nm InP film on $In_{0.37}Ga_{0.63}As$ grown at 625 °C, the highest InP growth temperature studied (sample 9 in Table 2). The misfit dislocations that relaxed the InP film reside at the interface highlighted in Figure 7.1 between InP and the relaxed $In_{0.37}Ga_{0.63}As$ platform. As with all PVTEM micrographs in this work the [110] direction points to the top of the page for ease of comparison. The diffraction condition in which each micrograph was taken is inset within the corresponding micrograph and the diffraction condition is labeled.

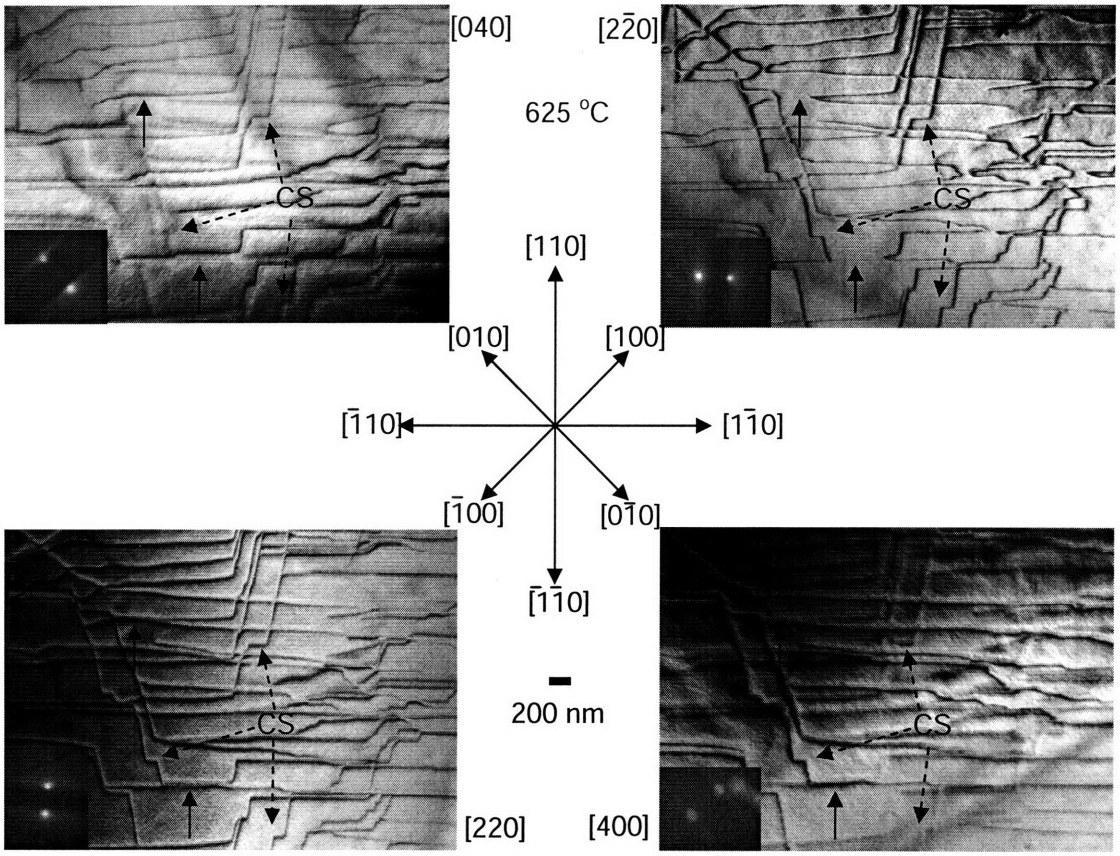

Figure 7.3: Bright-field, PVTEM $\vec{g}\cdot\vec{b}$ analysis of the dislocations that a 10 nm InP film grown at 625 °C on In$_{0.37}$Ga$_{0.63}$As induced while relaxing (sample 9 in Table 2). Care was taken to arrange all PVTEM micrographs in this paper such that the [110] direction points upward on the page, parallel to the micrograph edge. In each micrograph, the diffraction condition by which the figure was taken is displayed in the inset and the diffraction vector for each micrograph is labeled beside each micrograph. Notice that the misfit dislocations no longer lie exclusively along $\langle 110\rangle$ -type directions compared to Figure7.1(b) and that those that lie close to the [100] or [010] directions go out of contrast when $\vec{g}$ is close to parallel to the dislocation line direction. The solid arrows mark Lomer dislocations, ones that disappears in a $\vec{g}=\langle 220\rangle$. These Lomer dislocations appeared to form from the reaction of two other dislocations similar to what was described in reference [8]. Dashed arrows marked CS, for cross-slip, are kinks showing that cross-slip is present.

The morphology of the dislocations in Figure 7.3 is quite different from Figure 7.2(b). In Figure 7.2(b), misfit dislocations lie vertically and horizontally along <110>-type directions at nearly right angles. In Figure 7.3, however, the misfit dislocations appear to trace lines along the somewhat horizontal and at about 30° to the left and right of the vertical (the [110] direction). The misfit segments that are ~30° from the vertical largely disappear when $\vec{g} = \langle 0\bar{4}0 \rangle$ or $\vec{g} = \langle 400 \rangle$, depending on if the misfit line is closer to the $\langle 0\bar{1}0 \rangle$ or $\langle 100 \rangle$ direction, respectively (thus satisfying the $|\vec{g} \cdot \vec{b}| \leq \frac{1}{3}$ criterion). As with Figure 7.2, misfit dislocations lying vertically or horizontally are primarily 60°-type dislocations (not Lomer dislocations) as they do not disappear in a $\vec{g} = \langle 220 \rangle$ two beam condition. The solid arrows in Figure 7.3 point to corresponding positions in all of the micrographs and indicate the presence of a few Lomer dislocations. These Lomer dislocations appear to be formed through a dislocation reaction of two primarily 60° dislocations reminiscent of a process observed in reference[8].

The dislocations that are neither vertical nor horizontal appear to be a mixture of the primary- and secondary-slip systems enabled through cross-slip. Evidenced in Figure 7.3 by the abrupt changes in line direction, cross-slip is possible between the primary- and secondary-slip systems (see regions labeled CS for cross-slip in Figure 7.3). Further evidence for heavy cross-slip lies in the fact that the dislocations that disappear in the $\vec{g} = \langle 0\bar{4}0 \rangle$ or $\vec{g} = \langle 400 \rangle$ condition do not lie exactly along the $\langle 0\bar{1}0 \rangle$ or $\langle 100 \rangle$ direction, respectively.

While it is conceivable that these non-$\langle 110 \rangle$ directions are composed of frequent cross-slipping between the $\langle 0\bar{1}0 \rangle$ and $\langle 110 \rangle$ instead of cross-slipping between the primary- and secondary-slip systems, Bonar *et al.* performed high-resolution, weak-beam analysis and found in a similar system with similar morphology that cross-slip did not occur over small length scales in the primary-slip system[115]. In order to cross-slip, the threading dislocation must be pure screw and the Burgers vector must be shared by both slip systems. Pure screw is an expected form of the threading dislocation to minimize the Peierls stress[123].

To positively identify the slip system and verify that the secondary-slip system was active, $\vec{g}\cdot\vec{b}$ analysis and stereo microscopy were performed. Three pieces of information led to the identification of the secondary-slip system. First, since cross-slip is prevalent between the primary- and secondary-slip systems, the Burgers vector must be the same in both systems, namely $\vec{b}$ = a/2<110>. Second, stereo microscopy was performed and determined that the misfit dislocation lines lie in the (001) plane. The third piece of information needed to identify the secondary-slip system was that these dislocations disappear in a $\vec{g}=\langle 400\rangle$ or $\vec{g}=\langle 040\rangle$. With these three pieces of information, the secondary slip system can be uniquely identified. As an illustration of how to identify this slip system, examine at a dislocation that disappears in the $\vec{g}=\langle 400\rangle$ diffraction condition. Since the Burgers vector is of the form $a/2<110>$, to satisfy the $\vec{g}\cdot\vec{b}=0$ criteria the Burgers vector must be of the form $\vec{b}=a/2<011>$. To satisfy the $\vec{g}\cdot(\vec{b}\times\vec{u})=0$ criteria the line direction must be of the form $\vec{u}$ = <hkk>. However, since the line direction lies in the (001) plane, $\vec{u}$ must be of the form, $\vec{u}$ = <h00>, i.e. <100>. Because the slip plane must contain both the Burgers vector as well as the line direction, the slip plane is $(01\bar{1})$ and, in this example, the slip system is a/2[110]$(01\bar{1})$.

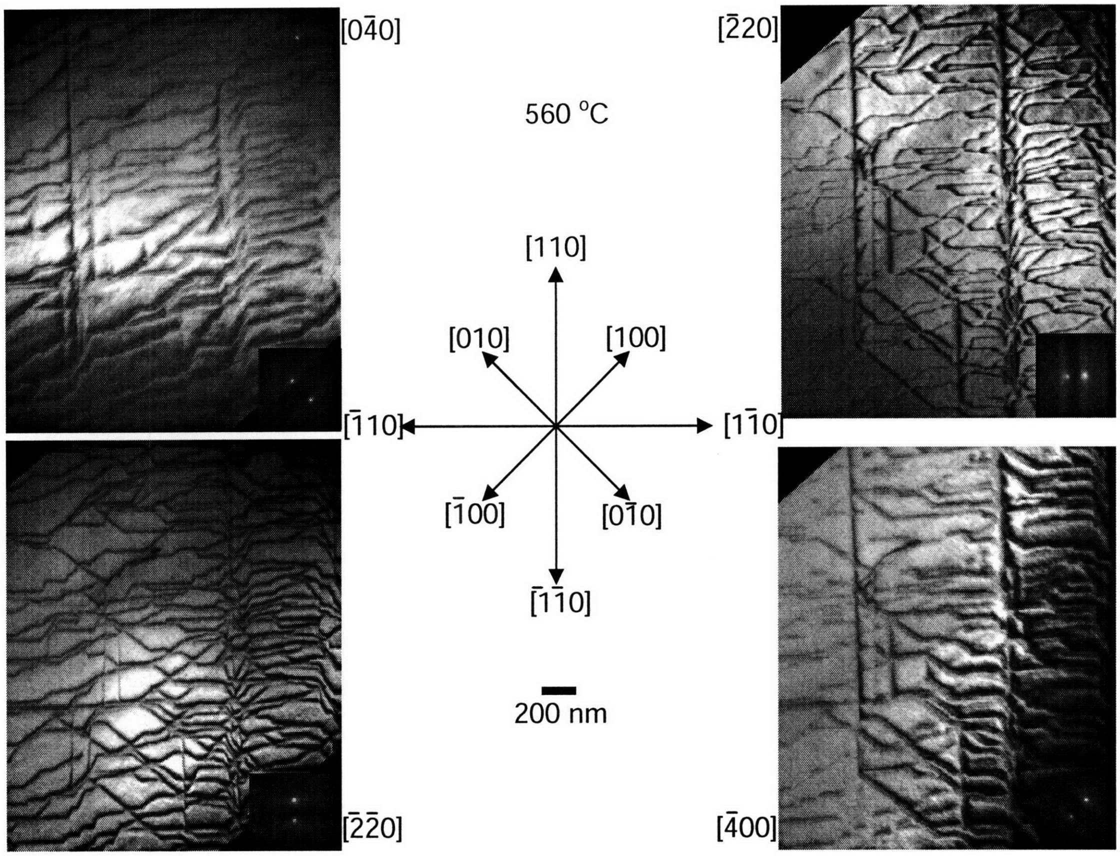

Figure 7.4. Bright-field, PVTEM, $\vec{g}\cdot\vec{b}$ analysis of the dislocations that a 14 nm InP film grown at 560 °C on $In_{0.37}Ga_{0.63}As$ induced while relaxing (sample 8 in Table 2). The secondary-slip system appears to be more active then in the case of the InP grown at 625°C seen in Figure 7.3 as there are less misfit segments lying vertically or horizontally and more dislocations disappear in the $\vec{g} = \langle 0\bar{4}0 \rangle$ or the $\vec{g} = \langle \bar{4}00 \rangle$.

The second structure (sample 8 depicted in Figure 7.4) was similar to sample 9 depicted in Figure 7.3 except the InP in sample 8 was grown at 560 °C instead of 625 °C. As all the InGaAs graded buffer platforms in this study were grown at 750 °C, the difference in this sample is in the growth temperature and thickness of the InP layer. The dislocation morphology at the InP/InGaAs interface is shown in Figure 7.4 (PVTEM $\vec{g}\cdot\vec{b}$ analysis). As is evident in comparing Figure 7.4 to Figure 7.3, more relaxation of the InP film occurred via the secondary-slip system. This is evident because more of the dislocations lose contrast in the $\vec{g} = \langle 0\bar{4}0 \rangle$ or $\vec{g} = \langle \bar{4}00 \rangle$.

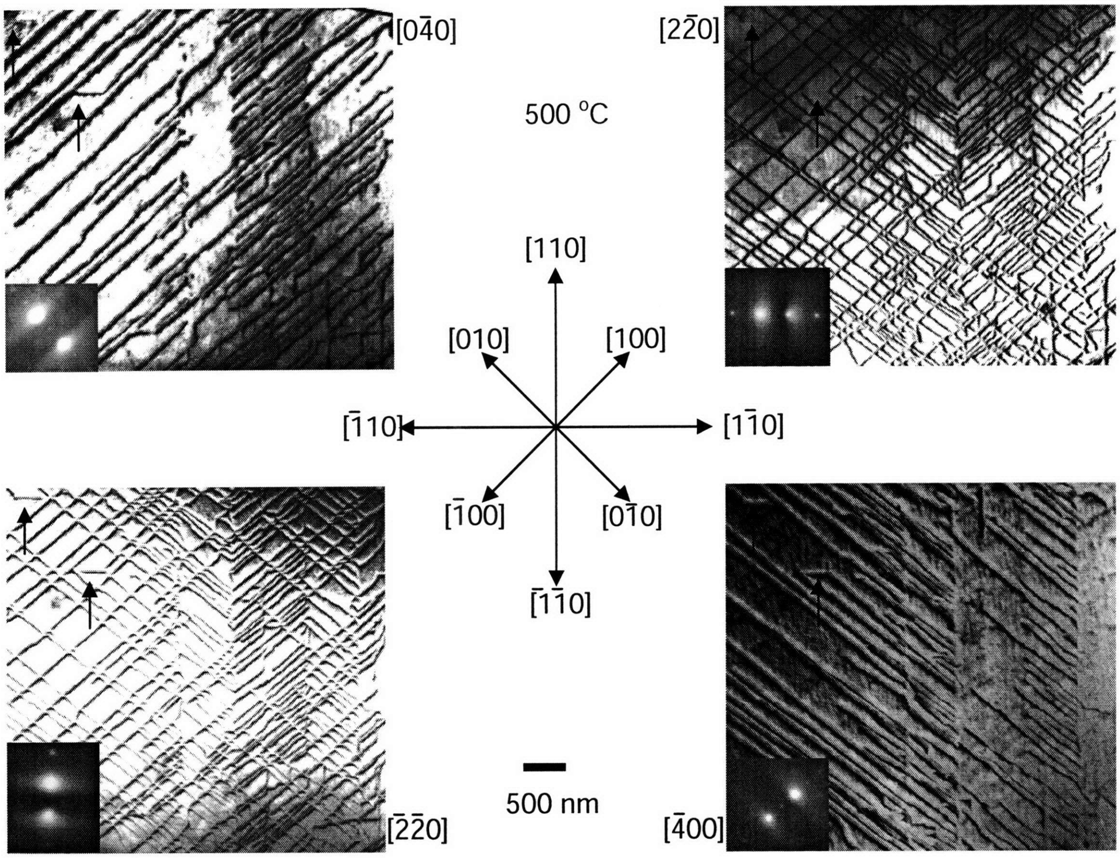

Figure 7.5. Bright-field, PVTEM $\vec{\mathbf{g}} \cdot \vec{\mathbf{b}}$ analysis of the dislocations that a 15 nm InP film grown at 500 °C on $In_{0.37}Ga_{0.63}As$ induced while relaxing (sample 4 in Table 2). As is evidenced by the micrographs, nearly all of the relaxation occurs via the secondary-slip system. This has been determined by the fact that half of the dislocations go out of contrast with the $\vec{g} = \langle 0\bar{4}0 \rangle$ and the other half when $\vec{g} = \langle \bar{4}00 \rangle$. The arrows in all of the figures highlight Lomer dislocations similar to Figure 7.3.

The third structure (sample 4), similar to the previous two samples discussed except the InP growth temperature is 500 °C, is depicted in Figure 7.5 (the plan view analysis of the InP/InGaAs interface). The relaxation of this InP film occurred almost completely via the secondary-slip system. Nearly all of the dislocations lose contrast, disappear, in either the $\vec{g} = \langle 0\bar{4}0 \rangle$ or $\vec{g} = \langle \bar{4}00 \rangle$ two-beam condition.

There are two trends seen by comparing Figures 7.3, 7.4 and 7.5 both of which lead to the conclusion that relaxation via the secondary-slip system is favored at lower temperatures. The first trend, evident by comparing Figures 7.3, 7.4, and 7.5, is that the degree of relaxation via the secondary-slip system increases as the growth temperature (T_g) of the InP film decreases. The second trend that points to increased relaxation via the secondary-slip system with decreasing T_g is that the angle between the non-<110> dislocation segments and the <110> increase and approaches 45°, on average, as the temperature is decreased. For example, the InP layer grown at 625 °C, has an average angle between the non-<110> segments and <110> direction of 16°; when the InP film is grown at 560 °C the average angle is 25°; and when InP is grown at 500 °C the average angle is 39°. As pure relaxation on the secondary slip system is 45° from the <110> direction, this trend of increasing angle towards 45° also indicates that the secondary-slip system is more active at lower temperatures.

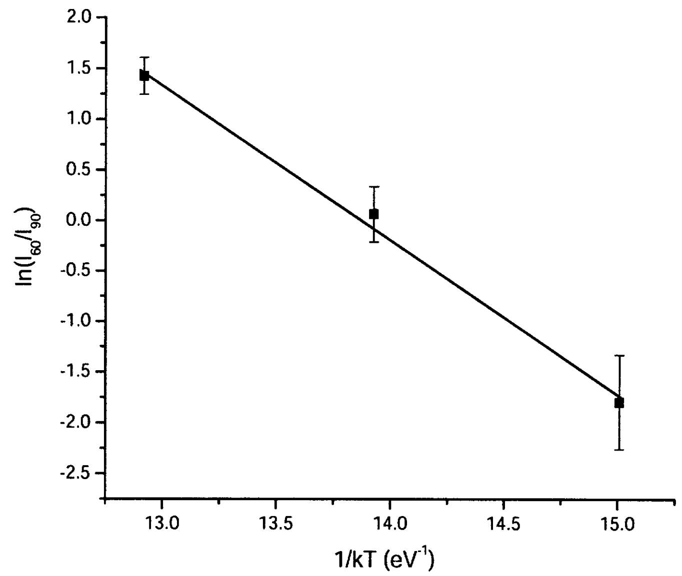

Figure 7.6 **$\ln(l_{60}/l_{90})$ [the natural logarithm of the misfit dislocation length attributed to secondary-slip system, l_{90}, divided by the misfit length attributed to the primary-slip system, l_{60}] versus 1/kT (1/eV). The three points that trace out a line whose slope is -1.5 eV represent data taken from InP grown on $In_{0.37}Ga_{0.63}As$.**

Figure 7.6 quantifies the temperature dependence of relaxation via the primary- and secondary-slip systems and plots the temperature dependence of the natural logarithm of (l_{60}/l_{90}) versus 1/kT for the three aforementioned samples. (l_{60} and l_{90} are the length of misfit dislocations observed in the interface and attributed to slip via the primary- and secondary-slip systems, respectively, while k is the Boltzmann constant and T is absolute temperature.) The ratio (l_{60}/l_{90}) follows Arrhenius-type dependence. The dislocation line length is related to the kinetics of the dislocation relaxation process. There are two main components of the kinetics in these systems: dislocation nucleation and dislocation glide. If dislocation nucleation is easy, then the dislocation length is only related to the velocity of the threading dislocations as they relax the material. In this material system, dislocation nucleation was found to be easy.

Frequent dislocation nucleation along $\langle 110 \rangle$-type directions in some regions was observed in samples 2-4, and 7-10 (Table 2) and is evident in Figure 7.4, Figure 7.5, and Figure 7.7. These dislocation nucleation events occur along $\langle 110 \rangle$-type directions and lie in patterns reminiscent of the "cross-hatch" pattern typically observed on relaxed mismatched films. The cross-hatch pattern is a direct consequence of misfit dislocation strain fields[71]. Trenches in the cross-hatch pattern are under compression and ridges in tension[71], and one would expect that dislocations would nucleate first in the trenches because the compressive strain there is the sum of the global compressive strain plus that of the local strain due to the underlying misfit dislocation network. In addition to the added compressive strain associated with the trenches, Cullis *et al.* have demonstrated that trenches provide easy nucleation sources for dislocations[124]. Consequently, we find in the InP/InGaAs structures that dislocation nucleation is easy, and therefore dislocation glide is likely dominating the dislocation morphology at the interface.

Figure 7.7: BF, $\vec{g} = \langle 220 \rangle$, PVTEM of Sample 3 in Table 2. Notice that prolific dislocation nucleation along <110>-type directions.

Thus, the interface dislocation length is directly related to the dislocation velocity, consequently $l_{60}/l_{90} \propto v_{60}/v_{90}$ (where v_{60} and v_{90} are the dislocation velocities of the primary- and secondary-slip systems respectively). Phenomenologically, the observed dislocation velocity, v_{sat}, has been seen to obey the semi-empirical equation dependant on strain, ε, to the power, m, and temperature given below[36, 37].

$$v_{sat} = C\varepsilon^{m} e^{(-E_a/kT)}$$ **Equation 21**

In this equation, C is a fitting parameter, and E_a is the activation energy. From this expression it may be possible to reproduce Figure 7.6 since, roughly speaking, the dislocation length should be proportional to the velocity. We can assume then that the quantity (l_{60}/l_{90}) graphed in Figure 7.6 is proportional to a ratio of exponentials containing the activation energy for dislocation glide in each of the two systems. Thus, $\ln(l_{60}/l_{90})$ is proportional to the difference in activation energy between the two glide systems. From Figure 7.6, we calculated the activation energy of the primary-slip system is larger then the secondary by 1.5 eV, and therefore the glide activation energy for the secondary-slip system in InP is around 0.1eV (1.6 eV is the activation energy for dislocation glide in InP[125]).

Many of the previous figures (Figures 7.3-7.6) document the change in relaxation morphology as a function of the InP growth temperature. Figure 7.8 shows the relaxation morphology of the InP film at different thicknesses and strains. Sample 4 and 6 show the trend at thin and intermediate thickness, whereas we reinsert in the third micrograph from Figure 7.1 to remind the reader of the dislocation morphology of InP, where the strain in the film is low. All three micrographs in Figure 7.8 are of the same scale and rotated such that the <110> direction points upward. In the first micrograph on the left (sample 4 in Table 2), the InP film grown at 500 °C relaxes almost completely via the secondary-slip system. The micrograph in the center (sample 6 in Table 2) was also grown at 500 °C but is thicker than the InP film in sample 4. Sample 6 is seen to relax via the primary- and the secondary-slip systems evidenced by both sets of misfit dislocation lines running along the <110>- and <100>-type line directions, respectively. Unlike in previous examples where cross-slip was evident both the primary- and secondary-slip systems were active together, the morphology in sample 6 suggests instead suggests that the primary- and secondary-slip systems were active at different times. The final micrograph on the right is from the sample depicted in Figure 7.2. This InP sample represents the type of deformation expected when the film is relatively thick and most of the strain has been relieved.

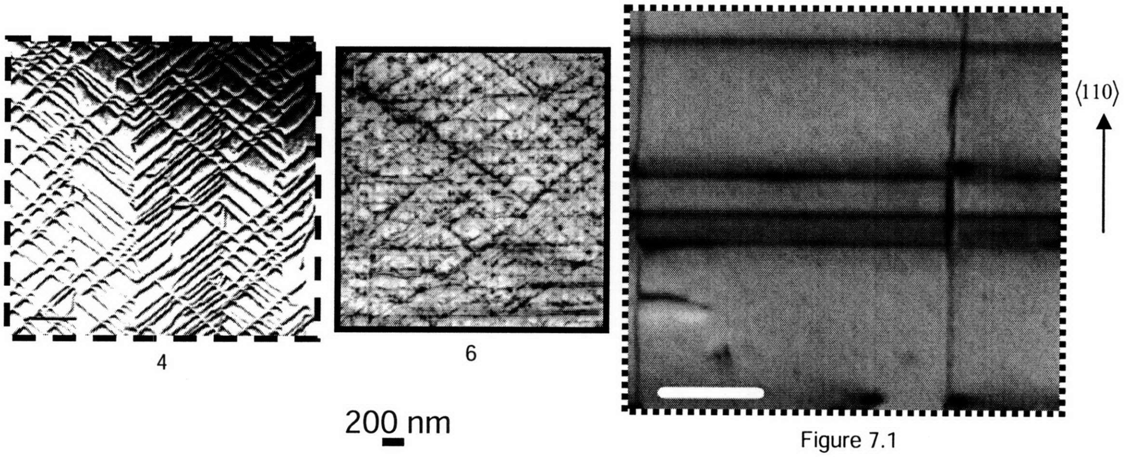

Figure 7.8: BF, $\vec{g}=\langle 220\rangle$, PVTEM micrographs of three samples showing three different relaxation morphologies of InP films. The <110> direction points upward in all three figures and all three figures are to the same scale. The micrograph on the left is from sample 4 in Table 2 grown at 500 °C and displays relaxation almost completely via secondary-slip system. The micrograph in the middle (sample 6 in Table 2) is also grown at 500 °C but the InP layer is a greater thickness, and there is relaxation via the secondary-slip system and the primary-slip system. The micrograph on the right, from Figure 7.2, shows relaxation via the primary-slip system. The borders around each micrograph correspond to the three different paths or relaxation indicated in Figure 7.9.

The microstructures in Figure 7.8 are consistent with the concept of a critical strain, ε_c, requirement for a film to relax via the secondary-slip system. Figure 7.9 schematically displays a possible evolution of strain and relaxation as a function of InP film thickness. Path 1 is taken by sample 4 where ε_c has been exceeded and the relaxation during the film growth terminates before the strain falls below ε_c. Since the strain level remains above ε_c all the relaxation in sample 4 occurs via the secondary-slip system. Path 2 initially follows the same relaxation path taken by sample 4 yielding secondary-slip dislocations. However, as the film thickness is increased, the InP continues to relax until eventually the remaining elastic strain in the InP film is less than ε_c. As a result, further relaxation occurring when $\varepsilon < \varepsilon_c$ is accomplished via only the primary-slip system. This mechanism describes how the InP film would relax via both the primary- and secondary-slip systems at different times as seen in the microstructure of sample 6 in Figure 7.8. Finally the low strain case, depicted by the right-most micrograph in Figure 7.8, corresponds to path 3 in Figure 7.9. Because of the low strain state, the critical thickness for the film is much larger, and the strain in the film is always below ε_c. Therefore, the InP film relaxes via the primary-slip system only. The trend seen in path 2 of Figure 7.9 was observed in InP films grown at 560 °C and 625 °C as well, though more cross-slip present at these temperatures are super-imposed making identification of two-stage relaxation more difficult.

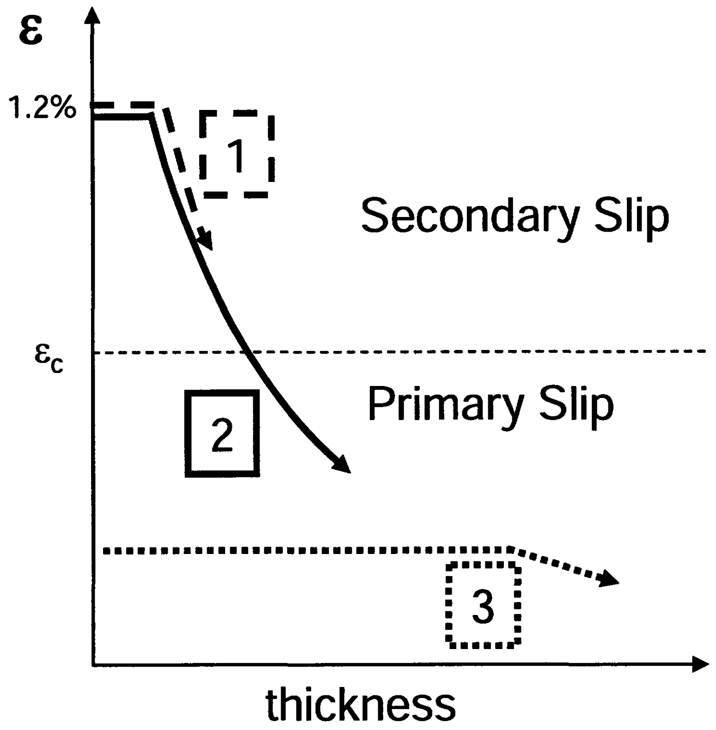

Figure 7.9: Schematic of relaxation process of the three InP films in Figure 7.8 illustrating the possibility of a critical strain associated with relaxation via the secondary-slip system. Two of these InP films (samples 4 and 6 in Table 2) start with high strains above the critical strain, ε_c, and the third film starts with low strain (depicted in Figure 7.2). These three samples take three paths to relax as the film grows. The three paths correspond to three microstructures. Relaxation via the first path (taken by sample 4) shows that all relaxation was done at high strains and as a result relaxation occurred only via the secondary-slip system. The second path started at high strains however, as the film relaxes the strain reduces below ε_c and relaxation via the primary-slip system occurred. Relaxation via the third path, taken by the sample depicted in Figure 7.2 occurred at low strains and, as a result, only 60° dislocations are present.

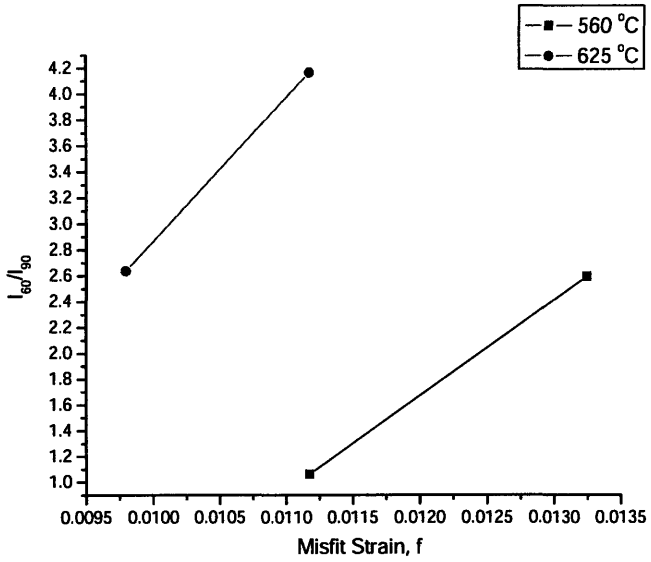

Figure 7.10: l_{60}/l_{90} versus misfit strain for InP grown at 560 °C and 625 °C. Though there are only two points for each temperature, the trend for each temperature is the same: namely that as the misfit strain increases, relaxation via the primary-slip system increases as well.

Unlike with Figure 7.6 which plots the natural log of l_{60}/l_{90}, Figure 7.10 plots the ratio of l_{60}/l_{90} and the small effects of misfit strain on this ratio. The trend apparent in Figure 7.10 is that once the critical strain has been surpassed and the secondary-slip system is enabled, as the strain is increased, relaxation via 60° dislocations is favored. This is evident at both 560 °C and at 625 °C. While there are only two points per temperature, the trend is consistent across the two temperatures. This phenomenon may also be explained by Equation 21, where there is also a dependency of the velocity on strain to the power m. This fitting parameter for 60° dislocations is m_{60}, if m_{60} is larger then m_{90} then one might be able to explain the results that 60° dislocations appear to be favored at higher strains evidenced in Figure 7.10.

Figure 7.11 plots the elastic strain remaining (ε) vs. the thickness (h) of samples 1-10 (InP films with T_g = 500, 560, and 625 °C on graded buffers with final composition close to $In_{0.36}Ga_{0.64}As$). The elastic strain remaining (ε) was determined by measuring the length of misfit dislocations from PVTEM micrographs over large areas and calculating the plastic deformation (δ) that occurred taking into account that the secondary-slip system has a larger effective Burgers vector. That plastic deformation (δ), was then subtracted from the lattice-mismatch (f) between the InGaAs platform and the InP to find ε according to the following relation.

$$\varepsilon = f - \delta \qquad \textbf{Equation 22}$$

The actual composition of the InGaAs platform varied slightly with each sample. This composition difference was taken into account as well in determining ε.

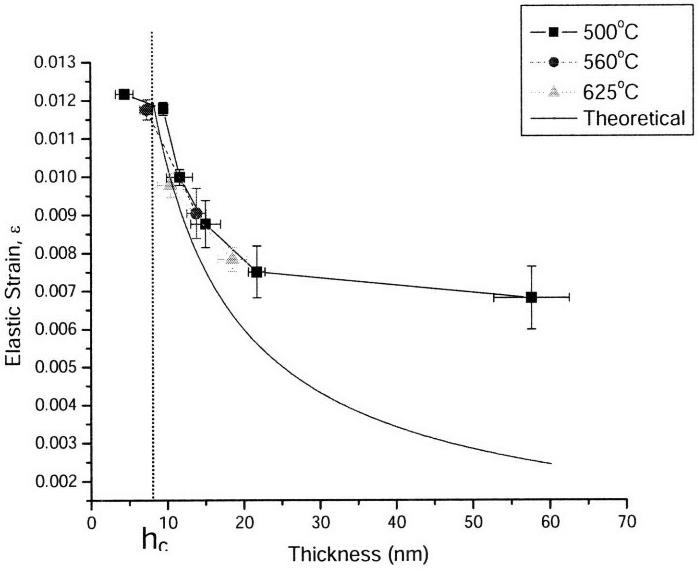

Figure 7.11. Elastic Strain vs. Thickness for InP films deposited on ~$In_{0.36}Ga_{0.64}As$ at 500°C, 560°C, and 625°C. The curve without error bars is the theoretical elastic strain vs. thickness calculated using an equation derived similarly to Matthews *et al.* in [6] and modified by Fitzgerald in [7] for dislocations in the primary-slip system.

In addition to the experimental data plotted, Figure 7.11 includes a theoretical curve based on the work of Matthews *et al*[6] and modified by Fitzgerald[7] for primary-slip dislocations. The theoretical curve in Figure 7.11 is plotted using the following equation.

$$\varepsilon = \frac{D(1-\nu\cos^2\alpha)[\ln(h_c/b_{eff})+1]}{Yh_c}$$ **Equation 23**

where ν is the Poisson ratio, α is the angle between $\vec{b}$ and $\vec{u}$, b_{eff} is the effective Burgers vector that accommodates the lattice-mismatch (f), Y is the Young's Modulus and D is an average shear modulus. Y and D are given by the equations below for (001) substrates

$$Y = C_{11} + C_{12} - 2\frac{C_{12}^2}{C_{11}}$$ **Equation 24**

$$D = G_f G_s b/\pi\ (G_f + G_s)(1 - \nu)$$ **Equation 25**

where C_{ij} are the elastic constants and G_f and G_s are the shear moduli of the film and substrate respectively. (The "substrate" in this case is the relaxed $In_xGa_{1-x}As$ platform upon which the InP is grown.)

The elastic strain remaining, ε, does not appear to be a function of temperature or methodology of relaxation as ε apparently follows a universal curve as a function of thickness at all three temperatures. This curve follows the calculated curve based on Equation 23 for 60° dislocations for thicknesses close to the critical thickness, h_c, where the relaxation rate is large. As the thickness increases, however, the theoretical curve predicts a greater degree of relaxation compared to relaxation measured in samples 1-10. This discrepancy in relaxation has been observed by Matthews *et al.*[44], Dunstan *et al.*[126], and Krishnamoorthy *et al.*[127] and has been attributed to work hardening (dislocation interactions) by the former two. Freund has proposed a mechanism for work-hardening in which dislocations arrest other dislocations because of the dislocation strain fields[43].

7.3.2 Highly strained InGaAs films

We have shown a mismatch, temperature, and thickness dependence on the interface dislocation morphology. In this section, we describe our experiments to test whether InP or InGaAs lattice-matched to InP has an influence on the dislocation morphology (i.e. to test if the film material has a large influence on the deformation). InGaAs lattice-matched to InP was substituted for InP, and the interface between $In_{0.53}Ga_{0.47}As$ on $In_{0.35}Ga_{0.65}As$ was also investigated. In a similar manner to growing InP on ~$In_{0.36}Ga_{0.64}As$ (as was done in samples 1-10), 15.2 nm of $In_{0.53}Ga_{0.47}As$ was grown on $In_{0.35}Ga_{0.65}As$ at 500 °C (sample 11 in Table 2). Figure 7.12 shows the bright-field PVTEM micrographs from the relaxation of this $In_{0.53}Ga_{0.47}As$ film. The morphology of the misfit dislocations depicts a mixture of primary- and secondary-slip dislocations with a few Lomer dislocations, as in Figure 7.3 and Figure 7.5. (The Lomer dislocations are marked by arrows in Figure 7.12.) Similar to the case with InP on $In_{0.37}Ga_{0.63}As$, the Lomer dislocations look to be the product of dislocation interactions. The microstructure of sample 11 is somewhat reminiscent to that of sample 9 (the InP film grown at 625 °C) as the dislocations that disappear are about 30° from the vertical in both samples. Thus, it is possible that $In_{0.53}Ga_{0.47}As$ at 500 °C may behave mechanically like InP at 625 °C, producing similar dislocation morphologies. The data also indicates that the activation of the secondary-slip system is not peculiar to InP.

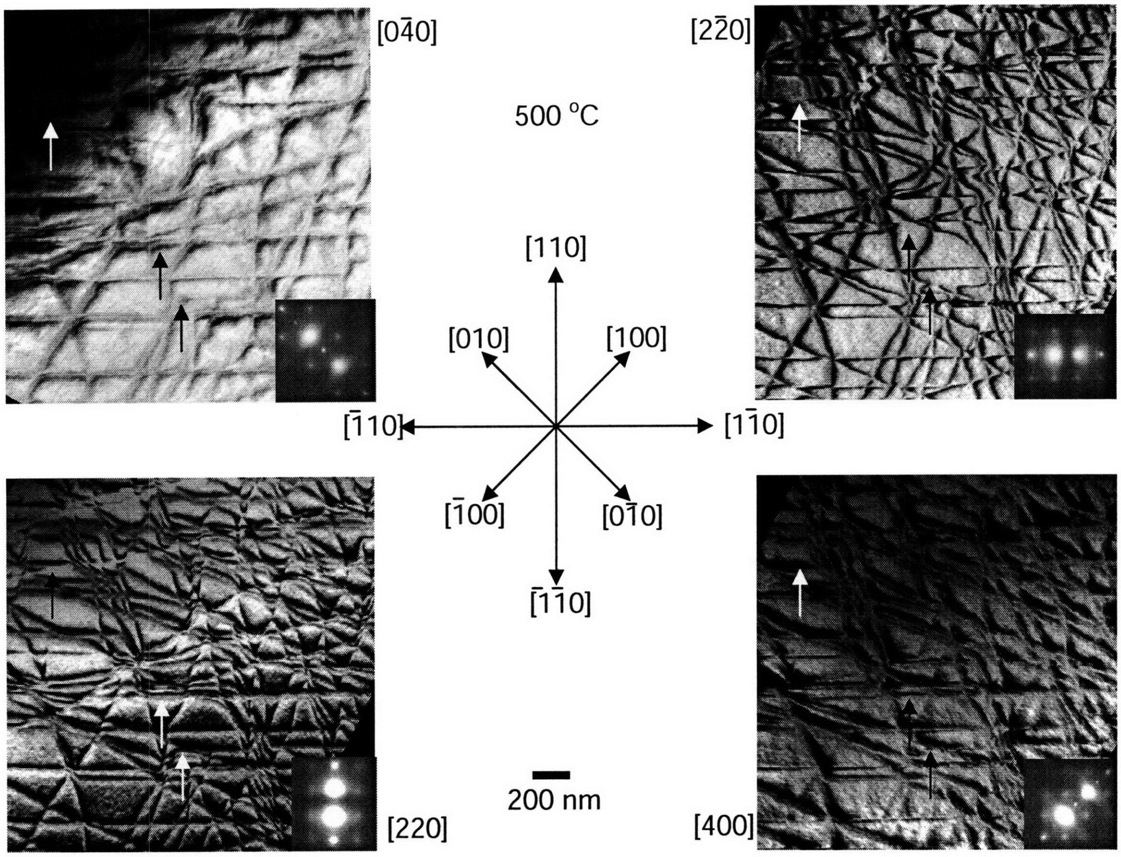

Figure 7.12: Bright-field, PVTEM micrographs of sample 11 under different diffraction conditions. The structure of sample 11 consists of a 15.2 nm of $In_{0.53}Ga_{0.47}As$ film on an $In_{0.35}Ga_{0.65}As$ graded buffer. The $In_{0.53}Ga_{0.47}As$ film was grown at 500 °C. Relaxation of the final $In_{0.53}Ga_{0.47}As$ appears to be a combination of primary and secondary-slip systems. The microstructure is somewhat reminiscent of InP grown at 625 °C. The arrows in the figure mark Lomer dislocations that disappear in the $\vec{g} = \langle 2\bar{2}0 \rangle$.

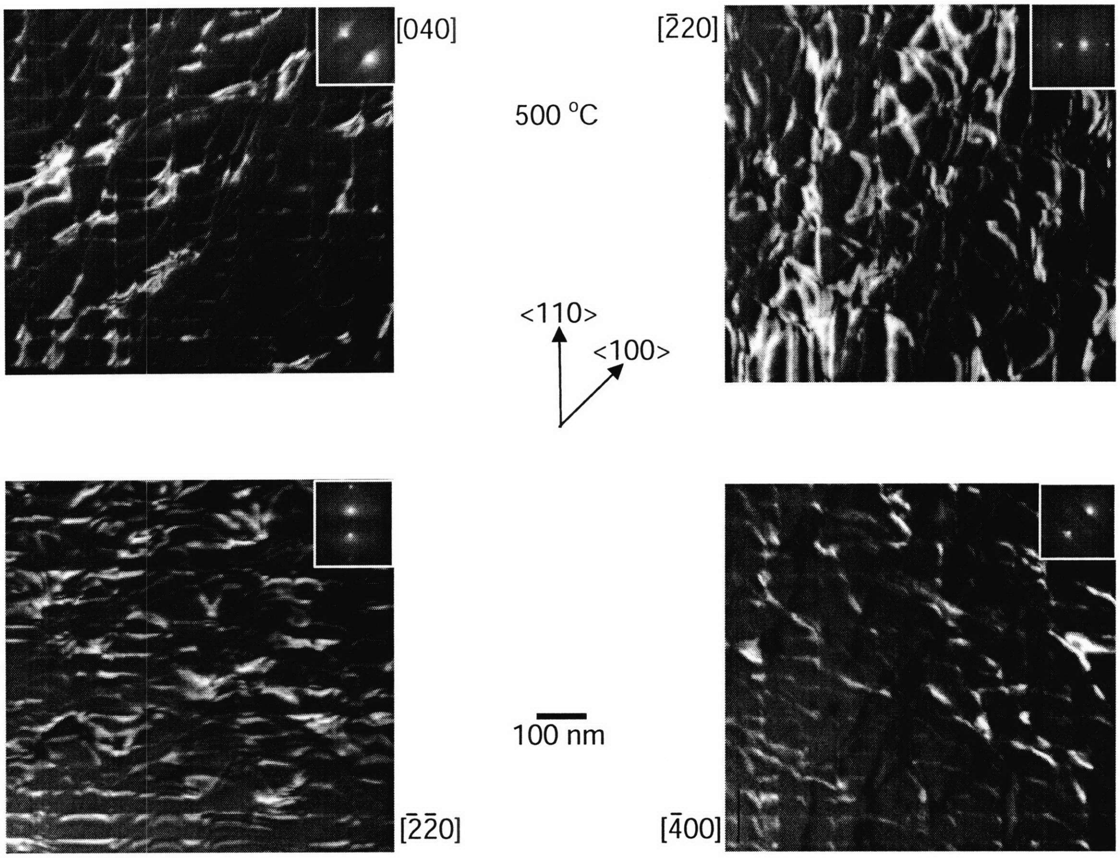

Figure 7.13: Weak-Beam, dark-field, PVTEM micrographs of 12.1 nm of $In_{0.4}Ga_{0.6}As$ on $In_{0.1}Ga_{0.9}As$ grown at 500 °C (sample 12) under different diffraction conditions. These micrographs display more Lomer dislocations that do not appear to be the result of dislocation interactions, unlike those seen in earlier figures.

As high strains enable the secondary-slip system, even higher strains were examined in the InGaAs system to determine if there were any further changes in dislocation morphology. A higher strained film, $In_{0.4}Ga_{0.6}As$ (f=2.1%) 12.1 nm thick, on a graded buffer whose final composition was $In_{0.1}Ga_{0.9}As$ is shown in Figure 7.13. (Weak-beam, dark-field, PVTEM was used to minimize the contrast from moiré fringes; consequently, dislocations appear as white lines.) Unlike all of the other PVTEM images whose lattice-mismatch was $f \approx 1.2\%$ (e.g. InP or $In_{0.53}Ga_{0.47}As$ on $In_{0.36}Ga_{0.64}As$), $In_{0.4}Ga_{0.6}As$ on $In_{0.1}Ga_{0.9}As$ displays a higher density of Lomer dislocations (horizontal or vertical dislocations that disappear in $\vec{g} = \langle \bar{2}20 \rangle$ or $\vec{g} = \langle \bar{2}\bar{2}0 \rangle$ two-beam condition, respectively). The Lomer dislocations in Figure 7.13 are not the product of dislocation reactions, but typically form in high-mismatched systems during pre-coalescence island growth. Thus, at large enough strain, this system behaves as a typical high-mismatched semiconductor interface.

7.4. Discussion and Summary

7.4.1 Discussion of the Secondary-Slip System

A significant lattice-mismatch strain is required for the semiconductors to relax via the secondary-slip system[108-119]. At low lattice-mismatches, the primary-slip system appears to be the only system of relaxation on the (001) axis. Even at large stresses, the primary-slip system appears to be active[108-119]. We observe that at larger strains above a critical strain, a secondary-slip system is activated in addition to the primary. High T_g the primary-slip system is still favored while low T_g favors secondary-slip. Albrecht *et al.* have calculated that for particular threading dislocation configurations there is a critical strain at which the primary-slip system is favored over the secondary-slip system[109].

Others have observed the secondary-slip system in semiconductors [108-119] and some have suggested that climb is the mechanism for secondary slip[116, 128]. However, the data in this work shows that relaxation via the secondary-slip system increases as the growth temperature decreases. For this reason, as climb is a thermally activated process requiring point defects, and also for the fact that these secondary-slip dislocations move at 3 μm/s at 450°C and at 10-30 μm/s at 690°C in InGaAs [109, 129] glide appears to be the mechanism for relaxation via the secondary-slip system.

Figure 7.14 summarizes the trends associated with relaxation via the secondary-slip system in this work. The secondary-slip system becomes active only at large lattice-mismatch. However, large lattice-mismatch is not the only variable that affects relaxation via the secondary-slip system. The temperature at which the film relaxes also affects the activation of the secondary-slip system (see Figures 7.3, 7.4, and 7.5).

Many growth conditions result in a dislocation morphology that suggests activation of both slip systems simultaneously. Due to this observation and because dislocation nucleation is relatively easy, the dislocation velocity in the two systems determines the extent to which relaxation occurs via the secondary-slip system at the cost of the extent of relaxation via the primary-slip system. This explanation is similar to the explanation for the predominance of the α or β dislocation over β or α dislocations, respectively, in the zinc-blende crystal system where the dislocation glide velocities for α and β dislocations are different. Also, Nabarro has suggested that when dislocations are formed through plastic deformation, those dislocations present are the ones that have the highest glide velocity[123]. Consequently, when applying this framework to the primary- versus secondary-slip systems, the implication is that at high strains and low temperatures the glide velocity of the secondary-slip system is higher than the 60° dislocation glide velocity and as the growth temperature is increased the velocity of the primary-slip system increases at a greater rate.

	Low T_g	High T_g
High ε	Primarily 90°	Mixed
Low ε	60°	60°

Figure 7.14: Schematic displaying the influence of stress and temperature on the dislocation morphology in relaxed semiconductor films grown on the (001) axis. At low stresses, the primary-slip system, associated with 60° dislocations, is active. However, for higher stresses, the secondary-slip system, associated with 90° dislocations, becomes active and is favored at high-stress and low temperature.

7.4.2 Mechanisms for Secondary-Slip

We note that cross-slip is present at high strains for all temperatures and cross-slip requires that the two slip-systems have the same Burgers vector. 60° dislocations are known to be dissociated into partial dislocations in semiconductors as they glide on the glide-set planes, as opposed to the shuffle-set planes[9, 10, 130]. The distance between partials (i.e. the length of the stacking fault) is related to the degree of compression in these (001) structures. The higher the compressive stress, the closer the partials are. It is reasonable to assume that a large distance between partials would decrease the chance for cross-slip. Higher compressive strains should bring the two partial dislocations closer together, enabling cross-slip onto the secondary-slip planes. Thus, high strains probably allow threading dislocations to more easily cross-slip and pursue the secondary-slip system. In this way, the ε_c may be the strain at which the partial dislocation are close enough to allow for cross-slip onto the secondary-slip system and would imply that dislocations that nucleate are 60° dislocations and, for sufficient strains, may cross-slip onto the secondary-slip system. (It should be noted that higher strains may also enable 60° dislocations to relax via the shuffle-set where partial dislocations are energetically unfavorable[11] which would also enable cross-slip.)

Once a high strain is achieved and dislocations glide via both the primary- and secondary-slip systems there is a dependence on temperature in the amount of relaxation observed via each slip system. Based on the experimental data, we are forced to conclude that dislocation velocity for the dislocation in the secondary-slip system are higher then that in the primary at high-strains and at low temperatures.

7.5. Conclusion

In InP/InGaAs and InGaAs/InGaAs systems, we have observed that InP and InGaAs layers relax in three possible regimes which depend on the strain state and the growth temperature of the film. Typically low-mismatch and high-mismatch regimes are reported, whereas we have explored an in-between regime in which a secondary-slip system is activated. In the low-mismatch regime, relaxation of the film occurs via the primary-slip system with 60° dislocations gliding on {111}-type planes. For intermediate lattice-mismatches, the film relaxes via the primary- and secondary-slip systems with dislocations gliding on {111}- and {110}-type planes respectively. The amount of relaxation that occurs via the secondary-slip system is a function of temperature with low temperatures favoring the secondary-slip system. In the high-mismatch regime, Lomer edge dislocations form during coalescence of islands as the film grows and covers the surface[131]. The larger the mismatch, the more efficient the dislocation type is at relieving the lattice-mismatch stress as 90° dislocations are more efficient then 60° dislocations and Lomer dislocations are the most efficient as their whole Burgers vector is in the (100) plane.

In the intermediate-strain, mixed-slip-system regime, the difference in the amount of relaxation via the primary- and secondary-slip systems as a function of temperature is explained by the semiempirical expression for dislocation velocity which is a thermally activated process. We can, therefore, explain the Arrhenius dependence observed in the ratio of l_{60}/l_{90} (in Figure 7.6) as well as the strain dependence on l_{60}/l_{90} (in Figure 7.10). We conclude that under high-strain conditions, the 90° dislocation glide has an activation energy 1.5 eV lower than that of 60° dislocation glide.

In this work the use of graded buffers enabled the selection of an arbitrary strain state for compressing InP. The methodology of using graded buffers to induce arbitrary strain in a material may allow more controlled stress-strain experiments in materials. One of the limitations to the traditional deformation methodology to study stress-strain curves, like tensile tests, was that the strain state in the materials could not be completely controlled or reproduced. By using graded buffers, however, an arbitrary stress can be achieved reproducibly.

Chapter 8. Summary of Results and Future Work

8.1. Summary of Results

8.1.1 InP on GaAs

In this work phase separation was seen in InGaAs, InGaP and probably $In_x(Al_yGa_{1-y})_{1-x}As$. This phase separation took the form of Ga-enriched regions within an otherwise compressively strained matrix. In this way the Ga-enrichment acted as a mode of plastic deformation reducing the compressive strain in the film. By studying the evolution of microstructure in a layer grown under the same growth conditions as a function of thickness, surface diffusion was shown to be the mechanism by which phase separation occurred. Within this layer, the fact that the microstructure changed as the film was grown suggested that the underlying strain fields on the surface affected the morphology of the phase separation in the growing film. In addition, strain fields associated with the misfit dislocation network along <110>-type directions were attributed to the phase separation forming along <110>-type directions. Analysis of AFM, PVTEM, and XTEM micrographs established a correlation between trenches and phase separation. In cross-hatched regions, trenches are associated with regions under compression, as the growth rate of compressive films is less then that of regions under tension[72]. The fact that the phase separation morphology changed with thickness and that phase separation starts in trenches point to a consistent picture that stress affects phase separation.

The evolution of the morphology of phase separation in graded buffers, for example in the InGaAs system develops in the following way: as the In content increases, the compressive stress associated with some regions appears to build up. Initially the phase separation develops in compressive regions following <110>-type directions associated with the cross-hatch pattern and then, as the In content increases, the phase separation spreads over into the tensile regions, where phase separation was initially suppressed. The phase separation may be suppressed in the tensile regions for some In contents; however, with enough In present, phase separation can still occur there. This evolution is shown in Figure 8.1 where initially, as in Figure 8.1(a), phase separation is well confined to <110>-type directions that could be associated with compressive regions in $In_{0.31}Ga_{0.69}As$. However, as the In content is increased to $In_{0.35}Ga_{0.65}As$, the phase separated regions expand. Understanding that phase separation was controlled by surface diffusion allowed us to speculate ways to influence the kinetic mechanism to reduce phase separation including increasing the growth rate and decreasing the surface diffusion.

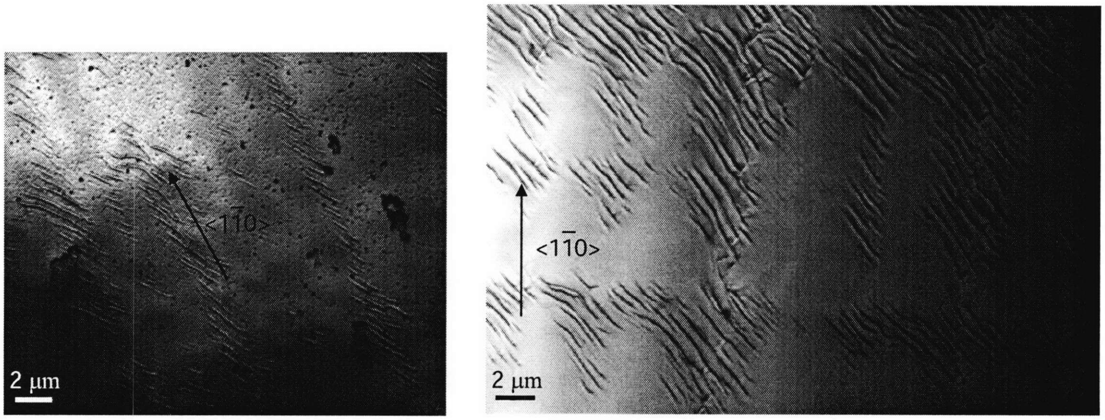

a

b

Figure 8.1 Bright-field, g=<220>, PVTEM micrographs of InGaAs out to a final composition $In_{0.31}Ga_{0.69}As$ (a), and $In_{0.35}Ga_{0.65}As$ (b) on 2° offcut GaAs substrates.

Understanding phase separation led to our success in suppressing it and enabling high-quality, low threading dislocation density, materials. We were able to achieve low

ρ_t (ρ_t=1.2x10^6/cm^2) In$_{0.34}$Ga$_{0.66}$As by growing the InGaAs graded buffers at 725 °C. This InGaAs was then used as a platform to enable high-quality InP on GaAs by using an InGaP graded buffer grown at 700 °C on top of the InGaAs platform. The quality of this InP on GaAs was then compared to bulk InP using by growing a PL structure on each. The PL results indicated that the quality of the InP on GaAs using the hybrid InGaAs and InGaP graded buffer was of comparable quality to the bulk InP since the ratio of the integrated intensities ratio was near unity and was not a strong function of temperature. These promising results suggest that minority carrier devices could be fabricated on top of this hybrid InGaAs to InGaP graded buffer. Since the operations of minority carrier devices are the most susceptible to defects, all devices should be able to use this high-quality InP on GaAs.

8.1.2 Dislocation Study

In examining InP with 1.3% compressive strain a secondary-slip system was activated. This secondary-slip system allowed dislocations to glide on <110>-type planes. A critical strain was required to activate this secondary-slip system as usually the primary-slip system, with dislocations gliding along {111} planes, is observed. At high strains when the secondary-slip is active, both the primary- and secondary-slip systems are active. When both systems are active, the secondary-slip system appears to be favored at lower temperatures with cross-slip being apparent between the two systems at all temperatures studied. Cross-slip was observed and implies that the threading dislocations are pure screw and that the Burgers vector is shared by the two slip systems. Usually, in semiconductors, the primary-slip system glides using the glide-set-type glide plane which allows dislocations to separate into partials. Dislocations that have separated into partials would not be able to cross-slip onto the secondary-slip system, however. Therefore, the larger compressive stress may compress the two partial dislocations in the glide-set sufficiently that it behaves as if it was a not separated into partial dislocations to allow cross-slip onto the secondary-slip system. The critical strain may then be the strain required to move the partial dislocation close enough to enable cross-slip.

Semiconductor materials seem to relax using three different dislocation systems at different strain states. At low strains, the primary slip system is active, at medium strains both the primary- and the secondary-slip systems are active and at high strains Lomer dislocations are present. Interestingly as the strain increases the dislocations by which the material relaxes becomes more efficient at relaxing the strain as 90^o dislocations relieve about 40% more strain then 60^o dislocations and Lomer dislocations relieve about 40% more strain then 90^o dislocations.

The original purpose of exploring this highly strained InP on InGaAs was to determine if high-quality InP on GaAs could be achieved through controlled relaxation of InP on the InGaAs platform. This study determined that many dislocation nucleation events occurred to relax the highly strained InP. These nucleation events greatly increased the threading dislocation density making high-quality InP on GaAs unachievable via this route.

8.2. Future Work

8.2.1 Graded Buffers

The most obvious future work for the high-quality InP on GaAs using the hybrid graded buffer would be to demonstrate a laser on this structure and compare it to one grown on bulk InP. This would be the ultimate result that was not yet attempted and would prove that high-quality materials for any device was achieved since lasers are the most particular devices, requiring the highest quality material. Another route for future work would be to grow still larger lattice constant materials beyond InP perhaps using InGaAs, InAsP, or using some Sb.

As mentioned in the introduction, incorporating high-quality InP on Si would be a worthy goal and would enable access to state-of-the-art transistors on the Si platform. As high-quality GaAs on Si has been demonstrated by Groenert *et al.* through the demonstration of a room temperature laser using a SiGe graded buffer[30, 31], this GaAs on Si platform on which the hybrid InGaAs and InGaP graded buffers could be grown may enable high-quality InP onto Si. In this way 300 mm InP on Si may be achieved; however, accomplishing this goal would be far from trivial for a number of reasons.

The first issue to overcome to achieve high-quality InP on Si is the issue of offcut substrates. As is seen in this work, offcut samples phase separate earlier than those that are on axis. Offcut substrates, however, are required to grow GaAs that is free of anti-phase boundaries (APBs) on Ge[132]. While using offcut substrates to avoide APBs, avoiding phase separation in the hybrid InGaAs and InGaP graded buffers may be accomplished using the high temperature InGaP materials system more and the InGaAs system less. A high-temperature (700 °C) InGaP graded buffer that was miscalibrated and had more Ga then expected seemed to show no signs of phase separation in spite of being richer in Ga. For this reason the composition window to avoid phase separation in

InGaP may be large enough to avoid phase separation and grow the graded buffer on an offcut substrate.

The second issue that would need to be overcome to have high-quality InP on Si may not be as easy to solve as the offcut substrate issue and lies is the differences between coefficients of thermal expansion. Differences in the coefficients of thermal expansion limit the thickness of heteroepitaxial thin films typically to thicknesses of about 10 μm. Thicker films will often lead to cracking or delamination. As a consequence, the Fitzgerald group has done some work to remove the graded buffer in the SiGe materials system to bring Ge directly onto Si. This is done by bonding the final Ge film on the graded buffer to a host substrate and then removing the initial growth substrate. Pitera and Isaacson have done some work on this; and have both had difficulties in achieving their results[133, 134].

The results of this work are very promising in enabling graded buffers in other materials systems when vertical strain contrast associated with phase separation is seen as well. When phase separation is observed, this work suggests going to higher temperatures and attempting to grow the required lattice constants using different materials systems (preferably those close to the pure binary component) to avoid phase separation. The path to achieve high-quality graded buffers in softer materials (like in the antimonides) may be lie in their growth at lower temperatures, well below the critical temperature in the diffusion limited regime of the TTT diagram. Growth at low temperatures in these softer materials may be possible because the dislocation glide velocities at these temperatures in these soft materials may be high enough to ensure low dislocation densities and surface diffusion may be sufficiently suppressed to avoid phase separation.

8.2.2 Dislocation Study

Looking at the bigger picture from the results of the InP with 1.3% compressive strain suggests a new way to conduct deformation studies using lattice-mismatched materials, as opposed to the traditional tensile-type tests. Unlike with the traditional methods, like tensile tests, a uniform strain can be applied to a material over a large region. In this manner deformation can be better controlled and understood as one of the problems with the traditional deformation techniques is not knowing exactly what the stress state was in a particular location where dislocations are observed. The use of graded buffers also allows the testing of a material at an arbitrary strain level dependent on the lattice constant of the graded buffer. Additionally, the presence of two slip systems at higher strains may allow for a comparative study that may suggest something unknown in the field: the root cause of why dislocations of a particular slip system are active while others are not.

Bibliography

1. Hafez, W. and M. Feng, *Experimental demonstration of pseudomorphic heterojunction bipolar transistors with cutoff frequencies above 600 GHz.* Applied Physics Letters, 2005. **86**(15): p. 152101.
2. Gorham, D., et al., *Electronic Materials and Devices.* 1985: The Open University.
3. Groenert, M.E., *Monolithic Heteroepitaxial Integration of III-V Semiconductor Lasers on Si Substrates*, in *Department of Materials Science and Engineering.* 2002, Massachusetts Institute of Technology: Cambridge.
4. Carlin, J.A., et al., *Impact of GaAs buffer thickness on electronic quality of GaAs grown on graded Ge/GeSi/Si substrates.* Applied Physics Letters, 2000. **76**(14): p. 1884-6.
5. Mistry, K., et al. *Delaying forever: Uniaxial strained silicon transistors in a 90nm CMOS technology.* in *2004 Symposium on VLSI Technology. Digest of Technical Papers, 15-17 June 2004.* 2004. Honolulu, HI, USA: Widerkehr and Associates.
6. Matthews, J.W., S. Mader, and T.B. Light, *Accommodation of misfit across the interface between crystals of semiconducting elements or compounds.* Journal of Applied Physics, 1970. **41**(9): p. 3800-4.
7. Fitzgerald, E.A., *Dislocations in strained-layer epitaxy: theory, experiment, and applications.* Material Science Reports, 1991. **7**(3): p. 87-142.
8. Fitzgerald, E.A., et al., *Structure and recombination in InGaAs/GaAs heterostructures.* Journal of Applied Physics, 1988. **63**(3): p. 693-703.
9. Cockayne, D.J.H. and A. Hons. *Dislocations in semiconductors as studied by weak-beam electron microscopy.* in *International Symposium on Dislocations in Tetrahedrally Coordinated Semiconductors, 25-29 Sept. 1978*
Journal de Physique Colloque. 1979. Hunfeld, West Germany.
10. Olsen, A. and J.C.H. Spence, *Distinguishing dissociated glide and shuffle set dislocations by high resolution electron microscopy.* Philosophical Magazine A (Physics of Condensed Matter, Defects and Mechanical Properties), 1981. **43**(4): p. 945-65.
11. Shockley, W., *Dislocations and Edge States in the Diamond Crystal Structure.* Physical Review, 1953. **91**: p. 228.
12. Hirth, J.P. and J. Lothe, *Theory of Dislocations.* 1982, New York: Wiley.
13. Wood, D.M. and A. Zunger, *Epitaxial effects on coherent phase diagrams of alloys.* Physical Review B (Condensed Matter), 1989. **40**(6): p. 4062-89.
14. Stringfellow, G.B., *Spinodal decomposition and clustering in III/V alloys.* Journal of Electronic Materials, 1982. **11**(5): p. 903-18.
15. de Cremoux, B., *Instability criteria in ternary and quaternary III-V epitaxial solid solutions.* Journal de Physique Colloque
International Colloquium on Epitaxial Growth of Semiconductor Materials, 30 Aug.-1 Sept. 1982, 1982. **43**(C-5): p. 19-27.
16. Cahn, J.W., *On spinodal decomposition.* Acta Metallurgica, 1961. **9**(9): p. 795-801.

17. de Cremoux, B., P. Hirtz, and J. Ricciardi. *On the presence of a solid immiscibility domain in the GaInAsP phase diagram.* in *Gallium Arsenide and Related Compounds, 1980. Eighth International Symposium on Gallium Arsenide and Related Compounds, 22-24 Sept. 1980.* 1981. Vienna, Austria: IOP.
18. Stringfellow, G.B., *Miscibility gaps in quaternary III/V alloys.* Journal of Crystal Growth, 1982. **58**(1): p. 194-202.
19. Stringfellow, G.B., *Calculation of ternary and quaternary III-V phase diagrams.* Journal of Crystal Growth, 1974. **27**(1): p. 21-34.
20. Zunger, A., *First Principles Statistical Mechanics of Semiconductor Alloys and Intermetallic Compounds,* in *NATO Advanced Study Institute on Statics and Dynamics of Alloy Phase Transformations,* P.a.G. Turchi, A., Editor. 1994, Plenum: New York. p. 361-419.
21. Kim, A.Y., W.S. McCullough, and E. Fitzgerald, *Evolution of microstructure and dislocation dynamics in In/sub x/Ga/sub 1-x/P graded buffers grown on GaP by metalorganic vapor phase epitaxy: Engineering device-quality substrate materials.* Journal of Vacuum Science & Technology B (Microelectronics and Nanometer Structures), 1999. **17**(4): p. 1485-501.
22. Maksimov, S.K., *Composition automodulation of semiconductor epitaxial films on the basis of A(3)B(5) solutions.* Microscopy of Semiconductors Conference in Oxford, 1991. **117**: p. 491-496.
23. Hasenohrl, S., et al. *Material properties of graded composition In_xGa_{1-x}P buffer layers grown on GaP by organometallic vapor phase epitaxy.* in *12th International Conference on Metalorganic Vapor Phase Epitaxy, 30 May-4 June 2004*

Journal of Crystal Growth. 2004. Lahina, HI, USA: Elsevier.

24. McGill, L.M., et al., *Microstructural defects in metalorganic vapor phase epitaxy of relaxed, graded InGaP: branch defect origins and engineering.* Journal of Vacuum Science & Technology B (Microelectronics and Nanometer Structures), 2004. **22**(4): p. 1899-911.
25. Langdo, T.A., *Selective SiGe Nanostructures,* in *Department of Materials Science and Engineering.* 2001, Massachusetts Institute of Technology: Cambridge.
26. Wong, W.S., et al. *Integration of GaN thin films with dissimilar substrate materials by Pd-In metal bonding and laser lift-off.* in *Manufacturing Issues in Rapid Thermal Processing, March 1999*

Journal of Electronic Materials. 1999. San Diego, CA, USA: TMS; IEEE.

27. Nakamura, S., et al., *High-power, long-lifetime InGaN/GaN/AlGaN-based laser diodes grown on pure GaN substrates.* Japanese Journal of Applied Physics, Part 2 (Letters), 1998. **37**(3B): p. 309-12.
28. Fitzgerald, E.A., et al., *Elimination of interface defects in mismatched epilayers by a reduction in growth area.* Applied Physics Letters, 1988. **52**(18): p. 1496-8.
29. Luan, H.-C., et al., *High-quality Ge epilayers on Si with low threading-dislocation densities.* Applied Physics Letters, 1999. **75**(19): p. 2909-11.
30. Groenert, M.E., et al., *Monolithic integration of room-temperature cw GaAs/AlGaAs lasers on Si substrates via relaxed graded GeSi buffer layers.* Journal of Applied Physics, 2003. **93**(1): p. 362-7.
31. Groenert, M.E., et al., *Improved room-temperature continuous wave GaAs/AlGaAs and InGaAs/GaAs/AlGaAs lasers fabricated on Si substrates via relaxed graded Ge_xSi_{1-x} buffer layers.* Journal of

Vacuum Science & Technology B (Microelectronics and Nanometer Structures), 2003. **21**(3): p. 1064-9.

32. Watson, G.P., et al., *Relaxed, low threading defect density Si_{0.7}Ge_{0.3} epitaxial layers grown on Si by rapid thermal chemical vapor deposition.* Journal of Applied Physics, 1994. **75**(1): p. 263-9.
33. Gupta, S., et al., *Controlling Threading Dislocation Density in a high mismatched completely relaxed SiGe layer for producing Ultra-Thin Buffers.* Semiconductor Science and Technology, 2006.
34. Lee, M.L., D.A. Antoniadis, and E.A. Fitzgerald, *Challenges in epitaxial growth of SiGe buffers on Si (111),(110), and (112).* Thin Solid Films, 2006. **508**: p. 136-139.
35. Fitzgerald, E.A., *(001) direction may be the direction of crystal growth because dislocations cannot nucleate easily on it. This was in reference to M.L. Lee's work 2006 Thin Solid Films V508 p136.* 2006: Cambridge, MA.
36. Chaudhuri, A.R., J.R. Patel, and L.G. Rubin, *Velocities and densities of dislocations in germanium and other semiconductor crystals.* Journal of Applied Physics, 1962. **33**(9): p. 2736-2746.
37. Houghton, D.C., *Strain relaxation kinetics in Si_{1-x}Ge_x/Si heterostructures.* Journal of Applied Physics, 1991. **70**(4): p. 2136-51.
38. Leitz, C.W., et al., *Dislocation glide and blocking kinetics in compositionally graded SiGe/Si.* Journal of Applied Physics, 2001. **90**(6): p. 2730-6.
39. Samavedam, S.B. and E.A. Fitzgerald, *Novel dislocation structure and surface morphology effects in relaxed Ge/Si-Ge(graded)/Si structures.* Journal of Applied Physics, 1997. **81**(7): p. 3108-16.
40. Currie, M.T., et al., *Controlling threading dislocation densities in Ge on Si using graded SiGe layers and chemical-mechanical polishing.* Applied Physics Letters, 1998. **72**(14): p. 1718-20.
41. Bulsara, M.T., C. Leitz, and E.A. Fitzgerald, *Relaxed In/sub x/Ga/sub 1-x/As graded buffers grown with organometallic vapor phase epitaxy on GaAs.* Applied Physics Letters, 1998. **72**(13): p. 1608-10.
42. Bulsara, M., et al., *Graded In/sub x/Ga/sub 1-x/As/GaAs 1.3 mu m wavelength light emitting diode structures grown with molecular beam epitaxy.* Journal of Applied Physics, 1998. **83**(1): p. 592-9.
43. Freund, L.B., *A criterion for arrest of a threading dislocation in a strained epitaxial layer due to an interface misfit dislocation in its path.* Journal of Applied Physics, 1. **68**(5): p. 2073-80.
44. Matthews, J.W. and J.L. Crawford, *ACCOMMODATION OF MISFIT BETWEEN SINGLE-CRYSTAL FILMS OF NICKEL AND COPPER.* 1970. **5**(3): p. 187-98.
45. Fitzgerald, E.A., et al., *Totally relaxed Ge_xSi_{1-x} layers with low threading dislocation densities grown on Si substrates.* Applied Physics Letters, 1991. **59**(7): p. 811-13.
46. Fitzgerald, E.A., et al. *Relaxed Ge_xSi_{1-x} structures for III-V integration with Si and high mobility two-dimensional electron gases in Si.* in *19th Annual Conference on the Physics and Chemistry of Semiconductor Interfaces, 28-30 Jan. 1992*

Journal of Vacuum Science & Technology B (Microelectronics Processing and Phenomena). 1992. Death Valley, CA, USA.

47. Lee, M.L. and E.A. Fitzgerald, *Strained Si/strained Ge dual-channel heterostructures on relaxed Si_{0.5}Ge_{0.5} for symmetric mobility p-type and n-type metal-oxide-semiconductor field-effect transistors.* Applied Physics Letters, 2003. **83**(20): p. 4202-4.
48. Hirsch, P.B., et al., *Electron microscopy of thin crystals.* 1977, London: Butterworths.
49. Fultz, B. and J. Howe, *Transmission Electron Microscopy and Diffractometry of Materials.* 2002, New York: Springer.
50. Cullity, B.D., *Elements of X-ray Diffraction.* Second ed. 1978, Reading, MA: Addison-Wesley Publishing Company, Inc.
51. van der Sluis, P., *Determination of strain in epitaxial semiconductor layers by high-resolution X-ray diffraction.* Journal of Physics D (Applied Physics), 1993. **26**(4A): p. 188-91.
52. Matney, K.M. and M.S. Goorsky. *A new approach for determining epilayer strain relaxation and composition through high resolution X-ray diffraction.* in *Strained Layer Epitaxy - Materials, Processing, and Device Applications. Symposium, 17-20 April 1995.* 1995. San Francisco, CA, USA: Mater. Res. Soc.
53. McGill, L.M., *MOCVD Growth of InGaP-based Heterostructures for Light Emitting Devices*, in *Department of Materials Science and Engineering.* 2004, Massachusetts Institute of Technology: Cambridge, MA.
54. Mathews, J.W. *Defects associated with the accommodation of misfit between crystals.* in *21st National Symposium of the American Vacuum Society, 8-11 Oct. 1974*

Journal of Vacuum Science and Technology. 1975. Anaheim, CA, USA.

55. Fitzgerald, E.A. and S.B. Samavedam. *Line, point and surface defect morphology of graded, relaxed GeSi alloys on Si substrates.* in *European Materials Research Society 1996 Spring Meeting, Symposium D: Group IV Heterostructures, Physics and Devices (Si, Ge, C, a-Sn), 4-7 June 1996*

Thin Solid Films. 1997. Strasbourg, France: Elsevier.

56. Fitzgerald, E.A., et al. *Influence of strain on semiconductor thin film epitaxy.* in *43rd National Symposium of the American Vacuum Society, 14-18 Oct. 1996*

Journal of Vacuum Science & Technology A (Vacuum, Surfaces, and Films). 1997. Philadelphia, PA, USA: AIP for American Vacuum Soc.

57. Kubo, H. and C.M. Wayman, *Spinodal decomposition of beta brass.* Metallurgical Transactions A (Physical Metallurgy and Materials Science), 1979. **10A**(5): p. 633-43.
58. Kubo, H., I. Cornelis, and C.M. Wayman, *Morphology and characteristics of spinodally decomposed β-brass.* Acta Metallurgica, 1980. **28**(3): p. 405-16.
59. Cui, L.J., et al., *Rapid thermal annealing effects on step-graded InAlAs buffer layer and In_{0.52}Al_{0.48}As/In_{0.53}Ga_{0.47}As metamorphic high electron mobility transistor structures on GaAs substrates.* Journal of Applied Physics, 2002. **91**(4): p. 2429-32.
60. Fastenau, J.M., et al. *Strain relaxation and dislocation filtering in metamorphic HBT and HEMT structures grown on GaAs substrates by MBE.* in *2004*

International Conference on Indium Phosphide and Related Materials. 16th IPRM, 31 May-4 June 2004. 2004. Kagoshima, Japan: IEEE.

61. Becourt, N., et al., *Surface step bunching and crystal defects in InAlAs films grown by molecular beam epitaxy on (111)B InP substrates.* Applied Physics Letters, 1997. **71**(20): p. 2961-3.
62. Rosenberg, J.J., et al., *In//0//. //1//5Ga//0//. //8//5As/GaAs PSEUDOMORPHIC SINGLE QUANTUM WELL HEMT.* IEEE Electron Device Letters, 1985. **ED-6**(10): p. 491-493.
63. Wang, C.A., *Correlation between surface step structure and phase separation in epitaxial GaInAsSb.* Applied Physics Letters, 2000. **76**(15): p. 2077-9.
64. Wang, C.A., et al., *High-quantum-efficiency 0.5 eV GaInAsSb/GaSb thermophotovoltaic devices.* Applied Physics Letters, 1999. **75**(9): p. 1305-7.
65. Cheng, K.Y., et al. *Formation of lateral quantum-wells in vertical short-period superlattices.* in *Proceedings of the 18th International Symposium on Gallium Arsenide and Related Compounds, Sep 9-12 1991.* 1992. Seattle, WA, USA: Institute of Physics Publishing Ltd.
66. Henoc, P., et al., *Composition modulation in liquid phase epitaxial In/sub x/Ga/sub 1-x/As/sub y/P/sub 1-y/ layers lattice matched to InP substrates.* Applied Physics Letters, 1982. **40**(11): p. 963-5.
67. Glas, F., et al., *Interface spinodal decomposition in LPE In/sub x/Ga/sub 1-x/As/sub y/P/sub 1-y/ lattice matched to InP.* Journal de Physique Colloque International Colloquium on Epitaxial Growth of Semiconductor Materials, 30 Aug.-1 Sept. 1982, 1982. **43**(C-5): p. 11-16.
68. Glas, F., et al., *STEM Microanalysis in InGaAsP Alloys Grown by Liquid Phase Epitaxy.* 10th International Congress on Electron Microscopy, 1982. **2**: p. 405.
69. McDevitt, T.L., S. Mahajan, and D.E. Laughlin, *Two-dimensional phase separation in In/sub 1-x/Ga/sub x/As/sub y/P/sub 1-y/ epitaxial layers.* Physical Review B (Condensed Matter), 1992. **45**(12): p. 6614-22.
70. Cahn, J.W., *On spinodal decomposition in cubic crystals.* Acta Metallurgica L2 - http://dx.doi.org/10.1016/0001-6160(62)90114-1, 1962. **10**(3): p. 179-183.
71. Fitzgerald, E.A., et al., *Relaxed Ge_xSi_{1-x} structures for III-V integration with Si and high mobility two-dimensional electron gases in Si.* Journal of Vacuum Science & Technology B: Microelectronics Processing and Phenomena, 1992. **10**(4): p. 1807.
72. Frank, F.C., *`Edge' dislocations as crystal growth sources.* Journal of Crystal Growth, 1981. **51**(2): p. 367-8.
73. Zhou, X.C., et al. *Strain-field induced crosshatch formation during molecular beam epitaxy of InGaAs/GaAs films.* in *Materials Research Society Spring Meeting, Apr 13-15 1993.* 1993. San Francisco, CA, USA: Publ by Materials Research Society, Pittsburgh, PA, USA.
74. Louthan, J., M.R., *Stress orientation of Titanium Hydride in Titanium.* Metallurgical Society of American Institute of Mining, Metallurgical and Petroleum Engineers -- Transactions, 1963. **227**(5): p. 1166-1170.
75. Eto, T., A. Sato, and T. Mori, *Stress-oriented precipitation of G.P. zones and &thetas;' in an Al-Cu alloy.* Acta Metallurgica, 1978. **26**(3): p. 499-508.
76. Ferguson, P. and K.H. Jack, *Stress orientation of nitrogen during the quench-aging of nitrogen ferrite.* Philosophical Magazine A (Physics of Condensed Matter, Defects and Mechanical Properties), 1985. **52**(4): p. 509-23.

77. Bogers, A.J., *Orientation relation between austenite and martensite in an fe-ni alloy transformed by isothermal compression.* Acta Metallurgica L2 - http://dx.doi.org/10.1016/0001-6160(62)90128-1, 1962. **10**(3): p. 260-262.
78. Mahajan, S., et al., *Spinodal decomposition in InGaAsP epitaxial layers [photoluminescence].* Journal of Crystal Growth, 1984. **68**(2): p. 589-95.
79. Ipatova, I.P., V.G. Malyshkin, and V.A. Shchukin, *On spinodal decomposition in elastically anisotropic epitaxial films of III-V semiconductor alloys.* Journal of Applied Physics, 1993. **74**(12): p. 7198-210.
80. Palfrey, H.D., M. Brown, and A.F.W. Willoughby, *Self-diffusion of gallium in gallium arsenide.* Journal of the Electrochemical Society, 1981. **128**(10): p. 2224-8.
81. Palfrey, H.D., M. Brown, and A.F.W. Willoughby, *Self-diffusion in gallium arsenide.* Journal of Electronic Materials, 1983. **12**(5): p. 863-77.
82. Petroff, P.M., et al., *Alloy clustering in Ga/sub 1-x/Al/sub x/As compound semiconductors grown by molecular beam epitaxy.* Physical Review Letters, 1982. **48**(3): p. 170-3.
83. Bernard, J.E., S. Froyen, and A. Zunger, *Spontaneous surface-induced long-range order in Ga_{0.5}In_{0.5}P alloys.* Physical Review B (Condensed Matter), 1991. **44**(20): p. 11178-95.
84. Peiro, F., et al., *Influence of the composition modulation on the relaxation of In/sub 0.54/Ga/sub 0.46/As strained layers.* Applied Physics Letters, 1991. **59**(16): p. 1957-9.
85. Treacy, M.M.J., J.M. Gibson, and A. Howie, *ON ELASTIC RELAXATION AND LONG WAVELENGTH MICROSTRUCTURES IN SPINODALLY DECOMPOSED In//xGa//1// minus //xAs//yP//1// minus //y EPITAXIAL LAYERS.* Philosophical Magazine A: Physics of Condensed Matter, Defects and Mechanical Properties, 1985. **51**(3): p. 389-417.
86. Eremenko, V., et al., *AFM and TEM study of the lateral composition modulation in etched and photo etched In/sub x/Ga/sub 1-x/P epitaxial layers.* Materials Science & Engineering B (Solid-State Materials for Advanced Technology), 2002. **B91-92**: p. 269-73.
87. Takano, Y., et al., *Temperature dependence of threading dislocation density in In_{0.2}Ga_{0.8}As layers grown on GaAs substrates by metalorganic-vapor phase epitaxy.* Journal of Crystal Growth, 2005. **282**(1-2): p. 36-44.
88. Takano, Y., et al., *Threading dislocations and phase separation in InGaAs layers on GaAs substrates grown by low-temperature metalorganic vapor phase epitaxy.* Japanese Journal of Applied Physics, Part 1 (Regular Papers, Short Notes & Review Papers), 2005. **44**(9A): p. 6403-11.
89. McGill, L.M., *MOCVD Growth of InGaP-based Heterostructures for Light Emitting Devices*, in *Materials Science and Engineering.* 2004, Massachusetts Institute of Technology: Cambridge, Massachusetts.
90. Kim, A.Y., *Co-Evolution of Microstructure and Dislocation Dynamics in InGaP/GaP: Engineering High Qualit Epitaxial Transparent Substrates.*, in *Materials Science and Engineering.* 2000, Massachusetts Institute of Technology: Cambridge, Massachusetts.

91. Bulsara, M.T., *Materials Issues with the Integration of Lattice-Mismatched* In_xGa_{1-x}*as Devices on GaAs*, in *Materials Science and Engineering.* 1998, Massachusetts Institute of Technology: Cambridge, Massachusetts.
92. Cahn, J.W., *Hardening by spinodal decomposition.* Acta Metallurgica L2 - http://dx.doi.org/10.1016/0001-6160(63)90022-1, 1963. **11**(12): p. 1275-1282.
93. Dahlgren, S.D., *Correlation of yield strength with internal coherency strains for age-hardened Cu-Ni-Fe alloys.* Metallurgical Transactions A (Physical Metallurgy and Materials Science), 1977. **8A**(2): p. 347-51.
94. Wegscheider, W. and H. Cerva, *Effect of compressive and tensile strain on misfit dislocation injection in SiGe epitaxial layers.* Journal of Vacuum Science & Technology B (Microelectronics Processing and Phenomena)

Topical Conference on Silicon-Based Heterostructures II, 9-10 Nov. 1992, 1993. **11**(3): p. 1056-63.

95. Huston, E.L., J.W. Cahn, and J.E. Hilliard, *Spinodal decomposition during continuous cooling.* Acta Metallurgica L2 - http://dx.doi.org/10.1016/0001-6160(66)90193-3, 1966. **14**(9): p. 1053-1062.
96. Turnbull, D. and H.N. Treaftis, *Micrographic investigation of precipitation in Pb-Sn alloys.* Metallurgical Society of American Institute of Mining, Metallurgical and Petroleum Engineers -- Transactions, 1958. **212**(1): p. 33-39.
97. Cahn, J.W., *Kinetics of cellular segregation reactions.* Acta Metallurgica L2 - http://dx.doi.org/10.1016/0001-6160(59)90164-6, 1959. **7**(1): p. 18-28.
98. Chu, S.N.G., et al., *Surface layer spinodal decomposition in In/sub 1-x/Ga/sub x/As/sub y/P/sub 1-y/ and In/sub 1-x/Ga/sub x/As grown by hydride transport vapor-phase epitaxy.* Journal of Applied Physics, 1985. **57**(10): p. 4610-15.
99. Gonzalez, L., et al., *Relaxation behavior of undoped In_xGa_{1-x}P 0.5<x<0.7 grown on GaAs by atomic layer molecular-beam epitaxy.* Journal of Applied Physics, 15. **80**(6): p. 3327-32.
100. Leitz, C.W., et al., *Dislocation glide and blocking kinetics in compositionally graded SiGe/Si.* Journal of Applied Physics, 15. **90**(6): p. 2730-6.
101. Liu, T.Y., et al. *Electronic properties of dislocations in heavily dislocated quantum well structures: doping effects.* in *III-V Heterostructures for Electronic/Photonic Devices Symposium, 24-27 April 1989.* 1989. San Diego, CA, USA: Mater. Res. Soc.
102. Tangring, I., et al., *Strong 1.3-1.6 μm light emission from metamorphic InGaAs quantum wells on GaAs.* Applied Physics Letters, 2005. **86**(17): p. 171902-1.
103. Karnthaler, H.P., *STUDY OF GLIDE ON left brace 001 right brace PLANES IN F. C. C. METALS DEFORMED AT ROOM TEMPERATURE.* Philosophical Magazine A: Physics of Condensed Matter, Defects and Mechanical Properties, 1978. **38**(2): p. 141-156.
104. Carrard, M. and J.L. Martin, *STUDY OF (001) GLIDE IN left bracket 112 right bracket ALUMINIUM SINGLE CRYSTALS. I. CREEP CHARACTERISTICS.* Philosophical Magazine A: Physics of Condensed Matter, Defects and Mechanical Properties, 1987. **56**(3): p. 391-405.
105. Stevens, A.L. and L.E. Pope, *Observation of secondary slip in impact-loaded aluminum single crystals. I.* Scripta Metallurgica, 1971. **5**(11): p. 981-6.

106. Le Hazif, R. and J.-P. Poirer, *Cross-slip on {110} planes in aluminium single crystals compressed along <100> axis.* Acta Metallurgica, 1975. **23**(7): p. 865-71.

107. Pichaud, B. and F. Minari, *110 DIRECTION left brace 110 right brace IN COPPER SLIGHTLY DEFORMED AT ROOM TEMPERATURE.* 1980. **14**(11): p. 1171-1174.

108. Albrecht, M., et al. *Structure of dislocations formed in Ge(Si) by glide on secondary glide planes.* in *Proceedings of Microscopy of Semiconducting Materials: 8th Oxford Conference (SMM VIII), 5-8 April 1993.* 1993. Oxford, UK: IOP.

109. Albrecht, M., et al., *Dislocation glide in {110} planes in semiconductors with diamond or zinc-blende structure.* Applied Physics Letters, 1993. **62**(18): p. 2206-8.

110. Okada, T., et al., *Dislocation relaxation in InAs/sub y/P/sub 1-y/ films deposited onto (001) InP by gas-source molecular beam epitaxy.* Applied Physics Letters, 1993. **63**(23): p. 3194-6.

111. Liu, X.W., et al., *Edge-type misfit dislocations produced by thermal processing of pre-relaxed In_xGa_{1-x}As/GaAs heterostructures.* Journal of Applied Physics, 2000. **88**(10): p. 5975-5980.

112. Kim, J., *TEM characterization of InAs epilayers grown on InP substrates by metalorganic chemical-vapor deposition.* Journal of the Korean Physical Society
International Conference on Advanced Materials and Devices '96, 11-13 June 1996, 1997. **31**(1): p. 215-18.

113. Kim, J., et al., *Misfit dislocation generated in InAs epilayer and InP substrate interfaces grown by metalorganic chemical-vapor deposition.* Materials Letters, 2002. **53**(6): p. 446-51.

114. Bonar, J.M., et al., *Layered structures : heteroepitaxy, superlattices, strain, and metastability : symposium held November 27-December 1, 1989, Boston, Massachusetts, U.S.A,* ed. B.W. Dodson. 1990, Pittsburgh, Pa.: Materials Research Society. xvii, 823.

115. Bonar, J.M., et al., *Observations of new misfit dislocation configurations and slip systems at ultrahigh stresses in the (Al)GaAs/In_xGa_{1-x}As/GaAs(100) system.* Applied Physics Letters, 1992. **60**(11): p. 1327.

116. Zou, J., et al., *Misfit dislocations lying along <100> in [001] GaAs/In/sub 0.25/Ga/sub 0.75/As/GaAs quantum well heterostructures.* Applied Physics Letters, 26. **65**(13): p. 1647-9.

117. Young, E.C., et al., *Strain relaxation by <100> misfit dislocations in dilute nitride* $In_xGa_{1-x}As_{1-y}N_y$*/GaAs quantum wells.* Physica Status Solidi (a), 2005. **202**(15): p. 2849-2857.

118. Dynna, M. and G.C. Weatherly, *The energetics of the relief of misfit strain in InAs/sub y/P/sub 1-y/ films grown on <100> InP substrates by means of three sets of dislocations.* Scripta Metallurgica et Materialia, 1995. **32**(10): p. 1565-71.

119. Dynna, M., T. Okada, and G.C. Weatherly, *The nature of dislocation sources and strain relief in InAs/sub y/P/sub 1-y/ films grown in <100> InP substrates.* Acta Metallurgica et Materialia, 1994. **42**(5): p. 1661-72.

120. Zhang, X., et al., *The strain relaxation of In_{0.1}Ga_{0.9}As on GaAs(110) grown by molecular beam epitaxy.* Journal of Applied Physics, 1995. **78**(11): p. 6454-7.

121. Zhang, X. and D.V. Pashley, *A comparison of strain relief behaviour of In_xGa_{1-x}As alloy on GaAs (001) and (110) substrates.* Journal of Materials Science: Materials in Electronics, 1996. **7**(5): p. 361-367.
122. Quitoriano, N. and E.A. Fitzgerald, Journal of Vacuum Science & Technology B, 2006. **In Press**.
123. Nabarro, F.R.N., *Theory of Crystal Dislocations.* 1967, London: Oxford University Press. 821.
124. Cullis, A.G., A.J. Pidduck, and M.T. Emeny, *Misfit dislocation sources at surface ripple troughs in continuous heteroepitaxial layers.* Physical Review Letters, 18. **75**(12): p. 2368-71.
125. Maeda, K. and S. Takeuchi, *Recombination enhanced dislocation glide in InP single crystals.* Applied Physics Letters, 1983. **42**(8): p. 664-6.
126. Dunstan, D.J., et al., *Plastic relaxation of InGaAs grown on GaAs.* Applied Physics Letters, 1991. **59**(26): p. 3390-2.
127. Krishnamoorthy, V., et al., *Residual strain analysis of In_xGa_{1-x}As/GaAs heteroepitaxial layers.* Applied Physics Letters, 1992. **61**(22): p. 2680.
128. Kightley, P., et al. *Dislocation dipoles in strained InGaAs layers grown on GaAs.* in *Microscopy of Semiconducting Materials, 1991, Mar 25-28 1991.* 1991. Oxford, Engl: Publ by IOP Publishing Ltd, Bristol, Engl.
129. Bonar, J.M., et al., *Structural and Electronic Properties of GaAs/InGaAs/GaAs Heterostructures.* Mat. Res. Soc. Symp. Proc., 1990. **160**: p. 117-122.
130. *Forward.* Journal Physique, 1979. **40**.
131. Fitzgerald, E.A., *Dislocations in strained-layer epitaxy. Theory, experiment, and applications.* 1991, Publ by Elsevier Science Publ Co Inc, New York, NY, USA. p. 87-142.
132. Ting, S.M. and E.A. Fitzgerald, *Metal-organic chemical vapor deposition of single domain GaAs on Ge/Ge_xSi_{1-x}/Si and Ge substrates.* Journal of Applied Physics, 2000. **87**(5): p. 2618-2628.
133. Pitera, A.J., *Engineered Substrated for Coplanar Integration of Lattice-Mismatched Semiconductors with Silicon,* in *Department of Materials Science and Engineering.* 2005, Massachusetts Institute of Technology: Cambridge, MA.
134. Isaacson, D.M., in *Department of Materials Science and Engineering.* 2006, Massachusetts Institute of Technology: Cambrdige, MA.